# APPLICATION OF SATELLITE-BASED RAINFALL ESTIMATES AND INUNDATION EXTENT FOR FLOOD MODELING IN THE SEBEYA CATCHMENT, RWANDA

EMMANUEL NTAWUKURIRYAYO
August 2022

SUPERVISORS:
DR. ING. T.H.M. RIENTJES
IR. G.N. PARODI

# APPLICATION OF SATELLITE-BASED RAINFALL ESTIMATES AND INUNDATION EXTENT FOR FLOOD MODELING IN THE SEBEYA CATCHMENT, RWANDA

EMMANUEL NTAWUKURIRYAYO
Enschede, The Netherlands, August 2022

Thesis submitted to the Faculty of Geo-Information Science and Earth Observation of the University of Twente in partial fulfilment of the requirements for the degree of Master of Science in Geo-information Science and Earth Observation.
Specialization: Water Resources and Environmental Management

SUPERVISORS:
DR. ING. T.H.M. RIENTJES
IR. G.N. PARODI

THESIS ASSESSMENT BOARD:
Dr. S. Salama (Chair)
Prof. dr.ir. P (Paolo) Reggiani (External Examiner, University of Siegen, Germany)

# ABSTRACT

The Sebeya catchment in its downstream part of Mahoko market and tea plantations has suffered from frequent floods in the past years. The flooding is caused by heavy rainfall in the upstream hills and forests of the Sebeya floodplain and the river's bank instability. However, the hydrological and hydrodynamic knowledge of flood dynamics is limited. Data required to build and calibrate the hydrological and flood models constitutes a main challenge in the Sebeya catchment. Therefore, this study aims to assess the application of satellite rainfall estimates (SREs) in the hydrological model and satellite-derived inundation extent in the hydrodynamic flood calibration in the Sebeya catchment. Two satellite rainfall products, CHIRPS and TAMSAT, were analyzed and bias-corrected for their systematic errors using the available rain gauge as a reference from 2014 to 2018. Based on an analysis that relies on four statistical indicators, correlation, relative bias, root mean square (RMSE) and mean errors (ME), the CHIRPS product outperformed the TAMSAT SRE. The time-space variable bias correction was used to test the sequential (SW) and moving (MW) window schemes on 3, 5, 6, 7, 10, 12, 15, 17, and 20 sample window sizes to correct identified errors in SREs. An algorithm was developed to overcome the high difference errors found in uncorrected SREs and rain gauges. The RMSE, correlation, and standard deviation were used to examine the bias correction outputs. This study revealed that 6 days SW bias correction scheme performed well for the CHIRPS product and 6 days MW sampling window for the TAMSAT product. The rain gauges and bias-corrected satellite rainfall data served as model input to force the HBV rainfall-runoff model of the Sebeya catchment. Model calibration was performed using corrected and modified observed streamflow. The NS and RVE served as indicators to evaluate the performance of the HBV model. After calibrating the model with rain gauge rainfall data, NS of 0.8 and RVE of 5.9 % were found. The bias-corrected CHIRPS product also performed satisfactorily with the NS of 0.8 and RVE of 2.5 %. On the contrary, the bias-corrected TAMSAT rainfall data could not reproduce the observed hydrograph because of identified weak rainfall detection of the product, which propagated in its further use. The rain gauges and CHIRPS bias-correction were combined to simulate streamflow, which serves as upstream inflow to the 2D hydrodynamic flood model. The Planetscope satellite image was used for the hydrodynamic model calibration. NDVI differencing changed detection was used to delineate flood extent from the Planetscope. The available DTM depicts defects to represent surface features, like river reach. Therefore, the DTM was enhanced to produce an adequate topographic representation for the hydrodynamic model. It is deduced that the simulated flood extent improves after DTM enhancement for the Sebeya floodplain. The 2D HEC-RAS was found sensitive to upstream inflow boundaries, where streamflow generated by rain gauges and bias-corrected and uncorrected CHIRPS rainfall were tested. The simulated flood extent appears acceptable based on on-site knowledge by the author of this document. The simulation reveals the conveyance of water in the river reaches. The critical success index (CSI) indicator was poor when comparing the satellite-derived and hydrodynamic simulated flood extent. Overall, the findings indicate that the satellite-derived inundation extent could not be used in calibrating the hydrodynamic model of the Sebeya catchment floodplains.

**Keywords:** Sebeya catchment, Satellite rainfall estimates, Bias correction, optimal sampling window, HBV hydrological model, DEM enhancement, satellite inundation extent, 2D HEC-RAS hydrodynamic model

# ACKNOWLEDGEMENTS

# TABLE OF CONTENTS

# LIST OF FIGURES

# LIST OF TABLES

# 1. INTRODUCTION

## 1.1. Background

Floods are natural disasters affecting many people and with socio-economic impacts worldwide. Flooding may cause loss of people's lives, displacement, destruction of infrastructures, and environmental degradation (IFRC, 2012). In 2016, floods affected 78.1 million people and cost almost US $59 billion for 31 countries among 79 that suffered from such hazards (Beden and Ulke Keskin, 2021). Climate change may affect rainfall patterns and intensity, leading to flooding (Dubey et al., 2021). Projections reveal an increase in heavy precipitation in several regions due to a temperature increase of 1.5°C above pre-industrial conditions (Masson-Delmotte et al., 2018). Tropical cyclones and monsoon rains are the leading cause of flooding in emerging and least developed countries (Douben, 2006). Africa is the most vulnerable continent to flooding due to its limited adaptive capacity (Niang et al., 2015). It is expected that the African climate will change with an increase of 2°C in temperature above the 20th century (Weitzman, 2007), which is likely to cause extreme weather events, droughts, and floods (Collier et al., 2008). Moreover, population increase, topographic factors, and informal urbanization continue to increase flood risks.

Flooding caused significant losses in Rwanda, particularly in the Sebeya watershed, located in the north-western part of the country, due to heavy rainfall, illegal mining, agriculture, and the Sebeya river basin urban population increase (MINEMA, 2018). Flood events from the past years trigger deaths, injuries, displacement of people, economic losses, etc., across the country. However, there has been little research on floods in the Sebeya catchment. For instance, Marie Aimée (2020) highlighted flood resilience practices such as artificial lake creation, deviation of the Sebeya river, and retaining walls along the river to protect flood-prone areas. The study applies a participatory GIS[1] approach to monitor floods and interventions in the Sebeya catchment. In recent years, through REMA[2] and RWB[3], the Government of Rwanda carried out a detailed design of flood control measures and the development of flood early warning systems for the Sebeya catchment. The significant outcomes of these reports were flood hotspots, mainly the Mahoko Centre, different agricultural lands, and Petit Séminaire high school areas, due to heavy rainfall and steep-slope mountains in the upstream part of the Sebeya catchment.

The Mahoko Centre and tea plantations are the areas of interest in this research. They are located in the downstream flat floodplain area of the Sebeya catchment, surrounded by upstream hills. Typically, the Mahoko area is a dynamic town with regular traffic and trade, leading to the town's growth, thus increasing flood risk and vulnerability. The tea plantation areas are located upstream at almost 1.5 kilometers from the Mahoko Centre on the left bank of the Sebeya river. Despite their benefits, these areas are more vulnerable to frequent flooding. Sebeya riverbanks instability and heavy rain in the Gishwati forest and other upstream hills are the leading causes of the resulting inundations. However, the lack of availability and knowledge on the physical characteristics of flood events, the area's potential impacts, and the site's insufficient flood research are the main factors in selecting the Sebeya catchment as the study area.

Rainfall data are crucial input when estimating floods using the hydrological models (Hamlin, 1983). However, limited and unevenly distributed rain gauges, like rain gauges in the Sebeya catchment, could lead to inevitable errors during streamflow simulation that causes flooding using hydrological models. Consequently, satellite rainfall estimates (SREs) have been alternatively used as a substitute for rain gauges

---

[1] Geographic Information System
[2] Rwanda Environment Management Authority
[3] Rwanda Water Resources Board

to spatially represent the rainfall in hydrological models (Nikolopoulos et al., 2010; Wu et al., 2012; Zhao et al., 2015). SREs provide rainfall information at good Spatio-temporal resolution and coverage in data-limited areas (Belay et al., 2019; Jamandre and Narisma, 2013). Different authors, Adjei et al. (2015); Bitew and Gebremichael (2011); Tramblay et al. (2016); Wiwoho et al. (2021), have indicated the application of SREs in hydrological modeling. Nevertheless, SREs possess uncertainties, which could be caused by instruments and algorithms used to detect rainfall of satellites (Gebregiorgis and Hossain, 2013). Habib et al. (2014) revealed that it is essential to correct and minimize the systematic errors in SREs products before they can be used in hydrological modeling.

Flood modeling and flood forecasting use hydrodynamic models to estimate flood characteristics (flood extent, depth, duration, and velocity) (Ongdas et al., 2020). However, hydrodynamic models require calibration for their applicability using field observations or remote sensing detections to increase knowledge of adequate flood management (Alivio et al., 2019). Lack of field observations on the flood extent in the data-scarce Sebeya catchment presents difficulties in hydrodynamic model calibration. Thus, Satellite remote sensing flood detection is an adapted method for calibrating flood modeling with considerable spatial resolution and cost-effective demand for flood delineations (Addae, 2018). Flood inundation coverage is extracted using optical satellites or radar sensors to evaluate flood modeling in the past decades (Klemas, 2015). Numerous satellites, such as Sentinels, Landsat, etc., provide freely available data for flood mapping applications. However, clouds in the atmosphere challenge optical remote sensing to monitor inundation areas during a flood event (Shen et al., 2019). The radar remote sensing method uses synthetic-aperture radar sensors in flood monitoring to differentiate flooded areas from non-flood areas (Addae, 2018). Radar can identify and map the inundation areas under all weather conditions and periods (day and night) using backscattering change and supervised classification (Manavalan, 2017). However, the effects of wind and backscattering magnitudes of different land cover types often hinder the possibility of the use of SAR in defining inundation areas (Refice et al., 2014).

Remote sensing flood detection presents challenges, but they provide significant support for flood research in data deficient environments (Yan et al., 2015). Karim et al. (2011) used remote sensing derived flood extent by calibrating the hydrodynamic model of Fitzroy River catchment (Australia). The calibration method by Di Baldassarre et al. (2009) reveals that a hydrodynamic model's optimal set of parameters depends on the observation of flood extent, the technique to extract flood extent, and the type of satellite applied to assess the model. Furthermore, Grimaldi, Li, Pauwels, and Walker (2016) describe the importance of remote sensing flood extent in the hydrodynamic model calibration and validation in data-scarce areas.

## 1.2.    Problem statement

Knowledge and estimates of flood extent are essential in flood hazard monitoring and management, risk reduction, and other water resources practices in frequently flooded areas. The Sebeya catchment is one of the areas in Rwanda with frequent floods. Limited information on the inundation extent for hydrodynamic model analysis in the Sebeya catchment is the prime motive for this research. Poor and uncertain data availability constitutes a second motive. Hydrodynamic models are essential tools that serve in the reduction of flood impacts, the suggestion of protective practices, and operational flood management in flood risk hotspots (Singh et al., 2020). Poor data availability is one barrier to setting up, calibrating, and validating the hydrodynamic model outputs of flood-prone areas (Ghimire, 2013). This challenge is also found in the Sebeya catchment. However, the lack of observed flood extent has made flood extent assessments through remote sensing an alternative data source in data-limited areas like the Sebeya catchment.

Several researchers have explored the applicability of satellite-based inundation extent maps as cost-effective and valuable data in calibrating hydrodynamic flood modeling (Anusha and Bharathi, 2020; Notti et al., 2018). However, satellite images present drawbacks like the limited temporal and spatial resolution of sensors, land surface cover effects, and weather conditions interference, reducing the accuracy of flood observed extent for model calibration (Addae, 2018). Regardless of those challenges, Giustarini et al. (2015) reveal that a combination of remote sensing and hydrodynamic flood extents provides necessary information on flood inundation maps. Therefore, investigating the capability of remote sensing inundation extents is a key in the hydrodynamic model for data-limited areas like the Sebeya catchment.

The Sebeya catchment lacks detailed information on the flood events, which frequently occur in the area (once or twice annually) during the rainy season (Figure 1-1). The frequent flood necessitates the development of hydrodynamic modeling for flood mapping simulations, predictions, and forecasting. Furthermore, limited field observed inundation data to calibrate the hydrodynamic model makes satellite observations necessary as an alternative for effective flood modeling. However, applying satellite-derived inundation extent maps to calibrate hydrodynamic models is not common in Rwanda. Hence, this study aims to develop the 2D[4] hydrodynamic model and calibrate it using satellite-derived flood extents in the Sebeya catchment's model domain.



Figure 1-1 Examples of flood events at Mahoko Centre (Photo credits: the Newtimes and umuseke newspapers)

### 1.3. Research objectives and questions

The main objective of this research is to investigate the applicability of satellite-based rainfall estimates (SREs) and satellite-derived inundation extent to perform hydrodynamic flood modeling of the floodplain in Sebeya catchment, Rwanda.

#### 1.3.1. Specific objectives

In the context of the main objective mentioned above, the following specific objectives of the research are outlined.

- To extract the extent of inundation from optical satellite images in the semi-urban floodplain.

---

[4] Two dimensional

- To quantify the errors in satellite rainfall estimates (SREs) with reference to ground-based rainfall recordings.
- To conduct bias-correction procedures on SREs for the Sebeya catchment.
- To develop a rainfall-runoff model for streamflow estimation of the Sebeya catchment using satellite rainfall products.
- To build a 2D hydrodynamic model for flood inundation simulation in a frequently flooded area.
- To assess the relation of the inundation derived from satellite image with the hydrodynamic model flood extent.

## 1.4.    Research questions

The following research questions will be addressed following the objectives mentioned above of this study:

- What techniques can be applied to extract inundation extent from optical satellites in the semi-urban flooded area?
- What is the magnitude of errors found in the SREs with reference to InSitu rainfall?
- What could be the appropriate scheme to bias-correct SREs in the Sebeya catchment?
- How can satellite-based rainfall patterns be used to simulate the daily streamflow of the Sebeya catchment?
- How do DEM uncertainties propagate in the hydrodynamic flood model results?
- What is the impact of the inflow boundary conditions on the hydrodynamic model?
- What approaches can be applied to evaluate the relationship between the model-simulated flood extent and satellite-derived inundation maps?

## 1.5.    Thesis structure

This research thesis comprises six chapters. The first chapter introduces the study with an overview of the background, research problem, objectives, and research questions. The second chapter illustrates the literature review on the applied methods and studies related to this research thesis. The third chapter describes the study area, available datasets, and their pre-processing. The fourth chapter outlines the details of methods used to answer research questions. The fifth chapter addresses the results of the research and their discussions. The last chapter, the sixth, summarizes the primary research's outcomes and provides recommendations for future research studies and the limitations of this study.

# 2.  LITERATURE REVIEW

## 2.1.  Optical remote sensing applications for flood mapping

Optical remote sensing-based techniques provide essential information in inundation detection and mapping for flood management (Chignell et al., 2015). Flood extent is extracted from optical satellite images by applying different techniques, including supervised or unsupervised classification and spectral indices thresholding to separate water and non-water pixels (Sekertekin, 2019). Spectral indices thresholding is a commonly applied method to extract water from satellite images because it is an easy-to-use, simple, straightforward, and less time-consuming approach to retrieving flood extent (Schumann et al., 2009). NDWI and MNDWI are two commonly used water indices for flood extent mapping. McFeeters (1996) proposed an NDWI index that uses the optical image's Green, NIR, and MIR bands to differentiate water extent areas from other land use classes. However, NDWI presents difficulties in separating water and built-up pixels in an urban flooded area (Feyisa et al., 2014). Therefore, Xu (2006) proposed a modified version of NDWI, MNDWI, that replaces the NIR band in NDWI with a SWIR band to accurately extract inundation extent from optical satellites. The choice of water index to delineate surface water extent depends on the bands of satellite images. Planetscope sensors use atmospherically corrected bottom-of-atmosphere (BOA) reflectance values for its four bands (visible and NIR bands) (Planet Labs, 2020). For other optical sensors like Sentinel-2, top-of-atmosphere (TOA) reflectances are used for level-1B and level-1C, while level-2A products consist of BOA reflectance images with visible NIR and MIR bands (SUHET, 2015). The available products of optical images provide pixel values of BOA or TOA reflectances scaled by 10000 (for example, a pixel value of 1200 = 0.12 TOA or BOA reflectance value). Both indices' values range from -1 to +1, where positive values ranging from 0 to 1 indicate water pixels while negative values (0 to -1) indicate non-water surface cover. Authors like ABAZAJ (2019) and Acharya et al. (2016) used the NDWI index for flood mapping in the Buna River area, Albania and Han River basin, North Korea, respectively. On the other hand, Sajjad et al. (2021) and Sivanpillai et al. (2021) applied MNDWI to delineate flood extent. Table 2-1 describes the equation of each water index.

<div align="center">Table 2-1 Water indices</div>

$$NDWI = \frac{Green - NIR}{Green + NIR} \qquad MNDWI = \frac{Green - MIR}{Green + MIR}$$

NDWI and MNDWI indices use the thresholding method to separate water and non-water features. The selection of threshold values makes extracting water coverage in optical images challenging. Therefore, an appropriate threshold value should be selected based on the visual inspection, image histogram analysis, and pixel-by-pixel investigation to avoid misclassifying non-water features to water extent. A threshold value varies according to the image characteristics (Yang et al., 2017). Addae (2018) and Ali et al. (2019) applied the thresholding method to differentiate water from non-water features. The approach that will be used in this study is detailed in section 4.2.

Although optical satellite images provide information on the flood extent, they present various limitations. Spatial resolution, dark objects or shadows of buildings and vegetation, highly turbid water and cloud cover, and shadows introduce difficulties in inundation and surface water extent mapping (Yang et al., 2017).

## 2.2. Height Above Nearest Drainage (HAND) method

The Height Above Nearest Drainage (HAND) approach proposed by Rennó et al. (2008) can be used to differentiate water lookalike features in satellite-derived flood extent. The HAND algorithm uses the digital elevation model (DEM) as input. First, it is corrected to remove sinks, then flow directions can be computed, and the drainage network definition follows (Rennó et al., 2008). The HAND model modifies the topographic terrain with respect to the elevation of the drainage network. The sinks in the DEM are filled to avoid effects on the topographical representation created. Then, the fixed DEM generates the local drain direction (LDD) using the flow direction method. The upstream flow accumulated cells contributing to a downstream grid are defined using LDD. A minimum threshold of accumulated grids is used to delineate the drainage network. The nearest drainage map is generated using the LDD and drainage network with coded flow path grid points. Therefore, subtracting the nearest drainage map from the DEM results in the HAND grid map (Bhatt and Srinivasa Rao, 2018). In the HAND map, zero elevation values indicate the drainage network (Figure 2-1). From Figure 2-1, the DEM elevation grid of 72 is connected to the drainage cell of 53, and their subtraction results in a HAND grid of 19, which means the grid point is 19m above its nearest drainage cell. Figure 2-1 describes the summarized steps in the HAND creation process adopted by Rennó et al. (2008). The HAND method output is categorized into different classes based on either knowledge of the study area or field data (Nobre et al., 2011). The HAND approach can determine susceptible flood-prone and non-flooded areas (Hu and Demir, 2021). Authors like Nobre et al. (2016) and Bhatt and Srinivasa Rao (2018) applied the HAND approach to map inundation extent.
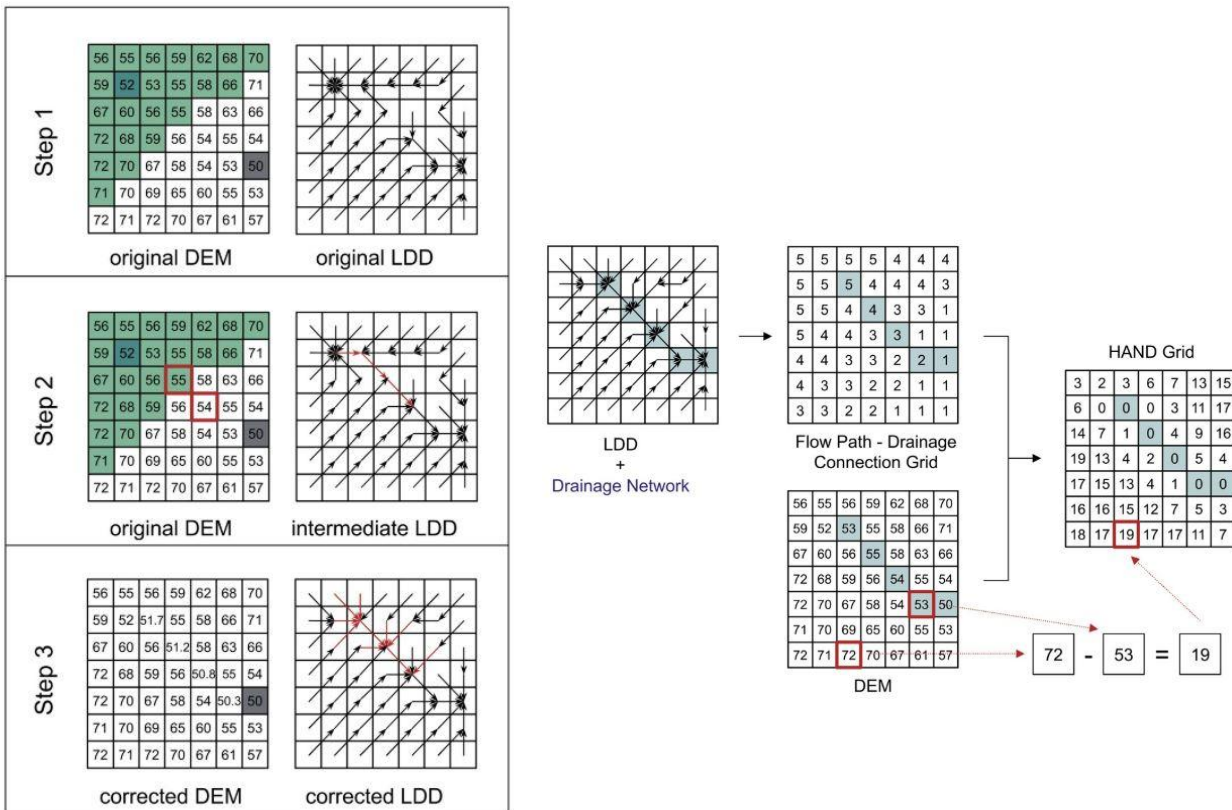


Figure 2-1 HAND development processes proposed by Rennó et al. (2008)

The HAND method uses a thresholding approach where an appropriate threshold value is defined to separate flooded and non-flooded prone areas (Chow et al., 2016). HAND grids with zero value indicate the drainage network, and HAND grids with values less than or equal to the threshold value are considered

flood-prone areas (Hu and Demir, 2021). Therefore, this study will define threshold height to delineate the susceptible areas to flooding, which will be used to reduce misclassified satellite-derived flood extent in the model domain. The quality of DEM products used (Rennó et al., 2008) and wrong threshold value selection can lead to either under or over-estimation of inundation extent areas (Chow et al., 2016).

## 2.3.    Satellite rainfall estimates

Rainfall is mainly an essential input in hydrological modeling. Rainfall can be measured using ground-based instruments (gauges and radar) and satellite-based sensors. In-situ measurements provide accurate rainfall data when well quantified, monitored, and spatially representative. However, the ground-based measurements lack the spatial representation of rainfall globally (Behrangi et al., 2011). Therefore, the uneven spatial distribution of rain gauges presents the scope application of satellite rainfall estimates in the hydrological models.

Satellite rainfall estimates (SREs) have been investigated in hydro-meteorological applications for different parts of the world (Ageet et al., 2022; Ashouri et al., 2016; Habib et al., 2014; Xue et al., 2013). SREs are estimated using sensors with infrared-based (IR) and passive microwave-based (PMW) techniques and their combination to record the rainfall. The IR-based method produces precipitation based on the top of cloud characteristics (temperature). The PMW-based technique uses ice particles or droplets concentrated in the atmosphere to estimate rainfall (Kidd et al., 2003; Vant-Hull et al., 2014). Various satellite rainfall products exist, like CMORPH[5], CHIRPS[6], TRMM-3B42[7], GPM-IMERG[8], etc. However, SREs possess uncertainties (i.e., random and systematic errors) in their measurements, producing erroneous results in the respective applications (Bakary et al., 2018). Therefore, a bias correction process is required to minimize the errors in the SREs.

The bias correction method is performed to improve the accuracy of SREs in the respective applications (Habib et al., 2014; Omondi et al., 2021). Different approaches have been evaluated where authors like Gumindoga et al. (2019) considered five bias correction approaches, namely Spatio-temporal (STB), elevation zone (EZ), power transform (PT), distribution transformation (DT), and quantile mapping based on an empirical distribution (QME) bias correction methods on CMORPH satellite product where they concluded that STB and EZ bias correction outperform other bias correction approaches. Habib et al. (2014) also assessed three sub-classes of the STB scheme, namely time-space variable (TSV), time variable (TV), and time-space fixed (TSF) on the CMORPH satellite product, where they deduced that the TSV reduces Bias in the CMORPH rainfall data. The bias-corrected satellite rainfall produces accurate streamflow in Ethiopia's Gilgel Abbey catchment.

Therefore, three satellite products (CHIRPS, CMORPH, and TAMSAT) will be analyzed to select one product that best represents rainfall in the Sebeya catchment, Rwanda. Then, the bias correction process was performed to reduce the propagation of errors in the hydrological model for the study area.

---

[5] Climate Prediction Center (CPC) Morphing technique
[6] Climate Hazards Group InfraRed Precipitation with Station data
[7] Tropical Rainfall Measuring Mission
[8] Integrated Multi-satellite Retrievals for Global Precipitation Measurement

## 2.4. Rainfall-runoff modeling

Hydrological models are a simplified representation of real-world characteristics through mathematical equations, several parameters, catchment characteristics, meteorological forcing, and other climatic variables (Devia et al., 2015). They provide information for water resources, environmental managers, hydroelectric projects, irrigation, flood mitigation practitioners, etc. Hydrological models can be grouped based on the process to be modeled, the model structure, model application, available input data for modeling, model approach, and mathematical equations applied (Becker and Serban, 1990). According to Rientjes (2016), hydrological models can also be classified as conceptual, empirical, and physical-based, depending on the model approach. Furthermore, each hydrological model can be divided into subclasses where a model can be classified as lumped, semi-distributed, and distributed based on the model's spatial representation.

The physical-based model considers the understanding of physical processes of the real world by applying mathematical equations that are derived from the conservation of mass, momentum, and energy to simulate the processes of the hydrological approach. Empirical model approaches do not consider the physical characteristics of the real-world features; hence they are based on the observations and input-output relations of the processes to be modeled. Empirical approaches often are applied in ungauged areas when rainfall and streamflow data time series are available while information on the study area is limited. On the other hand, conceptual model approaches involve relatively simple mathematical relations to simulate real-world processes. Conceptual approaches use semi-empirical equations and model parameters that are determined through calibration against observed streamflow to simulate real-world hydrologic phenomena (modified after Rientjes (2016)).

Moreover, depending on the spatial discretization of the catchment system, the hydrological model is considered lumped when spatial variations of processes and characteristics are ignored over the entire model domain (catchment). A semi-distributed model divides the catchment into sub-basins of different sizes based on the topography within the catchment. Each subbasin unit has its set of model parameters and state variables (hydro-meteorological data). On the other hand, distributed models describe the real-world characteristics in the elaborated way where the model domain is discretized into the same or different grid cell sizes, for which model parameters are assigned (Godara et al., 2019). Rainfall-runoff models often apply conceptual model approaches (Rientjes, 2016). Several hydrological model software packages exist, including HEC-HMS, MIKE-SHE, SWAT, and HBV.

Therefore, a semi-distributed conceptual Hydrologiska Byråns Vattenbalansavdelning (HBV) model will be used in this research to simulate the hydrologic behavior of the Sebeya catchment. The HBV model was selected due to its simple structure and moderate input data required (Sælthun, 1996). Several authors like Mendez and Calvo-Valverde (2016) used HBV to predict the streamflow of the river catchment. The estimated runoff from upstream will be used as inflow for the model domain in the flood model.

## 2.5. Hydrodynamic modeling

Hydrodynamic distributed flood modeling serves to assess spatial patterns of flood extend, flood depth, flow velocity, and flood duration in the main river reach and inundated areas (Costabile et al., 2020). Hydrodynamic models solve a set of finite difference equations using mass and momentum conservation principles to describe the flow dynamics across all wetted grid elements that constitute river channels and floodplains (Ongdas et al., 2020). Flood models may serve as simulations of flood hazards, inundation-prone areas, and flood mitigation strategies for flood management practitioners. These models apply concepts of

1D, 2D, or coupled 1D2D to simulate flow characteristics (duration, extent, depth, and velocity). The 1D hydrodynamic model estimates flood flow in channels or open floodplain areas with only cross-section data as geometry input (Yalcin, 2018). The 2D hydrodynamic model describes inundation patterns in floodplains in both directions (longitudinal and lateral) (Quirogaa et al., 2016). 1D and 2D models can be combined in a coupled 1D2D hydrodynamic model where the river and floodplains in urban areas are modeled together (Timbadiya et al., 2015).

Zainalfikry et al. (2020) revealed that the 1D hydrodynamic model performs sufficiently to simulate flooding in the Pahang River, Malaysia. However, it requires accurate river geometry data and presents difficulties in estimating inundations in complex floodplains, necessitating the introduction of a 2D hydrodynamic model. 2D hydrodynamic models use mesh patterns over the floodplain area to simulate flow paths in complicated topographic regions, particularly in urban areas (Yalcin, 2018). Liu et al. (2015) found that coupled 1D2D hydrodynamic model provides effective interactions of flow pathways between the channel and floodplain during urban flooding simulations. Several software packages, like MIKE FLOOD, SOBEK, HEC-RAS, etc., have been extensively applied in the flood simulation for channels and floodplains.

HEC-RAS hydrodynamic model tool was selected in this research to simulate inundation patterns in the semi-urban flood model domain located in the downstream part of the Sebeya catchment. The tool was selected because of its ability to depict flood using a 1D or 2D hydrodynamic model independently or in the coupled 1D-2D form model approach. The main inputs in the hydrodynamic model are topographic representation, channel cross-sections, land cover representation, and boundary conditions.

### 2.5.1. Topographical representation

The topographic data in a digital elevation model (DEM) is one of the essential input data in the hydrodynamic model to describe the geometric representation of floodplain and river channels (Md Ali et al., 2015). DEM is represented by grids where the pixel value of each grid shows the height of the terrain above a datum (Hawker et al., 2018). Different techniques exist to generate DEMs, including topographic surveys, Light Detection and Ranging (LiDAR), photogrammetry, and interferometric method (Mesa-Mingorance and Ariza-López, 2020). These methods extend from high resolution and accurate but expensive technique, LiDAR, to publicly available global, inexpensive and medium resolution data from Shuttle Radar Topography Mission (SRTM) and Advanced Spaceborne Thermal Emission and Reflection Radiometer (ASTER) (Md Ali et al., 2015).

DEM products' spatial resolution and vertical accuracy uncertainties introduce challenges in flood inundation modeling (Merwade et al., 2008). Watson et al. (2015) reveal that the flood inundation extent and depth characteristics change in the hydrodynamic model subject to applied variable DEM products and their quality and irregular channel representation in the floodplain. Cook and Merwade (2009) and Md Ali et al. (2015) revealed that finer resolution DEMs generate precise and effective inundation maps compared to coarse spatial resolution DEMs, which, at grid element scale, tend to overestimate inundation extents. Ali (2016) also demonstrated that DEM resolution and its accuracy influence the inundation extent simulated in flood models. Therefore, topographic terrain data with accurate surface features (river channels, roads, etc.) representation in the floodplain is necessary to produce reliable flood model results. In this study, the local DEM product collected from RWB, 10m× 10m spatial resolution, will be investigated for application in the hydrodynamic model.

# 3. STUDY AREA AND DATASET

## 3.1. Study Area

Sebeya catchment, with an area of 215.4 km², is the study area of this research and is located in the North-Western part of Rwanda. The catchment is a part of the Congo-Kivu catchment and covers parts of the Rubavu, Rutsiro, and Ngororero districts. Sebeya catchment has an average annual rainfall of above 1200 mm with an average temperature of 20°C (Hakorimana et al., 2019). Figure 3-1 shows the location of the Sebeya catchment. The primary stream of the catchment is the Sebeya river, with a total length of about 48 km. The river is the source of the water treatment plant and different hydropower plants for domestic and commercial use. The catchment was selected for this research due to the recurrent floods in its downstream part.
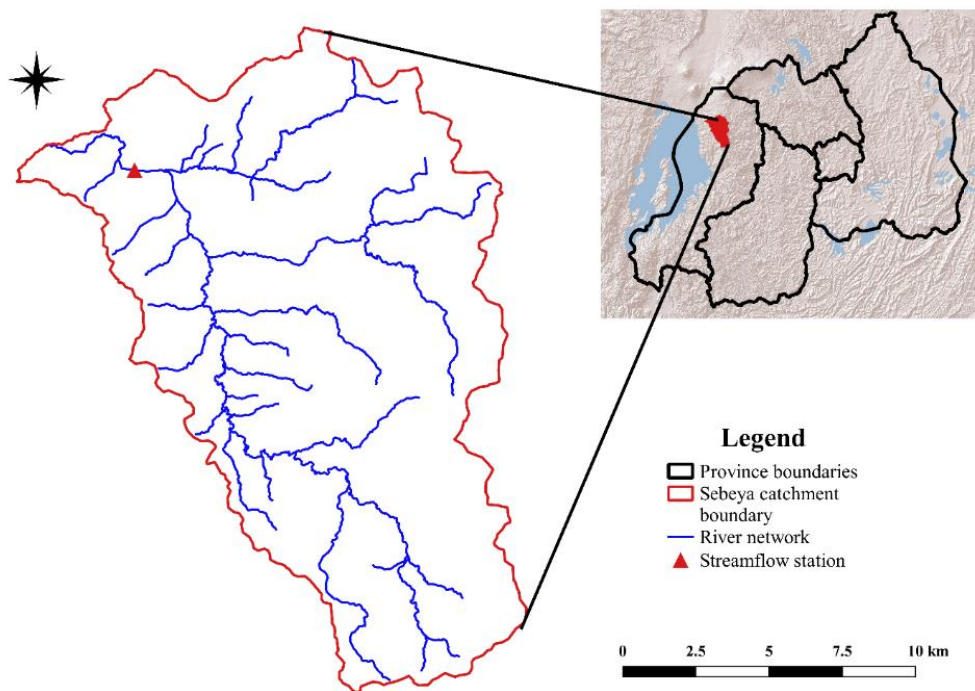


Figure 3-1 Location map of Sebeya catchment

## 3.1.1. Flood model domain concept

The Sebeya river is the main river of the catchment. A hydrodynamic model will be developed covering flood-prone areas, thus considering the model domain. The model domain considers the low and flatlands areas of the Sebeya catchment, covering the frequently flood-prone areas of Mahoko Centre and tea plantations. The flood model domain was delineated attentively to adequately present floodplain areas, with an area of about 5 km². The inflow boundaries representing streamflow from upstream areas will be estimated using the rainfall-runoff model, which will be developed in this research. The location of the model domain is shown in Figure 3-2.
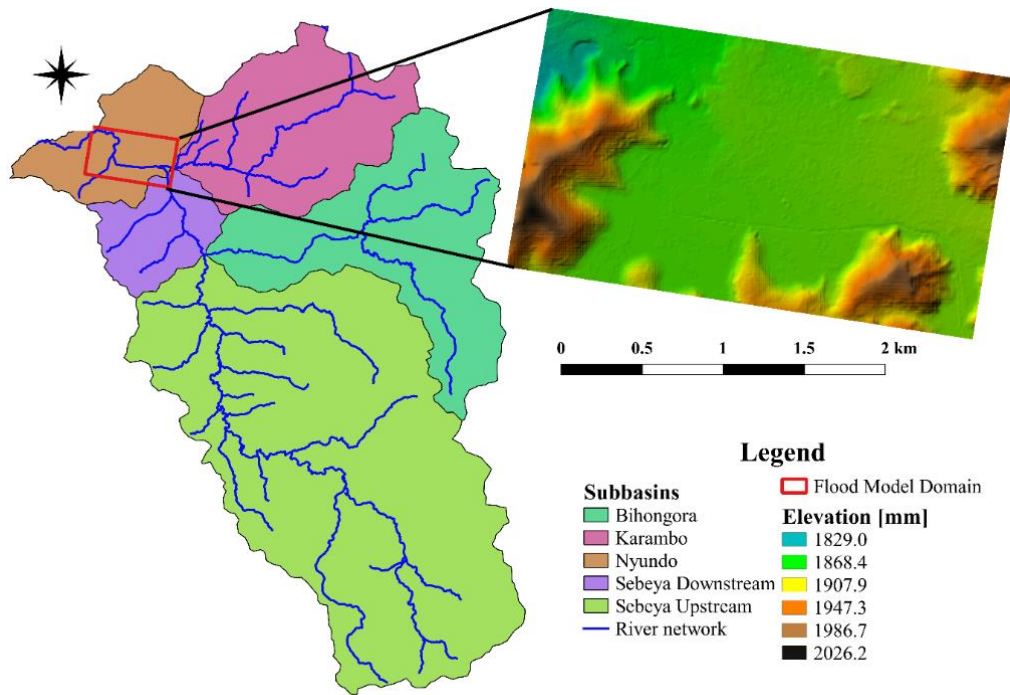
Figure 3-2 Location of the selected model domain

## 3.2.    Datasets

Sebeya catchment experienced recurrent flooding in recent years (2018, 2020, and 2021) for Mahoko market Centre but there are no in-situ recordings of these flood events. Therefore, this study intends to develop a hydrological and hydrodynamic flood model to understand the causes and extent of these flood events. Various types of data were used in this study, including hydro-meteorological data, topographic data of the catchment and flood model domain, land use/land cover, and satellite remote sensing data (Planetscope optical satellite images).

### 3.2.1.    Optical Satellite-based surface water

Earth observation satellites are extensively used in surface water bodies mapping and monitoring because they provide available, open-source, and inexpensive data (ABAZAJ, 2019). The detection of inundation extent from satellite requires the knowledge of the time flood took place. For this study, flood windows were acquired from different newspapers to download an image from the year 2018 to 2021. Numerous satellite products have been investigated, from freely accessible (Landsat-8, Sentinel-2, and Sentinel-1) to commercial (SPOT-6&7, and WorldView-3) satellite images. Still, the clouds and unavailable images during flood events were the main challenges to acquiring optical satellite images. However, after more efforts, a Planetscope optical satellite image was obtained from online data archives during the flood window. Table 3-1 describes the details of the collected images.

Table 3-1 Details of the downloaded Planetscope images

| Satellite image | Bands | Spatial resolution (m) | Acquisition time | Cloud cover (%) | Condition |
|---|---|---|---|---|---|
| **Planetscope** | 4-bands (Red, Green, Blue, NIR) | 3 | 04/03/2018 | 15 | After flood |
| | | | 23/09/2017 | 0 | Before flood |

Following the flood event that occurred on the 3rd March 2018, around 4 PM along the Sebeya river (EFRC, 2018), the Planetscope image after flooding was acquired on the next day (4th March) in the morning (7 AM). The satellite image before the flood was taken five months before the flood event. Therefore, these images will be used to detect areas affected by flooding in the model domain.

### 3.2.1.1. Planetscope satellite images

The Planetscope satellite constellation comprises around 130 individual satellites that record optical images in the visible and near-infrared bands daily (Planet Labs, 2021). The Planetscope Analytic Ortho Scene images (PSScene4Band) were downloaded from the Planetscope Explorer repository (https://www.planet.com/explorer/). These images are orthorectified, radiometrically, sensor, and geometrically corrected products and projected to UTM map projection (Planet Labs, 2021). All images (before and flood) were Surface Reflectance (SR) products in a GeoTiff format where SR values are scaled by 10,000 (Planet Labs, 2020). Details of acquired images are shown in Table 3-1, and Table 3-2 represents the specifications of Planetscope Ortho Scene images.

Table 3-2 Planetscope Analytic Ortho Scene image characteristics (source: (Planet Labs, 2021) )

| Product Attribute | Description |
|---|---|
| **Information Content** | |
| Analytic Bands | 3-band multispectral image (red, green, blue)<br>4-band multispectral image (blue, green, red, near-infrared) |
| Ground Sample Distance | 3.7 m (average at reference altitude 475 km) |
| **Processing** | |
| Pixel Size (orthorectified) | 3.0 m |
| Bit Depth | Analytic (DN): 12-bit<br>Analytic (Radiance - W m-2 sr-1 μm-1): 16-bit<br>Analytic SR (Surface Reflectance): 16-bit |
| Geometric Corrections | Sensor-related effects are corrected using sensor telemetry and a sensor model. Spacecraft-related effects are corrected using attitude telemetry and the best available ephemeris data. Orthorectified using GCPs and fine DEMs (30 m to 90 m posting) to <10 m RMSE positional accuracy. |
| Positional Accuracy | Less than 10 m RMSE |
| Radiometric Corrections | • Conversion to absolute radiometric values based on calibration coefficients<br>• Radiometric values scaled by 100 to reduce quantization error<br>• Calibration coefficients are regularly monitored and updated with on-orbit calibration techniques. |
| Atmospheric Corrections | • Conversion to top of atmosphere (TOA) reflectance values using at-sensor radiance and supplied coefficients.<br>• Conversion to surface reflectance values using the 6SV2.1 radiative transfer code and MODIS NRT data.<br>• Reflectance values are scaled by 10,000 to reduce quantization error. |

### 3.2.2. Topographic data

The DEM products generally provide information on the river channel and floodplain terrain in hydrologic and hydraulic modeling (Manyifika, 2015; Tarekegn et al., 2010). DEM data from two sources will be used in this research, ALOS-PALSAR for the hydrological model and local DEM in the hydrodynamic model. The DEM product was used to generate elevation zones for the hydrological model. Besides, it was imported into the hydrodynamic flood model for topographic representation.

The digital elevation model (DEM) used in the hydrological model for this study is the Advanced Land Observing Satellite/Phased Array type L-band Synthetic Aperture Radar (ALOS-PALSAR) DEM downloaded from Alaska Satellite Facility (ASF) website ( https://search.asf.alaska.edu/#/ ). The DEM consists of a 12.5m × 12.5m grid cell size. The topography of the Sebeya watershed extends from 1675 to 2930 m a.s.l based on the ALOS-PALSAR DEM product (see Figure 3-3), where the most significant parts, in its north and eastern regions, are dominated by high elevations and flatlands in the downstream area where frequent floods occur. Almost 80% of this land (particularly in the east of the catchment) is of high altitude (above 2000 m a.s.l.).

The local DEM product, 10m × 10m spatial resolution, will be used in the hydrodynamic model and collected from RWB. This product covered the whole country and resulted from the Rwanda Land Use and Development Plan project that used 0.25m × 0.25m grid size orthophoto images (Manyifika, 2015). However, the DEM presents errors in both horizontal and vertical directions, which could be a source of uncertainties introduced in flood inundation modeling (Merwade et al., 2008). Therefore, the DTM was enhanced to refine the terrain and represent surface features.

### 3.2.3. Land use/Land Cover

Land cover is an essential input in the HBV hydrological model. Land cover data for the Sebeya catchment were acquired from a 10m × 10m resolution ESA WorldCover map prepared in 2020 and released in 2021. Sebeya catchment contains seven land cover classes where the grassland is dominated throughout the area, followed by forest and croplands. The built-up areas are observed in the downstream part of the catchment because of the Mahoko Center, a dynamic town with regular traffic and trade, leading to the town's growth, thus increasing flood risk and vulnerability.

Manning's coefficient (n) represents the surface roughness, the resistance of river channels, and floodplain to flows (J.Arcement and Schneider, 1989). Surface roughness will be determined by the land use data extracted by classifying available orthophoto images. Optimal surface roughness is mainly estimated through the calibration process of the hydrodynamic model to get the best model performance (Liu et al., 2019). Abbas et al. (2020) and Garrote et al. (2021) use calibrated Manning's coefficient in flood modeling and reveal that calibrated model with surface coefficient produces an acceptable correlation between simulated and observed flood extent.
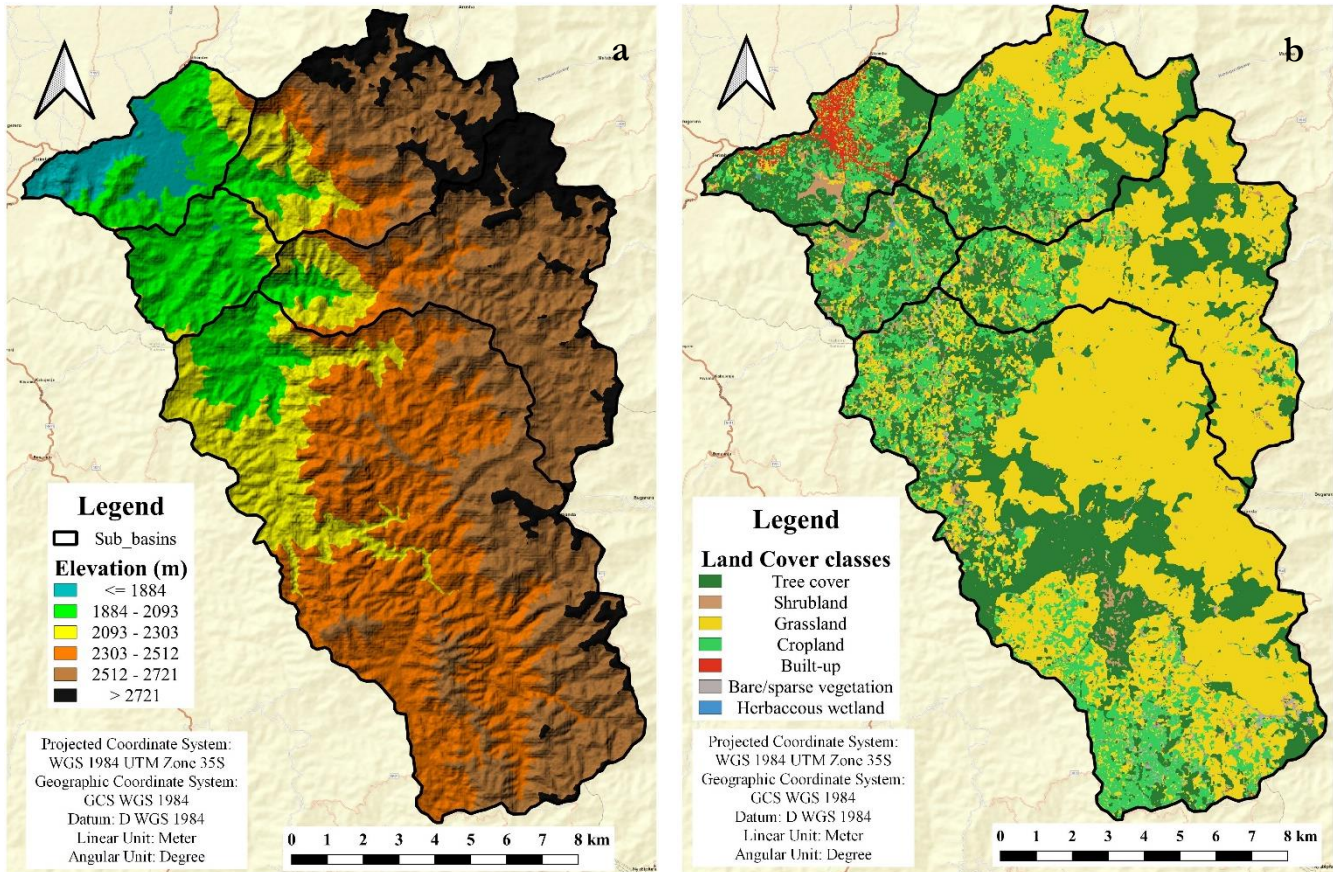
Figure 3-3 Topographic (a) and Land cover (b) maps of Sebeya catchment

### 3.2.4. Rainfall data collected

#### 3.2.4.1. InSitu rainfall data

Daily meteorological data were collected from RMA, which includes rainfall data. Among 11 rainfall stations provided, five stations were used in this study because they are close to the Sebeya catchment (Figure 3-4). This study used the Thiessen polygon method to generate a spatial representation of In-Situ meteorological data on the Sebeya sub-basins. Therefore, the meteorological data for each sub-basin was estimated using the influence fraction of each station on the sub-basin using QGIS software.
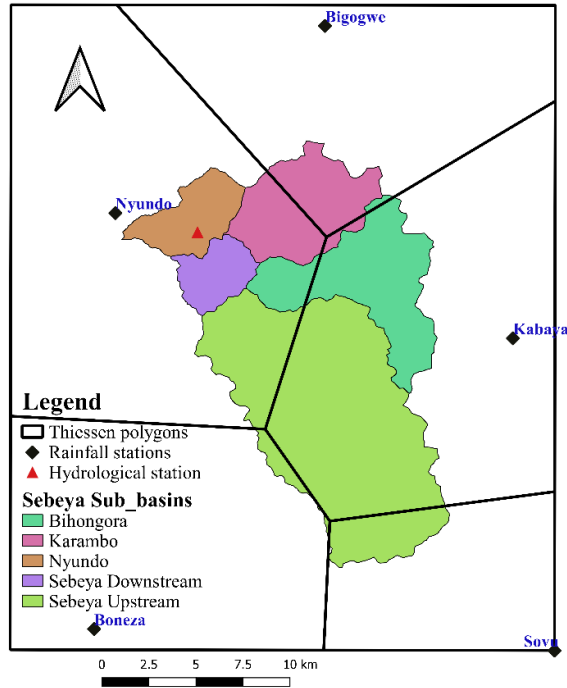
| Name | Longitude | Latitude | Elevation [m] |
|---|---|---|---|
| **Boneza** | 29.3 | -1.9 | 1632 |
| **Nyundo** | 29.31 | -1.7 | 1690 |
| **Bigogwe** | 29.41 | -1.61 | 2408 |
| **Kabaya** | 29.5 | -1.76 | 2442 |
| **Sovu** | 29.52 | -1.91 | 2335 |

Figure 3-4 Rainfall stations and their description

### 3.2.4.2. Satellite rainfall data

Three satellite rainfall products were evaluated in this study, as shown in Table 3-3. The SRE products were selected based on their high spatial and temporal resolutions, broad temporal coverage, and freely and easily accessible datasets.

**CHIRPSv2 dataset**

Rainfall data from CHIRPS produced by combining remote sensing and rain gauge stations were evaluated in this research. The United States Geological Survey (USGS) and the Climate Hazards Group at the University of California, Santa Barbara, developed the CHIRPS dataset, where they combine pentadal precipitation climatology, quasi-global geostationary TIR satellite observations from the Climate Prediction Center (CPC), and the National Climatic Data Center (NCDC), atmospheric model rainfall fields from the NOAA Climate Forecast System version 2 (CFSv2), and in situ rainfall observations (Funk et al., 2014). The product is available at 0.05° spatial resolution and at daily, pentad, and monthly temporal resolution. CHIRPS product extends over 50°S and 50°N and contains gridded rainfall time-series data from 1981 to the near-present. The daily CHIRPSv2 rainfall data was extracted from https://data.chc.ucsb.edu/products/CHIRPS-2.0/africa_daily/tifs/p05/.

Table 3-3 Description of satellite rainfall products used in this study

| Satellite product | Spatial | | Temporal | | File format | References |
|---|---|---|---|---|---|---|
| | **Resolution** | **Coverage** | **Resolution** | **Coverage** | | |
| **CHIRPSv2** | 0.05° ≈ 5 km | 50°N - 50°S Global | Daily | 1981-Present | GeoTiff | (Funk et al., 2014) |
| **CMORPH** | 0.0727° ≈ 8 km | 60°N - 60°S Global | ½ hourly | 1998-Present | ILWIS | (Joyce et al., 2004) |

| **TAMSATv3.1** | 0.0375° ≈ 4 km | Africa continent | Daily | 1983-Present | netCDF | (Maidment et al., 2017) |
|---|---|---|---|---|---|---|

**CMORPH dataset**

The CMOPH product provides rainfall using a morphing approach where PMW rainfall observations and IR brightness temperature from different satellites are combined to retrieve rainfall estimates. The 8km × 8 km spatial resolution rainfall estimates are determined from different sensor types where rainfall is generated at 30min periods from forward and backward weighted interpolation of PMW-measured estimates recording the shape and intensity of rainfall estimates at a particular location (Joyce et al., 2004). CMORPH rainfall estimates are available at 8 km × 8 km grid resolution for ½ hour and hourly time scale and at 25 km × 25 km daily and weekly. The data were downloaded through ILWIS software using ISOD Toolbox from 2014 to 2018. The ½ hourly data were aggregated daily to match the time step of rain gauges and other satellite products.

**TAMSATv3.1 data**

The Tropical Applications of Meteorology using Satellite and ground-based observations (TAMSAT) version 3.1 rainfall product was also used in this research. The TAMSAT product uses Meteosat thermal infrared (TIR) and ground-based rainfall data for calibration. The algorithm used in the TAMSAT is based on the cloud-indexing technique, where rainfall proxy is determined when cold cloud tops exceed a defined temperature threshold(Maidment et al., 2014; Tarnavsky et al., 2014). The daily TAMSAT estimates were assessed using daily ground-based rainfall data from five countries (Mozambique, Niger, Nigeria, Uganda, and Zambia) and other SREs products (CHIRPS, CHIRP, RFE, ARC, TMPA-3B42, and CMORPH) (Maidment et al., 2017). TAMSATv3.1 is available at approximately 4 km × 4 km spatial resolution and at daily, pentadal, decadal, monthly, and seasonal temporal scales. It contains data from 1983 to nearly present over the African continent. The daily data of TAMSAT were downloaded from http://www.tamsat.org.uk/data repository.

### 3.2.5. InSitu Rainfall Data pre-processing

Daily rainfall data from five stations were used in this study. There were no gaps in the data collected from 2014 to 2018. Double mass curve analysis was performed to check the consistency of the available rainfall stations. This method is estimated based on the cumulative daily rainfall of one station against the cumulative daily rainfall of neighboring stations (Manyifika, 2015). Figure 3-5 provides double mass curves of different stations, showing better consistency with a high correlation coefficient ($R^2 > 0.9$).
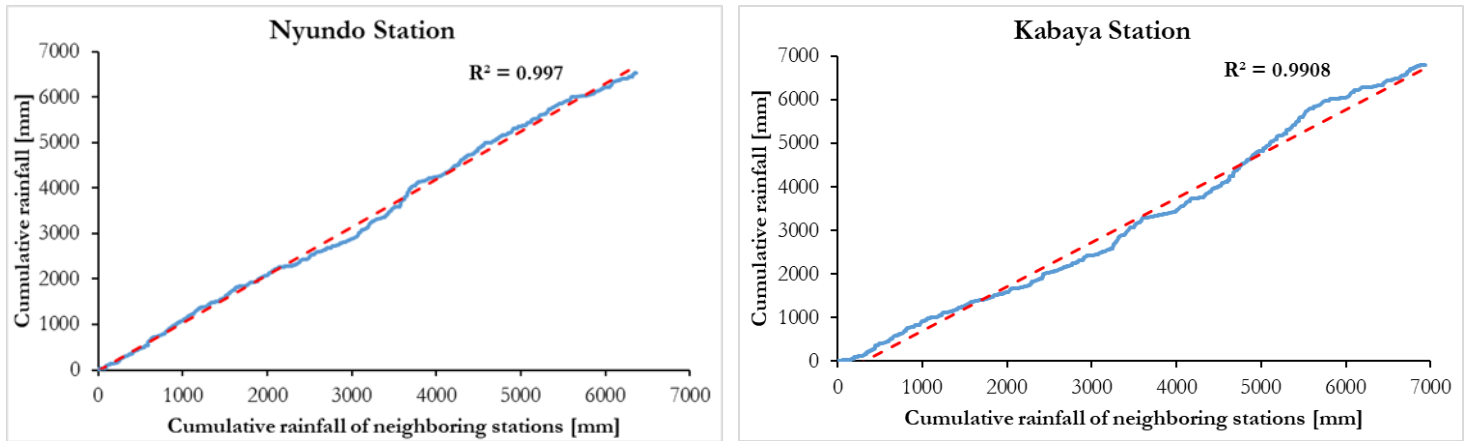
Figure 3-5 Double mass curve of some stations

Figure 3-6 presents the annual rainfall of selected rainfall stations for this study from 2014 to 2018. All the stations describe the consistency in the high amount of rainfall recorded with less rain in 2017. Boneza station shows high annual rainfall compared to other stations selected for this study.
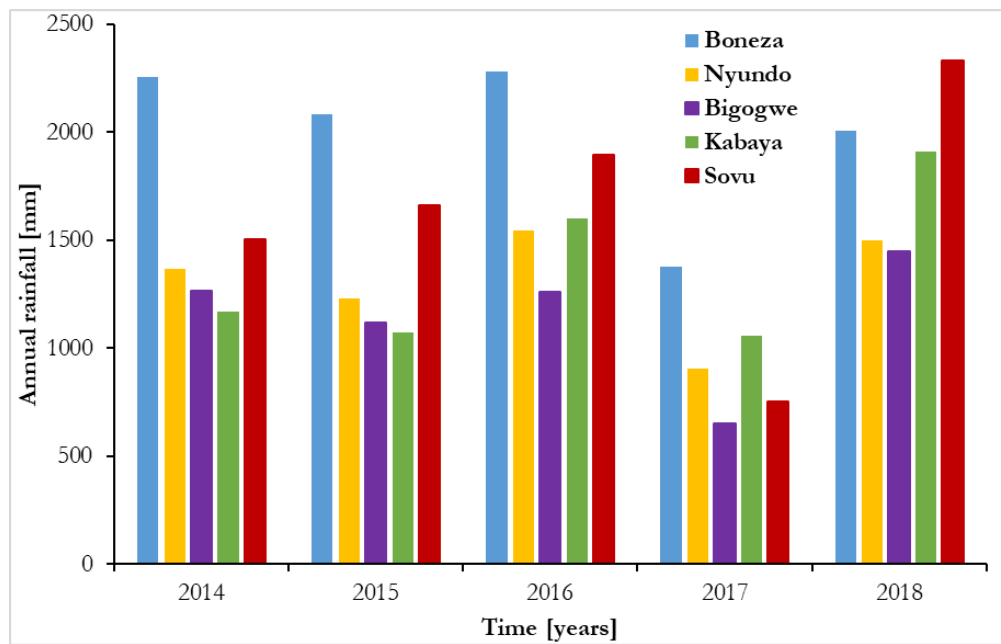


Figure 3-6 Annual rainfall for selected rainfall stations from 2016 to 2020

After selecting rainfall stations, the elevation-rainfall relationship was established, as shown in Figure 3-7 for the Sebeya catchment. It can be found that there is no relationship between the available rainfall stations and elevation based on the very low regression coefficient ($R^2 < 0.3$) and limited rain gauges (five rainfall stations). Therefore, the elevation-rainfall relation will not be applied to estimate rainfall over sub-basins.
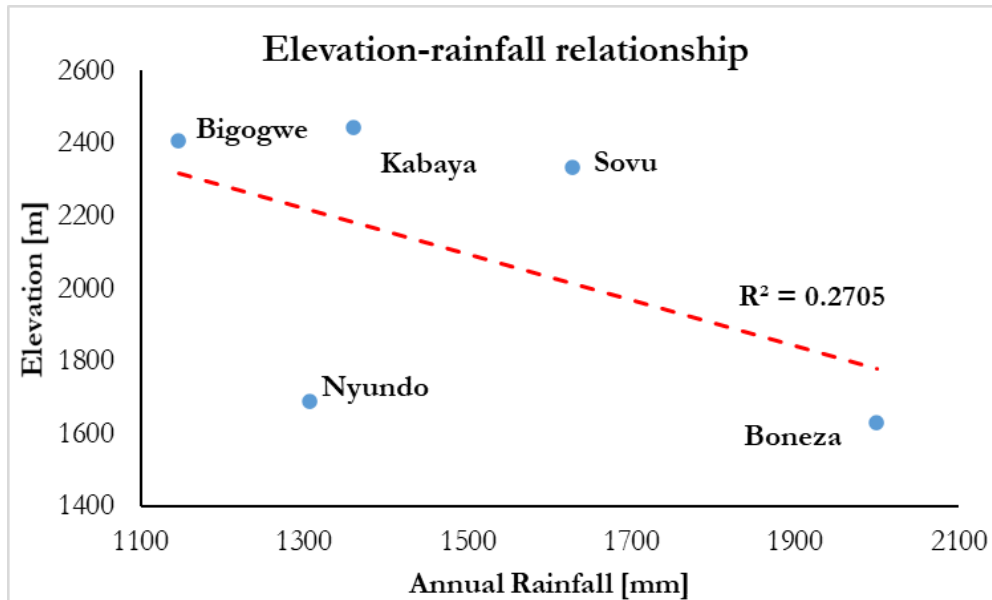
Figure 3-7 Elevation and rainfall relationship

### 3.2.6. Rainfall data consistency check

The available ground-based and satellite-based rainfall data were analyzed to determine the consistency of representing rainfall depth in the study area. Five rainfall stations and three satellite rainfall estimates were collected and acceptable for further operations. Nevertheless, some rainfall data depicts unreasonable values in recordings. The double mass curve was produced with all rainfall data from rain gauges and satellites, as it is shown in Figure 3-8. It is observed that Boneza and Sovu stations remarkably record high accumulated rainfall amounts compared to satellite rainfall estimates (SREs), i.e., SREs at those stations have much lower rainfall amounts. There is no information on the source of those effects, but they would be caused by erroneous data recorded on Boneza and Sovu rain gauges. Therefore, the remaining three stations were selected for further applications in the bias-correction process and hydrological modeling because of their consistent rainfall recordings.

On the other hand, collected SREs were checked for consistency before their applications. CMORPH satellite product typically underestimates accumulated rainfall amount in the selected rainfall stations. Therefore, the CMORPH product was excluded from further use as the product was considered nonrepresentative for the Sebeya catchment. The exclusion is unexpected because of its technique for recording rain (combination of infrared and passive microwave) and better performance compared to ground observations observed in different areas (Awange et al., 2016; Dinku et al., 2007; Shen et al., 2010) and its application in rainfall bias correction and hydrological modeling (Bhatti et al., 2016; Habib et al., 2014). However, the same underestimation of CMORPH SRE was found by Rahmawati et al. (2021), who indicated the larger underestimation of CMORPH satellite products compared to other satellite rainfall products. Therefore, the CHIRPS and TAMSAT SREs are selected for further use and application in hydrological modeling.
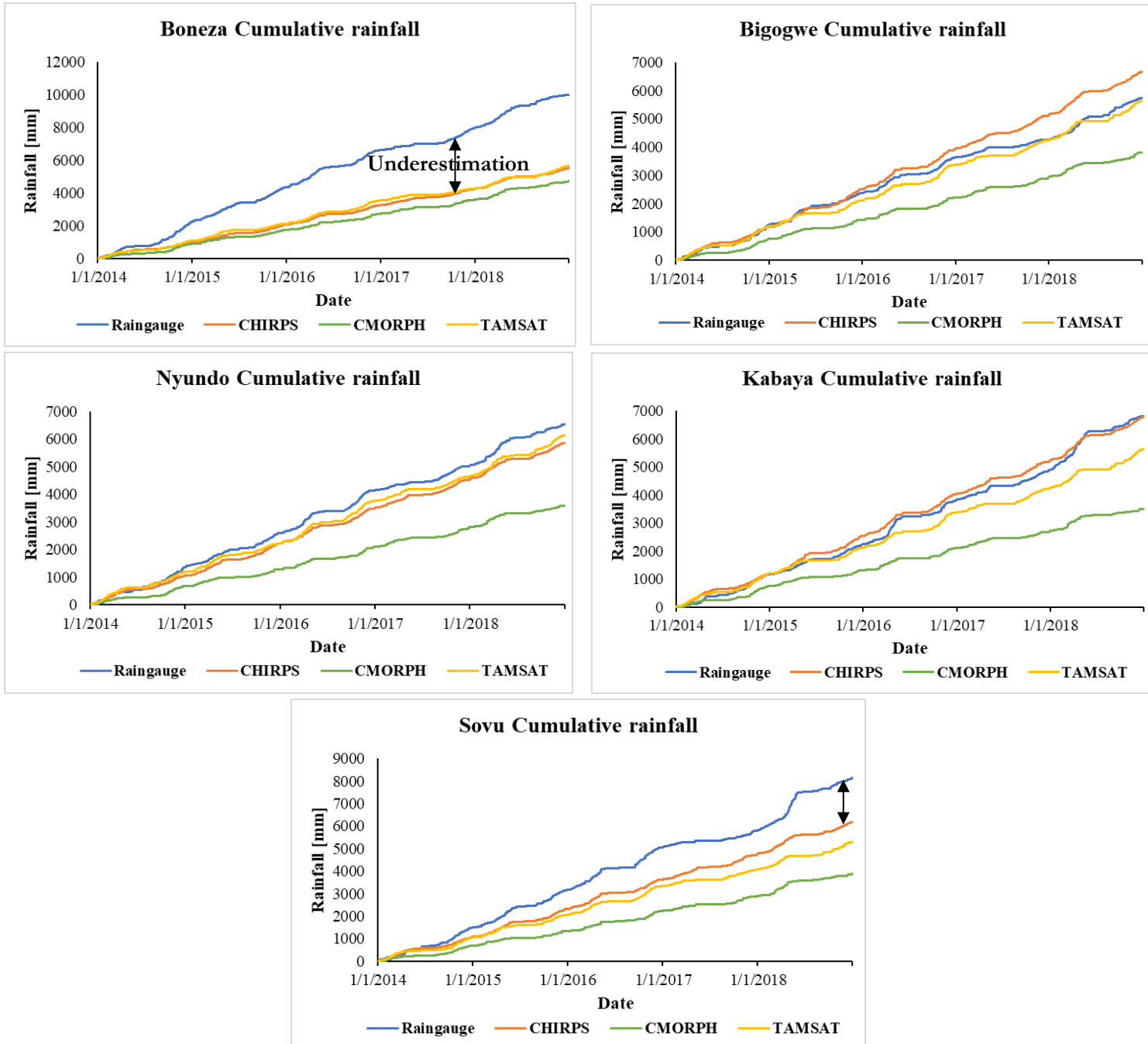
Figure 3-8 Accumulated rainfall for each rain gauge station with corresponding satellite-based rainfall amount

### 3.2.7. Temperature and potential evapotranspiration products

Potential evapotranspiration (PET) data is another input required for HBV hydrological model. The PET file may include either long-term monthly mean values, long-term daily mean values, or one value for each day following the PTQ-file time steps (Seibert, 2005). Long-term monthly PET values were used for this study as input for the hydrological model. PET values were acquired from the EarthData website (https://appeears.earthdatacloud.nasa.gov/) using the Application for Extracting and Exploring Analysis Ready Samples (AppEEARS) technique. The AppEEARS uses MOD16A2 of an 8-day composite product at 500m pixel size. The MOD16A2 data product is based on the Penman-Monteith equation.

The temperature data were obtained from Rwanda-Meteo, where the minimum and maximum daily temperatures for three stations (Bigogwe, Gisenyi-Aero, and Sovu) were provided. Therefore, the average between the minimum and maximum values was calculated from those three stations for the hydrological model.
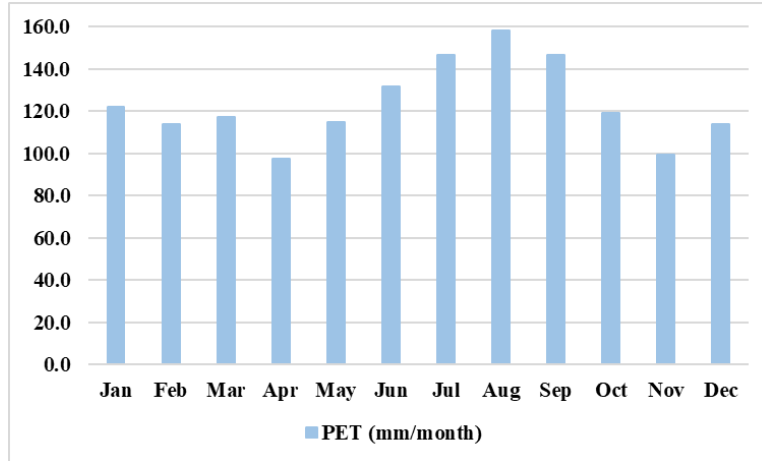


Figure 3-9 Monthly Long-term potential evapotranspiration (2015-2020)

### 3.2.8. Hydrological data analysis

Water level and flow discharge data for the Nyundo station were collected from the RWB water portal. It is necessary to have discharge data to calibrate the hydrological model. The available field visit measurements of water level and discharge were used to establish a stage-discharge relationship. There is a telemetry (Figure 3-10) instrument that records stage data on the river that were downloaded from the RWB portal with data from the 2018 to 2020 period. After establishing the stage-discharge relation, the available water level data were converted into flow discharge using Equation 3-1.
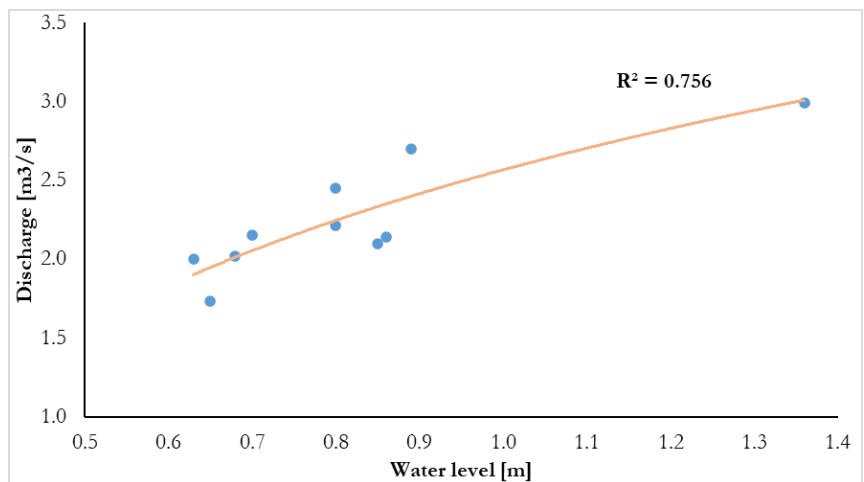


Figure 3-10 Location of Sebeya river gauging station and stage-discharge relation at Nyundo station

$$Q = C * (h + a)^b$$

Equation 3-1

Where Q is the discharge [m³/s], h is water level [m], a is the water level at zero flow, and C and b are calibration coefficients. C is the discharge at the effective flow depth (h + a) of 1, and b is the logarithmic slope of the rating curve. Manyifika (2015) provided detailed information on the estimation of a, C, and b coefficients in the annex. After computation of those coefficients for the Nyundo hydrological station, the

stage-discharge relation was deduced as illustrated in Equation 3-2. With Equation 3-2, the Sebeya streamflow time series (Figure 3-11) was obtained based on the available water level from 2018 to 2020.

$$Q = 1.968801 * (h + 0.35)^{0.831571}$$    Equation 3-2
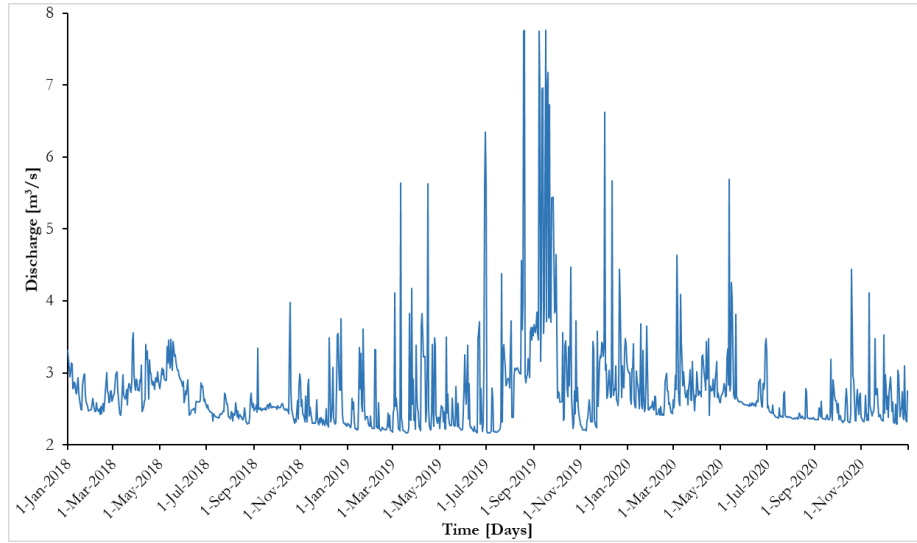


Figure 3-11 Sebeya river discharge data

### 3.2.8.1. Consistency analysis of hydrological data

The analysis of the available discharge data is required to understand the rainfall response for the Sebeya catchment with respect to the flow at the Nyundo gauging station. This approach was developed and proposed by Rientjes et al. (2011), indicating that an increase or reduction of rainfall should match with an increase or decrease in flow discharge for a selected area. The method is applied to remove the outliers in the flow discharge. Therefore, the outliers were adjusted to remove erroneous data in streamflow datasets. Following the study of Manyifika (2015), the ratio values ranging beyond -10 to +10 were corrected in the streamflow data to produce consistent streamflow for the Sebeya river. The increment differences of rainfall and streamflow and the ratio of increments were estimated and plotted.

$$\Delta Q = Q_t - Q_{t-1} \quad \& \quad \Delta P = P_t - P_{t-1} \qquad \text{in [mm]}$$    Equation 3-3

$$Ratio = \frac{|\Delta P|}{\Delta Q}$$    Equation 3-4

Figure 3-12 shows the incremental differences in rainfall and observed streamflow for three years of datasets (2018-2020), from which we will deduce a flood event that took place on 3rd March 2018. The average rainfall from all available rainfall stations was used for this operation to represent the rainfall influence from all subbasins. On the ratio $|\Delta P|/\Delta Q$, a few outliers range from -10000 to 10000, and most outliers range from -500 to 500.
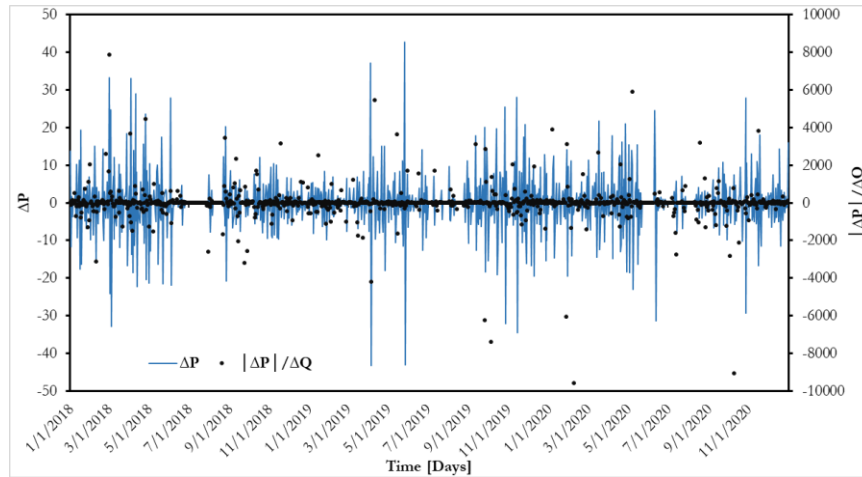
Figure 3-12 Sebeya river change ratios

Figure 3-12 necessitates the correction of observed streamflow time-series data. Hence, using Equation 3-4, observed streamflow data were corrected following the abovementioned conditions. However, elaboration of Equation 3-4 resulted in Equation 3-5, from which modified streamflow was estimated. Therefore, Equation 3-6 was used to estimate corrected streamflow, where a starting streamflow was taken from observed, and the ratio (-10 where there was a decrease in rainfall and +10 when there is an increase in rainfall) was inserted.

$$Ratio = \frac{\left|P^t - P^{t-1}\right|}{Q^t - Q^{t-1}} \qquad \text{Equation 3-5}$$

$$Q^t = \frac{\left|P^t - P^{t-1}\right| + ratio \times Q^{t-1}}{ratio} \qquad \text{Equation 3-6}$$

Where $P^{t-1}$ and $Q^{t-1}$ represents the rainfall and streamflow of the previous day, respectively. $P^t$ and $Q^t$ are rainfall and streamflow of the present day, respectively.

### 3.2.8.2. Corrected hydrograph

The errors in the available hydrograph were minimized to produce streamflow data used in the hydrological modeling in the Sebeya catchment. Figure 3-13 describes the corrected and modified hydrography for the Sebeya river during 2018.
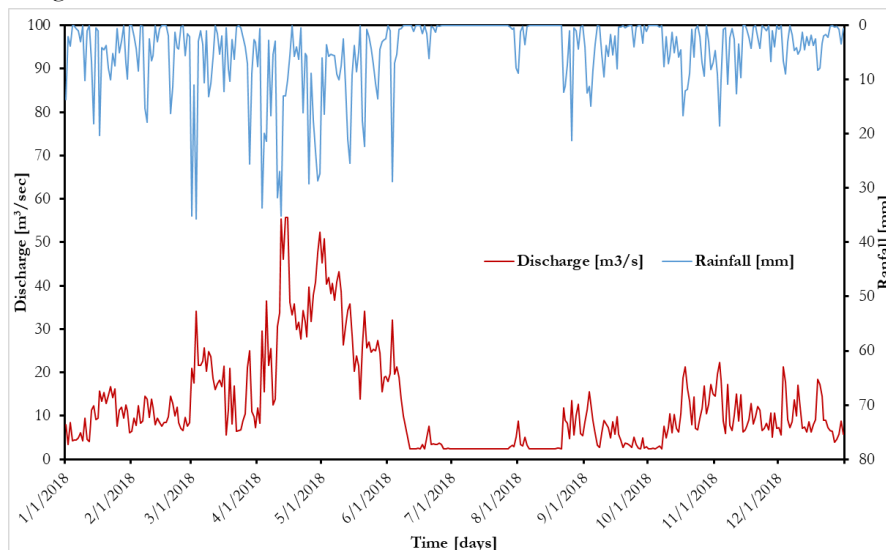


Figure 3-13 Sebeya River Corrected hydrograph

# 4. METHODOLOGY

## 4.1. DTM enhancement

Detailed analysis and enhancement of the available topographic data are essential in flood modeling to simulate reliable flood model results. Coarse-resolution and poor surface features' representative DEM products significantly affect the water depth, flood extent, and velocity estimated from the flood model. Therefore, a pre-processing of the available DEM was required to refine the terrain and represent surface features on the topographic data. Two approaches were tested in this study. The methodologies for the two approaches are depicted in Figure 4-1. The first approach considers resampling the original DEM (10m × 10m) to 1m × 1m for further operations on the DEM. Contours of 0.25m × 0.25m intervals were created to adjust the terrain in the flat floodplains before the available DEM was imported into the hydrodynamic model. After changing and correcting the contour elevations and positions, a TIN map was created using ArcGIS software. After that, the produced TIN was rasterized to 0.25 m resolution, which was resampled to 1, 5, and 10m grid size DEM to create a suitable terrain for hydrodynamic modeling.
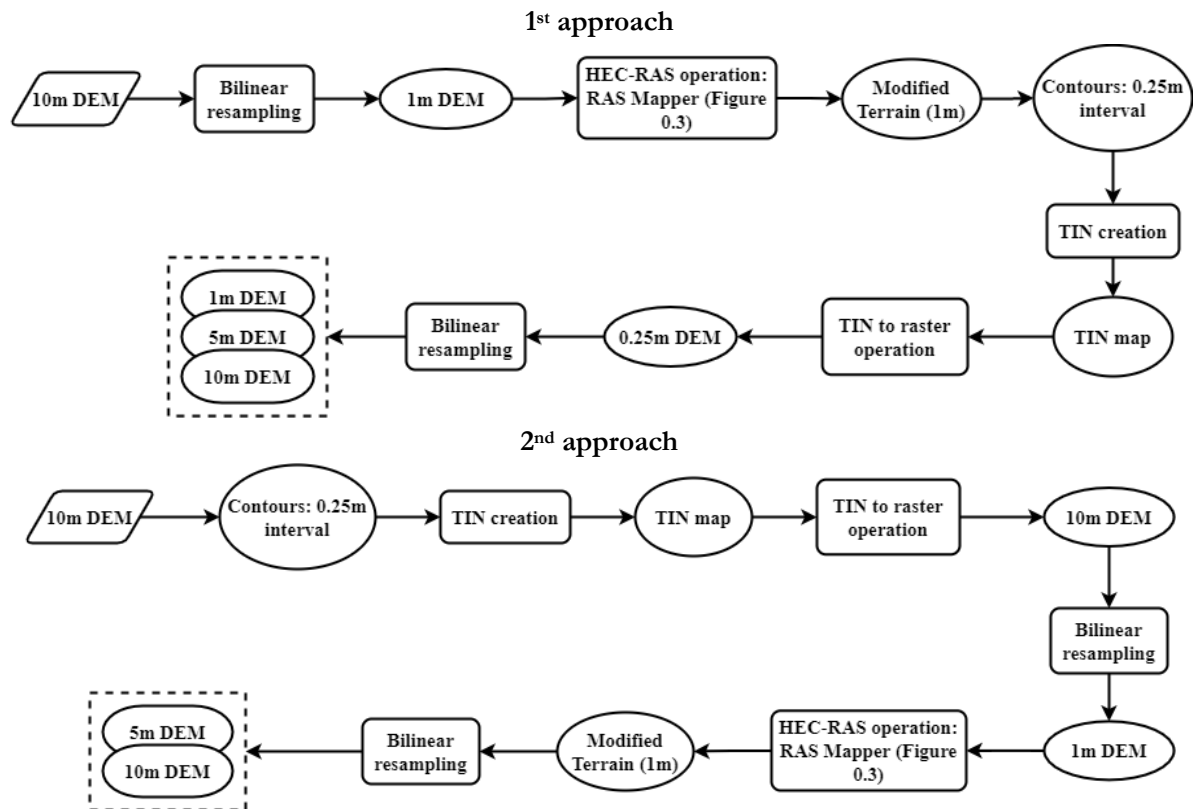


Figure 4-1 DEM enhancement process

The second approach considers the refinement of the original DEM (10m × 10m), where contours of 1m × 1m intervals were created to adjust the terrain in the flat floodplains before the available DEM was imported into the hydrodynamic model. Within the 1m interval contours, contours of 0.25m distance were added manually between each 1m interval, i.e., three contours were delineated at an equal distance between 1m interval contours. A TIN map was created using ArcGIS software after adding, changing, and correcting the contour elevations and positions. After that, the produced TIN was rasterized to 1m × 1m resolution, and the TIN can also be rasterized at different spatial resolutions. After that, 10m × 10m grid size DEM

was resampled to 1m × 1m DEM, which was imported in HEC-RAS to introduce the channel drainage to create a suitable terrain for hydrodynamic modeling. The modified topography (1m × 1m resolution) was resampled to 5m × 5m and 10m × 10m resolution DEMs to assess their description of surface features. The steps to delineate channels in HEC-RAS are described in Figure 4-2.

The HEC-RAS 6.1 using the RAS Mapper tool was used to modify the original topographic terrain. The terrain modification tools can create vectors like lines, shapes, and polygons, from which an elevation is specified to adjust the topography of the original terrain. In this case, a line vector format was created to modify the terrain of the main channel in the available topography. Therefore, the 1m × 1m spatial resolution DEM was imported into RAS Mapper to create a topographic terrain. It is better to create a virtual clone terrain on which the terrain modifications will be conducted, keeping the original topography unchanged.
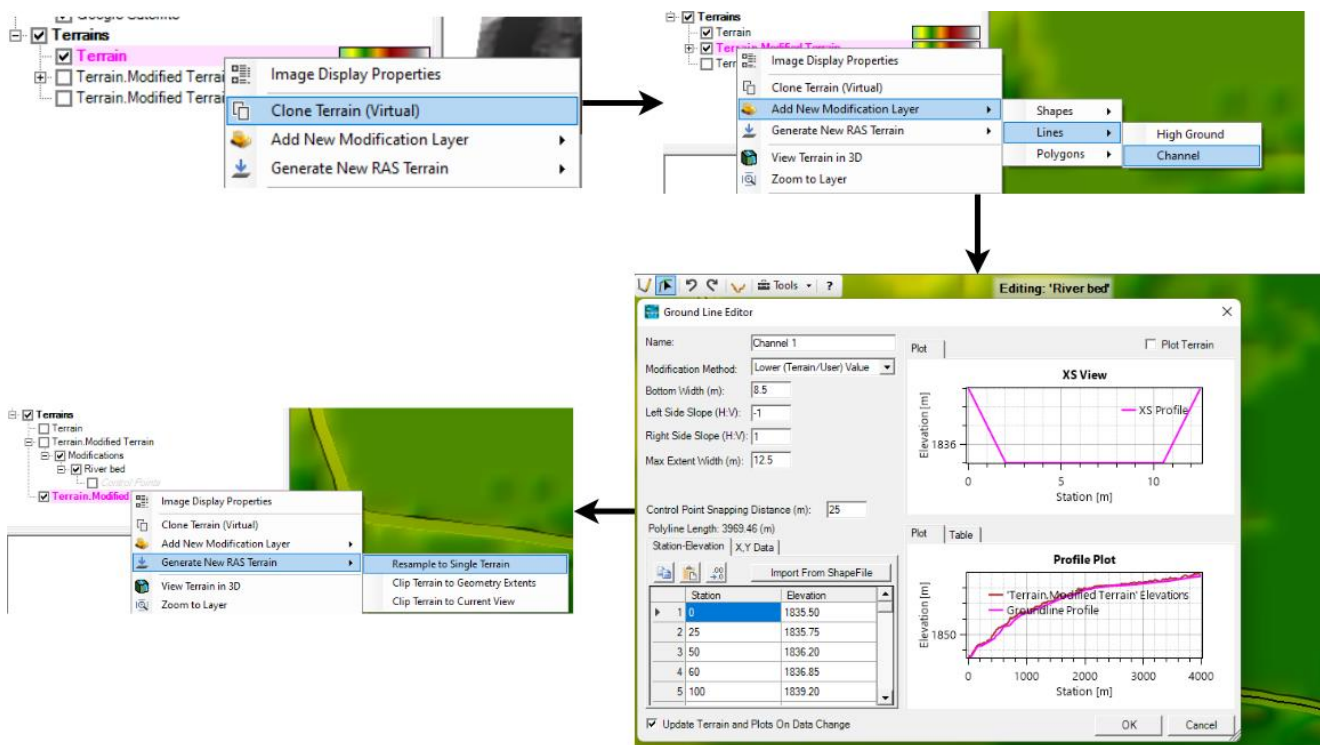


Figure 4-2 Steps of terrain modification in the RAS Mapper

Figure 4-2 indicates the steps involved in the terrain modification in HEC-RAS using the GIS RAS Mapper tool. In the new terrain modification layer, a river centreline is aligned following the channel on the google satellite image. Firstly, the start editing layers is selected to begin the definition of the river in the terrain by clicking on the starting point. In the ground line editor, a top width, max extent width, and right and left slope are defined based on the study area knowledge and observations on the satellite images to delineate a cross-section of the river channel. In the profile station and elevation data table, default elevation values can be edited to produce the river profile that follows the original terrain before modification. The steps indicated in Figure 4-2 can be used to modify the terrain by adding different surface features like roads, dams, or buildings to the original topography. After establishing the surface features (channel for this case), click on the stop editing to save the changes on the modified terrain. Therefore, a new topography can be saved in the raster format by combining the original and changed topographic terrain using resample to a single terrain tool (Figure 4-2). Table 4-1 describes the characteristics of river reach cross-sections used to introduce the river network in the original terrain.

Table 4-1 Characteristics of different river reaches used for terrain modification

| River characteristics | River reaches | | |
|---|---|---|---|
| | Sebeya downstream | Sebeya upstream | Karambo |
| Bottom width | 10 | 9 | 8 |
| Left side slope | -1 | -1 | -1 |
| Right side slope | 1 | 1 | 1 |
| Max extent width | 12 | 11 | 10 |

## 4.2. Planetscope flood mapping

The Planetscope satellite image for a flood event that occurred on 4th March 2018 was used in this study to extract inundation extent. But cloud cover in the study area for the respective acquisition date is a limitation in extracting appropriate surface water for use. The NDWI spectral index was suitable in this study to delineate surface water features based on the available Planetscope satellite images with four bands (indicated in Table 3-1), but the index produced unexpected inundation areas. The NDWI inundation extent results covered almost the whole model domain. Therefore, a change detection method was found to be another method that can be applied between the before and after flood images (Table 3-1) to identify pixels mostly affected after flooding. From this analysis, the vegetation index (NDVI) was selected for this study. Low values (below 0.1) of NDVI indicate bare lands, sand, water, and built-up areas. Moderate positive values (0.2-0.3) represent shrubs or grasslands, and high positive values describe vegetations and forests (Gandhi et al., 2015). NDVI images differencing method was performed in this study between before and after flood images. The difference image can track changes in the vegetation cover between two periods. The equations of NDVI and differencing method are described in Table 4-2.

Table 4-2 NDVI and change detection method applied

| NDVI | Differencing method |
|---|---|
| $\dfrac{NIR - Red}{NIR + Red}$ | $NDVI_{before} - NDVI_{after}$ |

NIR and Red in the NDVI formula are Near-Infrared and Red spectral bands of the Planetscope satellite images.
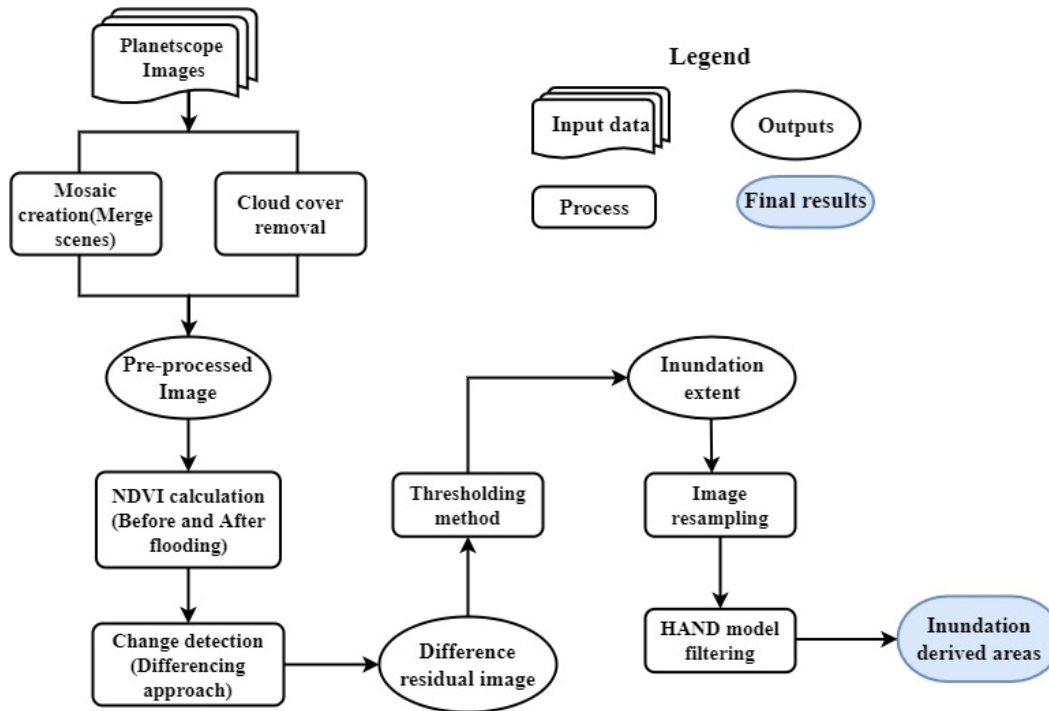
Figure 4-3 Planetscope flood extent mapping processes

A threshold value was selected to separate water and non-water features in the residual difference image. Pixels in the residual difference image with almost zero value indicate no change, and pixels with negative values represent an increase in vegetation in the two periods. High positive values in the residual difference image demonstrate areas affected by flood where vegetations change to soil (muds). Pixels close to water bodies were investigated to facilitate the threshold value selection in the residual image. The HAND output will be used to limit the inundation extent for flood-prone areas. The 3m × 3m spatial resolution Planetscope image was resampled to 1m × 1m resolution of the HAND model output. The majority filter tool was also applied to create a continuous flood extent in the model domain. All the data were processed using QGIS software.

## 4.3. Height Above Nearest Drainage (HAND) approach

The HAND approach describes the vertical distance between the grid point and the nearest pixel belonging to the drainage in the DEM, aiming to produce appropriate flood-prone area delineations. The satellite-derived flood extent from Planetscope was adjusted using the HAND model to differentiate non-water features from water surfaces better. Chow et al. (2016) apply the HAND approach to limit the misclassification of water and non-water features using a fixed threshold in HAND classes in different areas. The study revealed that the HAND model could improve the satellite-derived inundation extent. The enhanced DEM from the second approach of 1m × 1m spatial resolution DEM was used to create the HAND classes for the model domain. Figure 4-4 describes the steps and processes used to produce HAND using QGIS version 3.16.16.
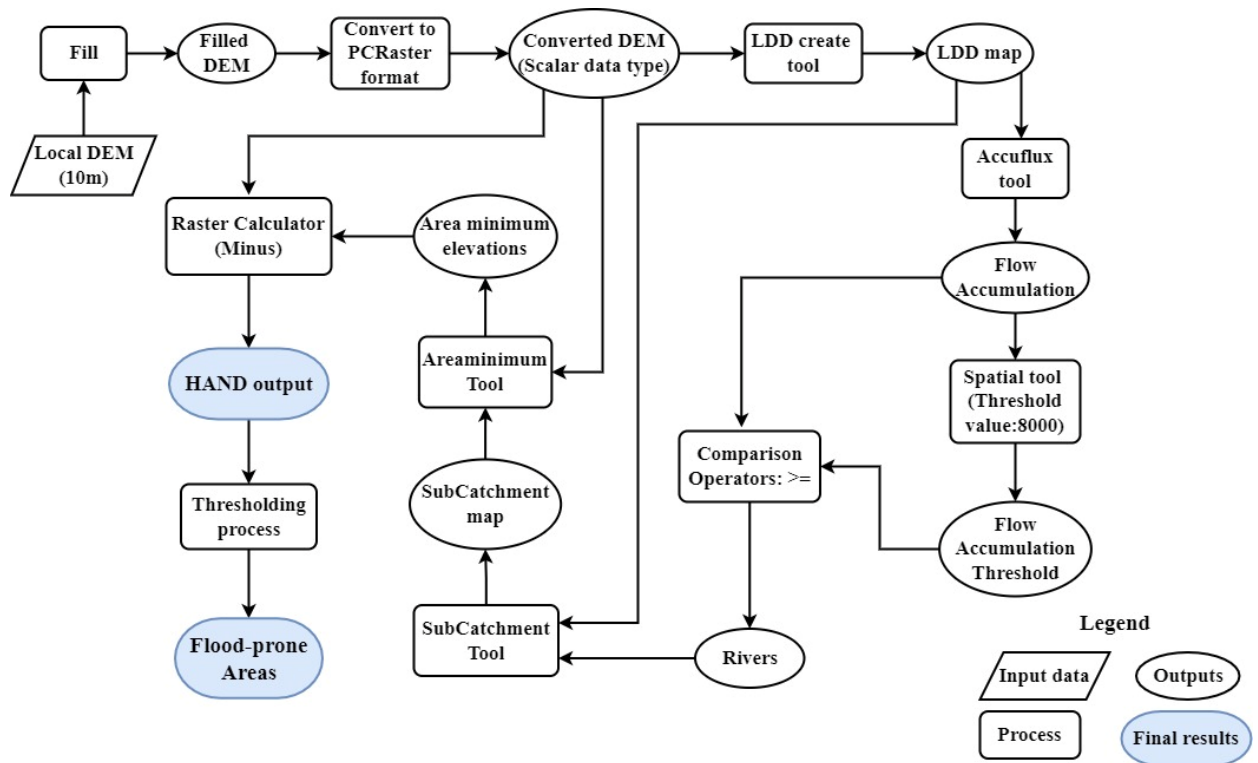
Figure 4-4 HAND model development processes using PCRaster Tool

PCRaster Tools plugin available in QGIS version 3.16.16 was used in this study to produce HAND output. The process follows the concept adopted by Rennó et al. (2008): firstly, correct the DEM by filling sinks, compute flow direction, and then define the drainage network in the study area. The PCRaster tool requires the conversation of DEM and other products into the scalar output data type. A threshold value is defined as a scalar data type to derive a drainage network. A conditional operation is established between flow accumulation or Local Drainage Direction (LDD) and threshold flow accumulation scalar data type. In this study, the drainage network was defined as pixels greater than or equal to 20000 because they represent the major stream network system of our interest in the model domain. As a result, a unique identifier (ID) was assigned to each pixel of the drainage network to determine the upstream area of each pixel of the drainage network. A minimum elevation is attributed to each area using filled DEM. Hence, the HAND output is calculated by subtracting the minimum height for each area from the corrected DEM using the raster calculator tool. Figure 4-4 shows details of HAND generation using the PCRaster tool.

The HAND output comprises different elevation zones; therefore, elevations below or equal to 3m, with reference to the nearest drainage elevation, were classified as regions susceptible to flood in this study because they are close to the drainage network. Planetscope-derived inundation extent that falls in the selected HAND zones were considered water features in the model domain. Water features that do not satisfy the condition were changed to non-water features using the Serval tool available in QGIS software.

## 4.4. Satellite Rainfall Estimates (SREs) evaluation

To deduce the differences between satellite-based and rain gauges-based rainfall estimates, the correlation coefficient (r), root mean square error (RMSE), and relative Bias (rBias) statistical metrics were selected for this study (Table 4-3). The correlation coefficient evaluates the linear relationship between gauge-based and satellite-based rainfall. The root mean square error (RMSE) computes the standard deviation of rainfall

errors measured from the satellite. Relative Bias (rBias) measures the difference between gauge-based and satellite-based rainfall where negative and positive values indicate underestimation and overestimation of satellite, respectively.

Additionally, the Mean Error (ME) was used to quantify the errors and their direction (overestimation or underestimation) of satellite products. The point-to-pixel method was executed to compare the rainfall of rain gauge stations with the corresponding pixel of each product from 2014 to 2018. Authors like Ageet et al. (2022); Bhatti et al. (2016) have applied the same approach.

Table 4-3 Statistical measurements of SREs

| Statistical measure | Value range | Accurate value & units |
|---|---|---|
| $r = \dfrac{\sum_{i=1}^{n}(S_i - \overline{S_i})(G_i - \overline{G_i})}{\sqrt{\sum_{i=1}^{n}(S_i - \overline{S_i})^2}\sqrt{\sum_{i=1}^{n}(G_i - \overline{G_i})^2}}$ | [-1 to 1] | 1, [-] |
| $RMSE = \sqrt[2]{\dfrac{\sum_{i=1}^{n}(S - G)^2}{N}}$ | [0 to +∞] | 0, [mm] |
| $rBias = \dfrac{\sum_{i=1}^{n}(S - G)}{\sum_{i=1}^{n} G} \times 100$ | [-∞ to +∞] | 0, [%] |
| $ME = \dfrac{\sum_{i=1}^{n}(S - G)}{N}$ | [-∞ to +∞] | 0, [mm] |

Where S and G represent satellite-based and gauge-based rainfall estimates, respectively, and N is the number of recordings.

The point-to-pixel approach facilitates the selection of satellite products that accurately represent the rainfall in the Sebeya catchment. The selected SREs will be aggregated on each sub-basin to produce rainfall inputs for the hydrological model. The Thiessen polygon approach was used to obtain the rainfall representation over sub-basins from InSitu measurements, which was used in the intercomparison with aggregated satellite rainfall.

## 4.5.    Satellite rainfall estimate bias-correction

Satellite-based rainfall estimates comprise errors, which could introduce uncertainties in their applications. Therefore, the errors need to be reduced to produce useful rainfall information. The time-space variable (TSV) approach, indicated by Habib et al. (2014), was selected for this study to correct for Bias because it is a direct and easy method that requires moderate data (Gumindoga et al., 2019). TSV method estimates the bias factor (BF) at a specific satellite grid and a corresponding rain gauge for a selected day (Equation 4-1). The BF is estimated within a predefined time window, which is then multiplied by daily satellite rainfall values. The BF can be calculated either using a moving window (MW) or a sequential window (SW). MW approach computes BF daily using the forward or backward window length specified, while SW estimates BF for all the days in the defined window length (Bhatti et al., 2016). The BF was computed when we had a certain minimum amount of accumulated rainfall and at least minimum days raining within a predefined window length; otherwise, no bias was estimated (i.e., assign a value of 1). Then, the performance evaluation, as stated above, will be conducted to compare the corrected SRE rainfall with the gauge-based rainfall.

$$BF_{TSV} = \frac{\sum_d^{t=d-l} G(i,t)}{\sum_d^{t=d-l} S(i,t)}$$

Equation 4-1

Where *G* and *S* represent gauge-based and satellite-based rainfall, respectively, *i* and *t* are rain gauge location and Julian day number, respectively, and *l* is the length of window time to compute the bias factor.

However, as described above, SREs possess systematic errors (hits, misses, and falses) that could be propagated during the bias correction process. Besides, ground-based rainfall may contain larger rainfall recordings (with over 50 mm/day) (see Figure 4-5) daily than satellite-based rainfall. Therefore, during the bias correction process, the user is required to establish an algorithm to reduce higher differences in rainfall recordings after bias correction. In this study, different conditions, including the reduction of differences between the highest rainfall on the rain gauge and satellite data, and differences between systematic errors, were developed after estimating BF. Figure 4-5 indicates an example scatter plot of satellite versus gauge-based rainfall for Nyundo station using TAMSAT satellite product, where the dots on the gauge-based axis show missed rainfall, and dots on the satellite-based axis describe false rain in the satellite product. The scattered dots on the graph represents the hits of rain. Generally, all those dots should be located on a black line (1:1 line) if satellite-based and gauge-based records are similar.
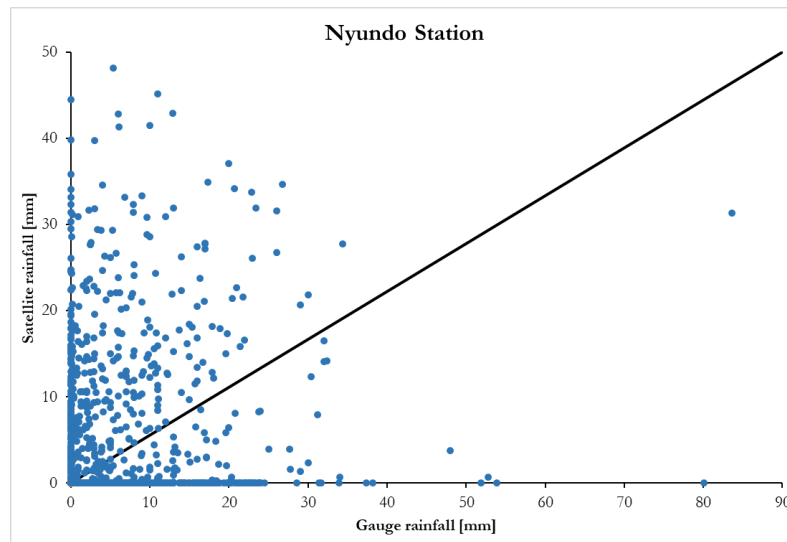


Figure 4-5 Scatter plot of satellite and gauge-based rainfall for Nyundo Station. The black line symbolizes the 1:1 line

Further investigation was performed to assess the effect of the adopted bias correction algorithm on reducing the errors in SREs. A sample of days during the rainy season (March-April-May) was selected to identify the results of the SW approach for CHIRPS and MW for TAMSAT products at 5 days window size at the Nyundo station. Table 4-4 describes the output of the bias-correction scheme in five days sampling window for each product. Recap that the BF for 5 days window size is computed when we have a minimum amount of 3 mm accumulated rainfall and a minimum of three days of rain within a 5 days window length; otherwise, no bias is estimated (i.e., assign a value of 1). Equation 4-2 and Equation 4-3 show the calculations for day number 107 using the SW approach for the CHIRPS satellite product and day number 114 using MW for TAMSAT, respectively.

$$BF_{107\_SW}^{CHIRPS} = \frac{19.8 + 2.5 + 0.3 + 3.8 + 0.0}{3.6 + 7.4 + 7.4 + 3.7 + 7.4} = 1.7$$

Equation 4-2

$$BF_{114\_MW}^{TAMSAT} = \frac{0.8 + 0.5 + 11.1 + 14.1 + 8.1}{0.0 + 0.0 + 0.0 + 0.0 + 0.0} = 1 \qquad \text{Equation 4-3}$$

Table 4-4 indicates a value of 1 on the bias factor on the TAMSAT satellite product for day 114. It was produced because within 5 days sampling window, TAMSAT SRE did not detect rainfall during the rainy season on the Nyundo station. Therefore, the weak rainfall detection capability of the TAMSAT product deteriorates its rainfall recordings that could be reproduced even after bias correction during the rainy season for the Nyundo station and other stations in the Sebeya catchment. The defects in the TAMSAT will be further investigated in the results section on the sub-basin scale. Therefore, this weakness propagated during bias-correcting the TAMSAT data (Table 4-4).

Table 4-4 BF estimation using 5 days sampling window size for different SREs

| Day number | InSitu Rainfall | Uncorrected CHIRPS | Bias Factor | Corrected CHIRPS | Uncorrected TAMSAT | Bias Factor | Corrected TAMSAT |
|---|---|---|---|---|---|---|---|
| 105 | 19.8 | 3.6 |  | 4.0 | 17.4 | 1.8 | 31.8 |
| 106 | 2.5 | 7.4 |  | 6.6 | 0.0 | 1.8 | 0.0 |
| 107 | 0.3 | 7.4 | 1.7 | 6.6 | 15.3 | 0.7 | 10.4 |
| 108 | 3.8 | 3.7 |  | 4.1 | 0.0 | 1.2 | 0.0 |
| 109 | 0.0 | 7.4 |  | 6.6 | 16.0 | 0.5 | 8.7 |
| 110 | 0.8 | 0.0 |  | 0.0 | 0.0 | 0.2 | 0.0 |
| 111 | 0.5 | 8.4 |  | 4.1 | 0.0 | 0.2 | 0.0 |
| 112 | 11.1 | 0.0 | 0.9 | 0.0 | 0.0 | 1.0 | 0.0 |
| 113 | 14.1 | 8.4 |  | 17.3 | 0.0 | 1.7 | 0.0 |
| 114 | 8.1 | 0.0 |  | 0.0 | 0.0 | 1.0 | 0.0 |

Table 4-4 presents the errors mentioned above that typically propagate in the corrected satellite rainfall. The yellowish color indicates the hit errors between InSitu and CHIRPS product rainfall recordings, but TAMSAT missed that rainfall. Different conditions developed after estimating BF to correct satellite rainfall recordings to reduce the difference between ground-based and satellite-based rainfall (as shown in Table 4-4 for the CHIRPS product) were performing reasonably. However, the artifacts detected in the TAMSAT satellite product propagated even after the bias correction process. Consequently, the applied algorithm in the bias correction improves the satellite rainfall recordings, but the bias-corrected satellite rainfall recordings are not always satisfactory because of deficiencies observed in SREs.

### 4.5.1. Definition of time window length

The window length needs to be defined adequately, representing bias in rainfall and allowing for effective bias correction to serve dynamic rainfall-runoff model simulation in this study. Authors like Habib et al. (2014) used a 7 days window length, and Gumindoga et al. (2016) applied a 10 days window length. However, Bhatti et al. (2016) evaluated different window length sizes (3, 5, 7, 9,..., 31) on both MW and SW techniques. They deduced that the 7 days SW approach adequately reduces errors in the CMORPH product for Gilgel Abbey catchment and the effectiveness of the applied bias-correction approach, which hydrologists can use to assess the application of CMORPH satellite data in the rainfall-runoff modeling. A similar process was followed in the Sebeya study area as no previous research was reported. Therefore, 3, 5, 6, 7, 10, 12, 15, 17, and 20 sample windows were selected to determine the effective window length that could perform well in the bias correction for the Sebeya catchment. A minimum of 3 days window length

was chosen to sufficiently accumulate rainfall on a temporal scale (Bhatti et al., 2016). The optimum window length will be the window length on which the RMSE doesn't show considerable changes with increasing window length.

## 4.6. Hydrological model

The HBV-light hydrological model was used to simulate the daily runoff of the Sebeya catchment. Bergstrom S (1976) developed HBV hydrological model at Swedish Meteorological and Hydrological Institute (SMHI) in the 1970s. HBV model can be classified as either lumped or semi-distributed model. The semi-distributed model approach will be applied in this study, where the Sebeya catchment was divided into sub-basins, elevation zones, and vegetation zones. Estimating runoff on a daily timestep of HBV requires daily rainfall, air temperature, and streamflow data. Evapotranspiration data, either daily or monthly averages, are also needed by HBV (Machlica et al., 2012).

Table 4-5 HBV light input data files (source:(Seibert, 2005))

| Data files | Description |
|---|---|
| **PTQ-file** | .txt file containing daily precipitation, temperature, and observed streamflow. |
| **Evaporation file** | .txt file of potential evapotranspiration, either daily or monthly averages. |
| **Sub Catchment file** | .txt file with several sub-catchments to run HBV. This study will use five sub-basins. |

### 4.6.1. Description of HBV model

Detailed information on the HBV model is further described in the document developed by Bergström (1992). The model can have four main components: snow routine, soil routine, response (groundwater) function, and river routing routine (Figure 4-6) (Heidler and Lisa, 2015). Since the study area doesn't receive snow, this component is removed. HBV model solves the water balance equation (Equation 4-4) that regulates the flow from the land surface to the deepest lower zone reservoir (Figure 4-6).

$$P - E - Q = \frac{d}{dt}(SM + UZ + LZ + LAKES)$$

Equation 4-4

Where P is rainfall, E is evapotranspiration, Q is runoff, SM is soil moisture content, UZ and LZ are upper zone and lower zone storages, respectively, and LAKES is the water storage in the basin.
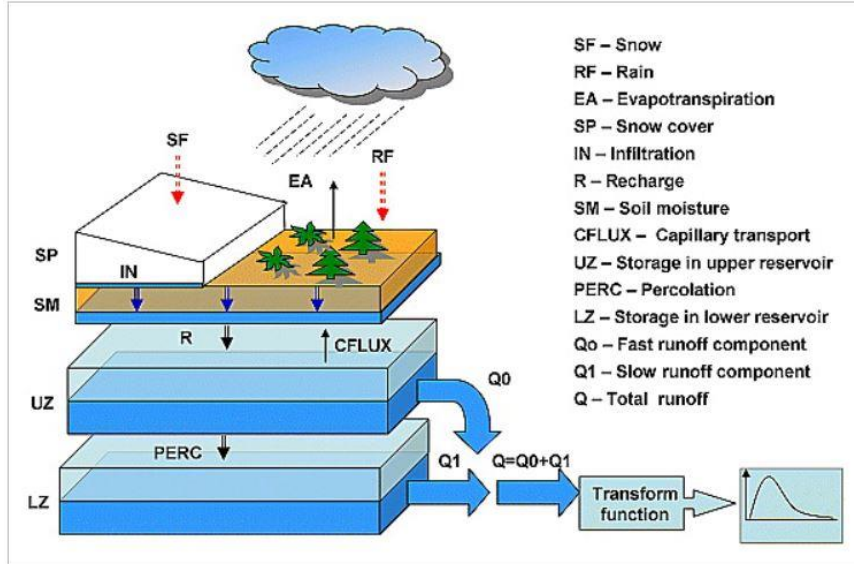
Figure 4-6 General description of the HBV-light model (source: (Solomatine and Shrestha, 2009))

Precipitation in the form of rainfall is the primary input in the soil moisture routine. Water stored in the soil governs actual evapotranspiration ($ET_a$), soil water content (SM), groundwater recharge ($Q_{in}$), and direct discharge ($Q_d$) in this routine based on the infiltrated precipitation. The soil routine requires three parameters: limit for potential evaporation (LP), field capacity (FC), and shape parameter (BETA), which is a power relationship between the response function and rise in soil moisture storage. Water that the soil moisture zone cannot hold is routed in response routine as recharge (R) (Mendez and Calvo-Valverde, 2016).

$$Q_d = max(P + SM - FC, 0)$$ 

Equation 4-5

$$Q_{in} = \left(\frac{SM}{FC}\right)^{BETA} \times (P - Q_d)$$ 

Equation 4-6

$$ET_a = ET_0 \times min\left[\frac{SM}{FC \times LP}, 1\right]$$ 

Equation 4-7

The response routine receives the water as recharge from the soil moisture zone, and it has two reservoirs, Upper zone (SUZ) and Lower Zone (LZ) storage. The SUZ reservoir describes the fast runoff component, and the LZ reservoir represents the slow or baseflow component. Three recession coefficients, $K_0$ and $K_1$ and $K_2$, and percolation rate (PERC) are the parameters used in the routine. Another parameter, alfa ($\alpha$), represents the nonlinearity of the SUZ reservoir and varies between 0 and 3. Capillary upward transport ($C_f$) is another process from the UZ storage to the soil moisture zone and depends on the difference between FC and available SM and the CFLUX parameter. The CFLUX parameter determines the amount of capillary flow (Mendez and Calvo-Valverde, 2016).

$$Q_0 = K_0 \times SUZ^{(1+\alpha)}$$ 

Equation 4-8

$$C_f = CFLUX \times \left(\frac{FC - SM}{FC}\right)$$ 

Equation 4-9

The baseflow is the second part of the response routine. The only input to the LZ reservoir is the PERC from the UZ, which depends on the recession coefficient, $K_2$.

$$Q_2 = K_2 \times LZ \qquad\qquad\qquad\qquad\qquad\qquad \text{Equation 4-10}$$

It is clearly observed that the actual evapotranspiration, groundwater recharge, and capillary flux depend on the amount of soil moisture storage. As the soil dries out, the actual evapotranspiration decreases.

The total outflow from all reservoirs is transformed into river runoff by a triangular weighting function with the parameter MAXBAS (Seibert and Vis, 2012). Like other hydrological models, the HBV model is calibrated with the streamflow recordings at the catchment outlet.

$$Q_t = Q_d + Q_0 + Q_2 \qquad\qquad\qquad\qquad\qquad\qquad \text{Equation 4-11}$$

### 4.6.2. HBV-light model set up

The HBV-light model was used in this research to simulate streamflow due to its simple structure, user-friendly approach, and application in different domains, including the estimation of flood cases (Seibert and Vis, 2012). The model requires meteorological forces, including rainfall, temperature, and potential evapotranspiration (see Table 4-5), as indicated in the HBV manual document developed by Seibert (2005). Figure 4-7 indicates the methodological framework of the hydrological model.
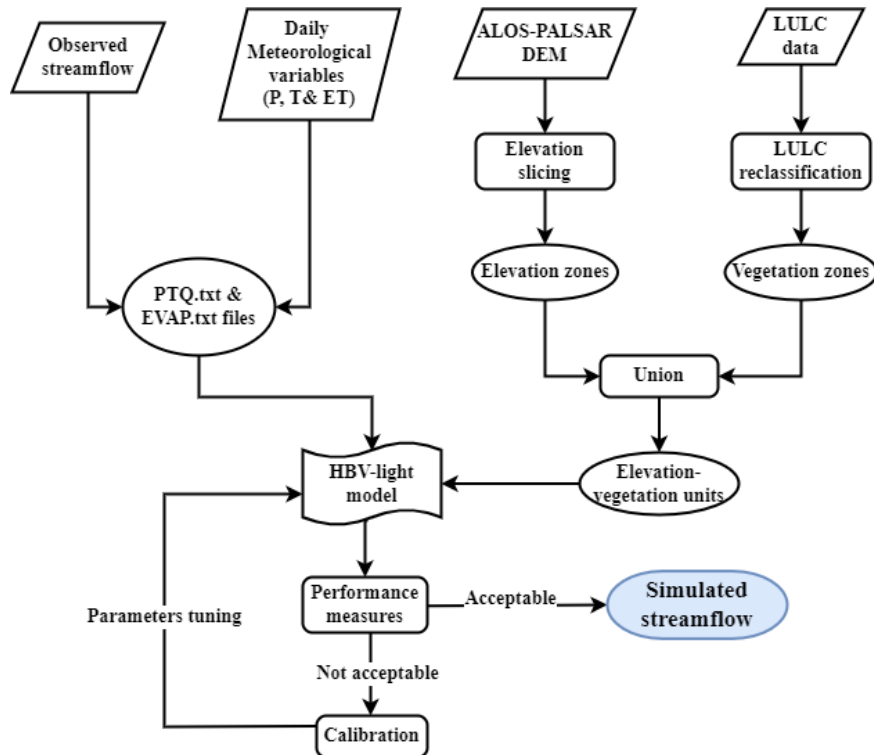


Figure 4-7 Methodological flowchart of HBV-light model

The available ALOS-PALSAR DEM of 12.5m × 12.5m spatial resolution was used to divide the Sebeya catchment into sub-catchments and create elevation zones. Five sub-catchments were delineated, and the elevation was classified into four elevation zones with 300m intervals. The elevation zones offer the HBV model the ability to consider the elevation aspect and distribution of meteorological variables in the study area with respect to topography (Assoumpta and Aja, 2021). The elevation slicing was performed using

QGIS software into four elevation zones (Figure 4-8a). The ALOS-PALSAR DEM was also used to create an aspect map that indicates different directions of slopes in the study area.
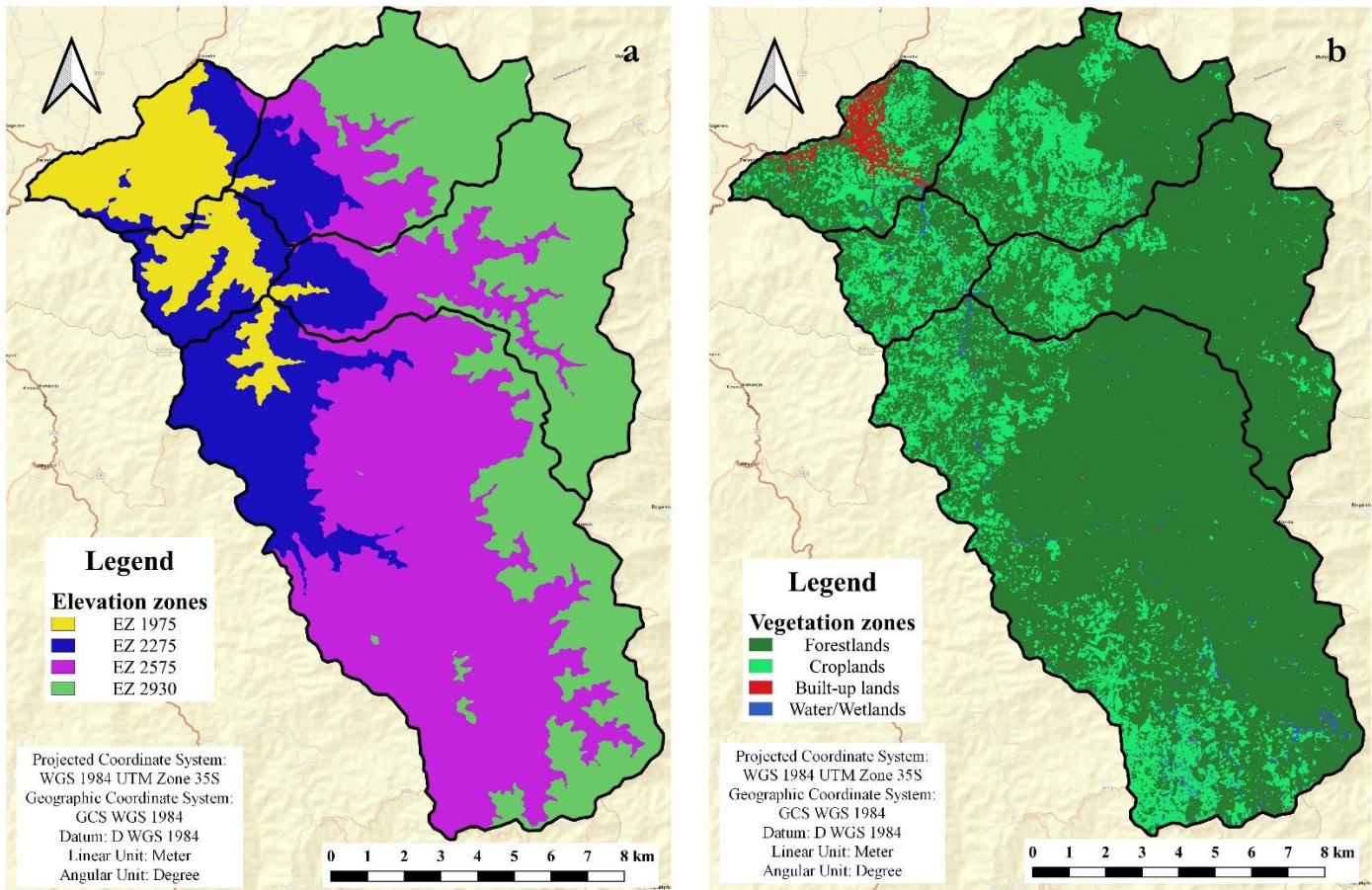


Figure 4-8 Elevation zones (a) and vegetation zones (b) of the Sebeya catchment for the HBV model

The WorldCover map produced by ESA based on Sentinel-1 and Sentinel-2 data was used in this study to create vegetation zones for the HBV model. QGIS software was used to reclassify seven LandCover classes into four vegetation zones to match HBV model input requirements (Figure 4-8). Afterward, the elevation zones map, aspect map, and vegetation zones map were combined in one map to find the vegetation zone ratio for each elevation zone and sub-basin.

### 4.6.3. HBV model calibration

The hydrological model requires a calibration process to produce a match between simulated and observed streamflow time series. Calibration is the process of adjusting model parameters, boundary conditions, and meteorological stresses, subject to the model approach, to obtain optimal model input and to produce reliable and accurate model simulations (Rientjes, 2016). In this study, model calibration only targeted model parameter optimization.

Many performance functions can be used to evaluate a hydrological model. This study will use two evaluation functions: the Nash-Sutcliffe coefficient of efficiency (NS) and the Relative Volume Error (RVE). RVE indicates the model's performance in the overall water balance, while NS shows the model's performance based on the simulated and observed hydrographs. Following the value range of NS and RVE objective functions, as described by Rientjes (2016), the NS objective function needs to be closer to 1 and RVE close to zero. Table 4-6 displays the mathematical equations of these criteria.

Table 4-6 Model Performance criteria (source: (Rientjes, 2016))

| Performance metrics | Formula | Values | Performance indication |
|---|---|---|---|
| **Nash-Sutcliffe coefficient of efficiency (NS)** | $NS = 1 - \dfrac{\sum_{n-1}^{N}(Q_{obs} - Q_{sim})^2}{\sum_{n-1}^{N}(Q_{obs} - \overline{Q_{obs}})^2}$ | 1 | Perfect |
| | | $0.9 - 1$ | Extremely well |
| | | $0.8 - 0.9$ | Very well |
| | | $0.6 - 0.8$ | Reasonably well |
| **Relative Volume Error (RVE)** | $RV_E = \left(\dfrac{\sum_{i=1}^{n}(Q_{sim(i)} - Q_{obs(i)})}{\sum_{i=1}^{n} Q_{obs(i)}}\right) \times 100$ | 0 | Best |
| | | -5% to +5% | Well |
| | | $\pm 5\%$ to $\pm 10\%$ | Reasonable |

Where $Q_{obs}$ and $Q_{sim}$ are observed and simulated streamflow, respectively, and the "trial and error" optimization technique was applied to fit the observed and simulated streamflow by adjusting the model parameters based on the studies that used the HBV model to simulate the catchment's streamflow (Habib et al., 2014; Solomatine and Shrestha, 2009; Ymeti, 2007). Sensitive parameters are optimized, keeping other parameters fixed until optimal model parameter values are reached.

## 4.7. Hydrodynamic flood modeling

The HEC-RAS software package developed by the United States Army Corps of Engineers was selected for this research, which is a computer program simulating the hydrodynamic behavior of water in rivers and floodplains. HEC-RAS is free software with a user-friendly interface, with a GIS component (RAS Mapper) to display the imported geometric data, other input data, and simulation outputs. The software can model 1D steady or unsteady water flow, 2D unsteady water flow, sediment transport computations, water quality analysis, and hydraulic structures design (Lea et al., 2019). Among those applications, this research will focus on the 2D unsteady HEC-RAS model scheme to simulate the flood extent in the river and floodplains, as there were no river cross-section data to integrate the 1D model approach. Several studies revealed the capacity and efficient performance of the HEC-RAS tool to adequately represent flood paths in rivers and floodplains (Boukhaly Traore et al., 2015; Lea et al., 2019; Rangari et al., 2019). Therefore, the 2D hydrodynamic model scheme was developed in the HEC-RAS 6.1.0 version for the Sebeya flood domain.

### 4.7.1. 2D HEC-RAS model governing equations

The 2D HEC-RAS model approach applies either Diffusion Wave equations (DWE) or Shallow Water equations (SWE) to simulate water flow in the channel river and floodplain. The original SWE, also known as Saint-Venant equations, was used in this study and comprises mass (continuity) (Equation 4-12) and momentum conservation equations (Equation 4-13 and Equation 4-14).

The 2D flow continuity equation (USACE, 2021)

$$\frac{\partial h}{\partial t} + \frac{\partial(hu)}{\partial x} + \frac{\partial(hv)}{\partial y} = q \qquad\qquad \text{Equation 4-12}$$

Where $u$ and $v$ are velocity in x and y direction [L/T], respectively, $t$ is the time [T], $h$ is the water depth [L], and $q$ is the source or sink flux [-].

The 2D flow momentum equation

$$\frac{\partial u}{\partial t} + u\frac{\partial u}{\partial x} + v\frac{\partial u}{\partial y} - f_c v = -g\frac{\partial z_s}{\partial x} + \frac{1}{h}\frac{\partial}{\partial x}\left(v_{t,xx}h\frac{\partial u}{\partial x}\right) + \frac{1}{h}\frac{\partial}{\partial y}\left(v_{t,yy}h\frac{\partial u}{\partial y}\right) - \frac{\tau_{b,x}}{\rho R} + \frac{\tau_{s,x}}{\rho h} \quad \text{Equation 4-13}$$

$$\frac{\partial u}{\partial t} + u\frac{\partial v}{\partial x} + v\frac{\partial v}{\partial y} - f_c u = -g\frac{\partial z_s}{\partial y} + \frac{1}{h}\frac{\partial}{\partial x}\left(v_{t,xx}h\frac{\partial v}{\partial x}\right) + \frac{1}{h}\frac{\partial}{\partial y}\left(v_{t,yy}h\frac{\partial v}{\partial y}\right) - \frac{\tau_{b,y}}{\rho R} + \frac{\tau_{s,y}}{\rho h} \quad \text{Equation 4-14}$$

Where $u$ and $v$ are velocity in x and y direction [L/T], $g$ is gravitational acceleration [L/T$^2$], $z_s$ is water surface elevation [L], $v_{t,xx}$ and $v_{t,yy}$ are horizontal eddy viscosity coefficients in the x and y orientations [L/T], $\tau_{b,x}$ and $\tau_{b,y}$ are bottom shear stresses on the x and y directions [M/L/T$^2$], $R$ is the hydraulic radius [L], $\tau_{s,x}$ and $\tau_{s,y}$ are the surface wind stresses in the x and y directions [M/L/T$^2$], $h$ is the water depth [L] and $f_c$ is the Coriolis parameter [-].

The terms in the 2D momentum equation describe the acceleration terms on the left-hand side of the equation and internal or external forces acting on the fluid (water) on the right-hand side of the equation.

### 4.7.2.    HEC-RAS model development

The 2D HEC-RAS model approach was applied in this research to determine the flood characteristics (depth, velocity, etc.) for the Sebeya floodplain. The model involves the creation of floodplain polygon, topographic representation (DTM data), surface roughness, and boundary conditions. The input data pre-processing was the first step in constructing the 2D HEC-RAS model, where the DTM was firstly enhanced before being used in the model. The first input in the HEC-RAS model is the DTM for topographic representation using the RAS Mapper user interface. Afterward, the GIS component, RAS Mapper, was used to create a floodplain polygon in which the computational mesh would be generated (Brunner, 2021). Figure 4-9 describes the components of the 2D HEC-RAS model.
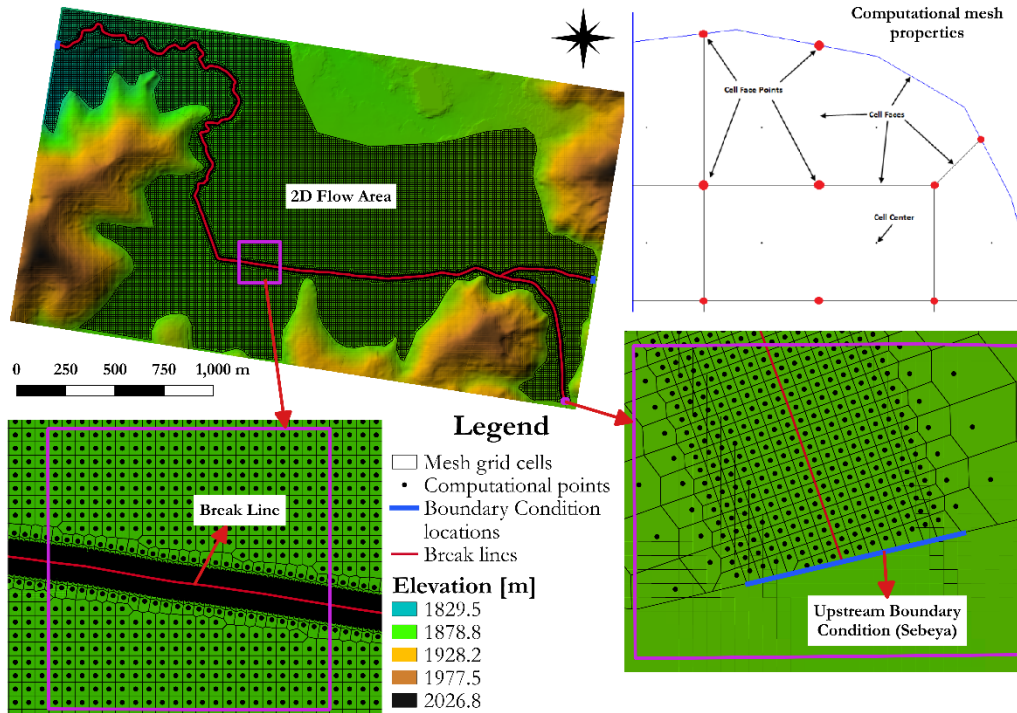


Figure 4-9 2D HEC-RAS schematization of Sebeya model domain

The 2D HEC-RAS model allows the creation of a 2D flow area, considered as a floodplain in the model. After delineation of the 2D flow area, a computational mesh was produced. The HEC-RAS user defines the mesh cell size, and 10m × 10m spacing was used to create the mesh in this study (Figure 4-9). Every computational mesh possesses three main properties called cell center, which is a computational cell center where water surface elevation is estimated for each cell, cell faces that represent the boundary surfaces of each cell, and cell face points describing the borders of the cell faces, that can be used to connect 2D flow areas to 1D components, and boundary conditions (Brunner, 2021a). However, in narrow locations, like river channels, the mesh was refined to allow a better flow simulation in the river channel. Therefore, the cell size spacing was reduced up to 1m × 1m in the river, as shown in Figure 4-9. Break lines were used to force the mesh at a small grid size and were interpolated in the river to control flow direction within the channel. The break lines can be imported as shapefiles or delineated by hand in the RAS Mapper interface. Figure 4-9 shows an example of break lines in the 2D flow area along the river channel.

The model was developed using the original DTM and enhanced DTM-2 to assess the effect of DTM errors in the flood modeling. After creating both original and enhanced terrain models and delineating mesh grid cells, the land cover layer was added to the model to define the surface roughness coefficient. Streamflow from the hydrological model was depicted on the boundary conditions, as described in the following sections. Therefore, each terrain model is associated with its corresponding geometry file and land cover layer within the 2D HEC-RAS model.

### 4.7.2.1. Boundary conditions

The 2D HEC-RAS flood model requires flow boundary conditions, upstream and downstream, to simulate flood flow bounded in time and space. Boundary conditions have significant effects on the flood simulation results, and the 2D unsteady flow simulation was used to estimate flood flow conditions in the Sebeya model domain. The model allows the application of different boundary conditions, which include the Flow Hydrograph, Stage Hydrographs, Rating Curves, and Normal Depth. The flow and stage hydrographs can be applied at points where water enters or leaves the 2D flow area, i.e., at upstream or downstream boundary conditions, while the normal depth and rating curve are used where water is discharged out of the model domain (downstream boundary condition) (Brunner, 2021a). Timeseries data of flow or stage (water level), for flow and stage hydrograph, respectively, are defined where they can be entered manually into a table or using an HEC-DSS[9] file (Brunner, 2021b). The rating curve in the HEC-RAS model is determined by the relation between surface water elevation and the flow, which is entered in the table manually or using the HEC-DSS file. The normal depth is entered in the model as a friction slope of the river's reach (Brunner, 2021a). The HE-RAS user can localize one boundary condition in one or more locations that are associated with a 2D flow area. Hence, flow Hydrograph boundary condition was used on the upstream inflows (Sebeya and Karambo) and the Normal Depth boundary condition in the downstream outflow of the flood model domain (Figure 4-10). Upstream inflows are obtained from rainfall-runoff model simulations for the 2018 flood event. A friction slope was defined at the downstream boundary condition for the floodplain to convey flow out of the 2D model domain.

---

[9] Hydrologic Engineering Center - Data Storage System
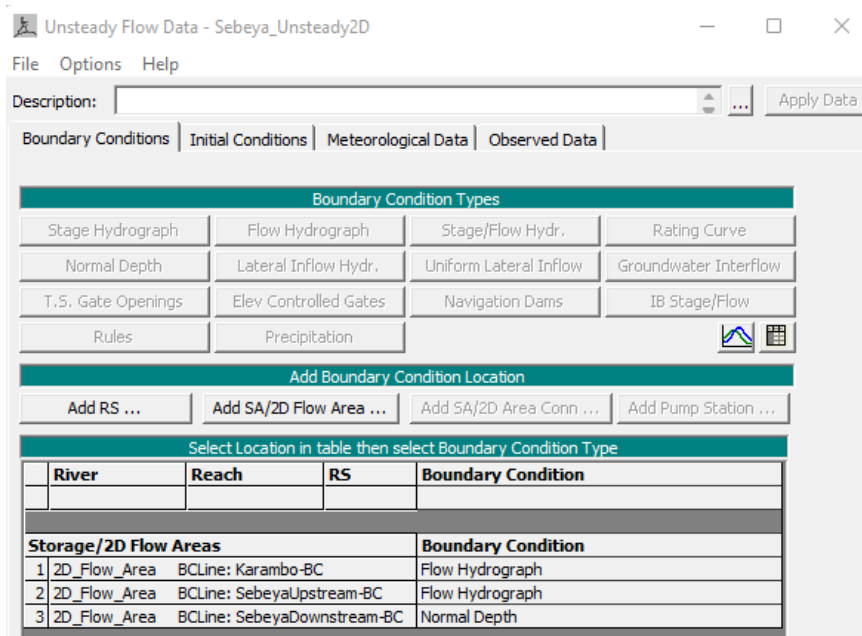
Figure 4-10 Boundary conditions used for the Sebeya 2D flood model

#### 4.7.2.2. Land cover representation

Manning's coefficient (n) describes the flood flow resistance of the river channel and floodplain. The land cover map obtained using the available orthophotos was used to parameterize the roughness coefficient in the flood model. The definition of surface roughness values will be based on the literature. The classified land cover map was resampled to the DTM's spatial resolution. The RAS Mapper user interface allows the creation of a land cover layer, which is used to define manning's values for each land cover class. Figure 4-11 shows land cover classes imported in the flood model, and Table 4-7 describes the manning's roughness coefficient values used for each land cover class.

Table 4-7 Land cover characteristics adapted from Brunner (2021)

| Land cover classes | Manning's values (n) |
|---|---|
| Urban areas | 0.08 - 0.16 |
| Green areas | 0.06 - 0.12 |
| Roads | 0.03 - 0.04 |
| River channel | 0.025 - 0.05 |
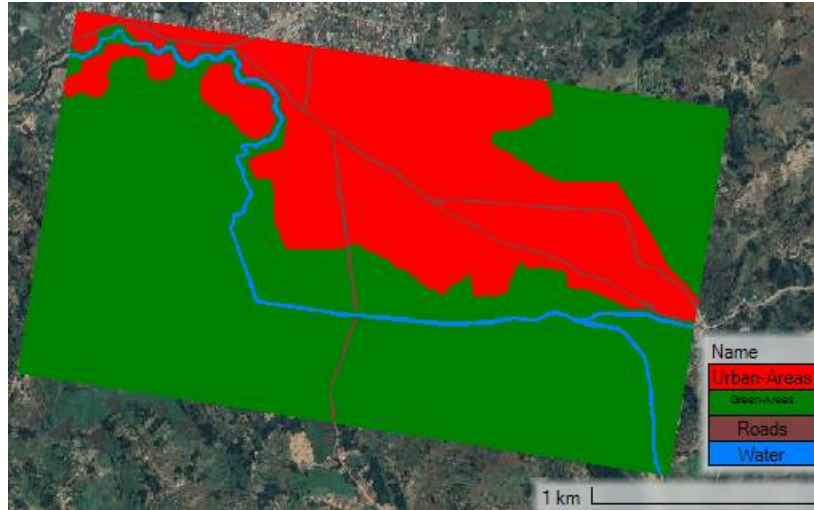
Figure 4-11 Land Cover representation in RAS Mapper

### 4.7.3.    Comparison of model flood extent and satellite-based inundation extent

The flood model is calibrated by comparing the simulated and satellite-derived flood extent. The calibration is made by adjusting the surface roughness coefficient of different land use in the model domain until an acceptable match between observed and simulated flood extent. The simulated flood extent was compared with the satellite-derived water extent because there were no observed flood recordings (flood depth or flood extent) to perform the hydrodynamic model calibration of the Sebeya catchment.

Table 4-8 Contingency table (Schumann et al., 2009)

|  | Wet area in satellite observations | Dry area in satellite observations |
|---|---|---|
| **Wet area in the flood model** | A | B |
| **Dry area in the flood model** | C | D |

The performance of the flood model is assessed using the goodness of fit measures. The contingency table (Table 4-8) compares dry and wet pixel numbers in the simulated and observed flood extent (Grimaldi et al., 2016; Schumann et al., 2009). Table 4-9 shows the selected statistical measure of the flood model based on the contingency table. The critical success index (CSI) was selected because of its wide applications (Addae, 2018; Grimaldi et al., 2016; Hunter et al., 2005). The CSI evaluates the ratio of satellite-derived water surface and/or accurately simulated flood extent pixels (Hunter, 2005). A minimum value of the CSI is zero, indicating that there was no simulated flood extent compared to satellite-derived inundation water, while a maximum value of CSI (1) represents a perfect match between the simulated and satellite-observed flood extent (Hunter et al., 2005).

Table 4-9 Flood extent performance measures by Grimaldi et al. (2016) and Schumann et al.( 2009)

| Measure | Equation | Description | Range |
|---|---|---|---|
| **Critical success index (CSI)** | $\dfrac{A}{A + B + C}$ | Measures the wet/dry pixels precisely simulated by the model | $0 - 1$ |

# 5. RESULTS AND DISCUSSION

## 5.1. DTM processing

### 5.1.1. DEM enhancement

Flood model simulations are affected by the representation of topographic and elevation terrain used in the model, where the coarse-resolution and poor grid data tend to result in overestimating inundation extent. Therefore, the 10m × 10m spatial resolution DEM was resampled and enhanced based on the knowledge and the available 0.25m × 0.25m grid size orthophotos for the model domain to produce an appropriate terrain for the flood model. Figure 5-1 represents original and enhanced DEM at 1m × 1m spatial resolution using the second approach to illustrate refinement results. The red ellipses indicate the change in elevations and enhancement on the DEM in floodplains of the model domain. It can be observed that the surface was smoothed, and the river network is well perceived after DEM enhancement.
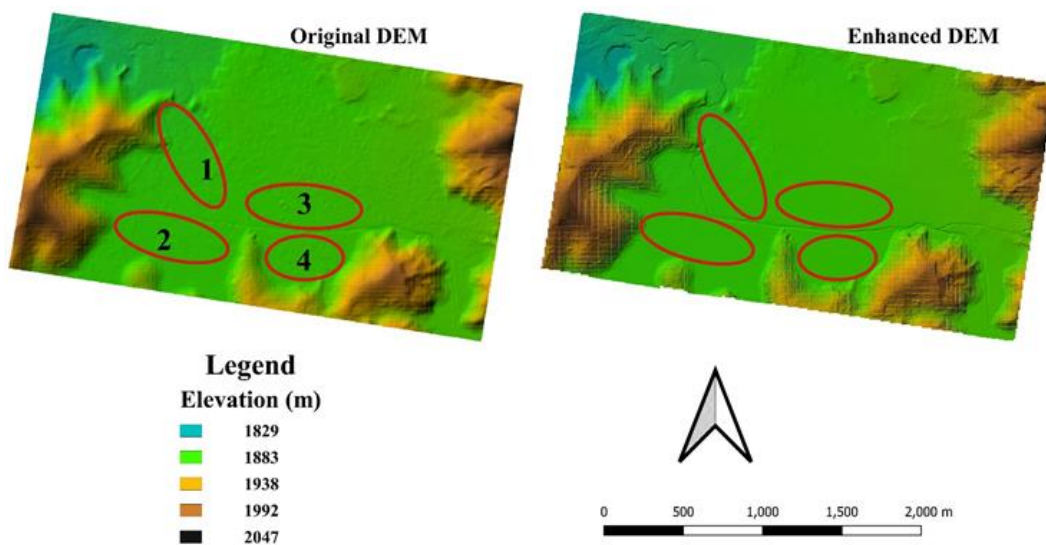


Figure 5-1 Topography of original and enhanced DEM at 1m spatial resolution

The output of modified terrain was resampled into elevation grid resolutions of 5m and 10m using the bilinear interpolation method in QGIS software (Figure 5-2). The output images significantly differ in representing the real-world elevation in floodplain areas. Figure 5-2 clearly describes that 5m and 10m resolutions fail to represent the river system in the model domain after DEM enhancement and interpolation on the selected floodplain '4' (Figure 5-1). On the other hand, 1m × 1m resolution represents the details of surface features (channels) in the floodplain. Therefore, 1m × 1m spatial resolution will be used for flood modeling.
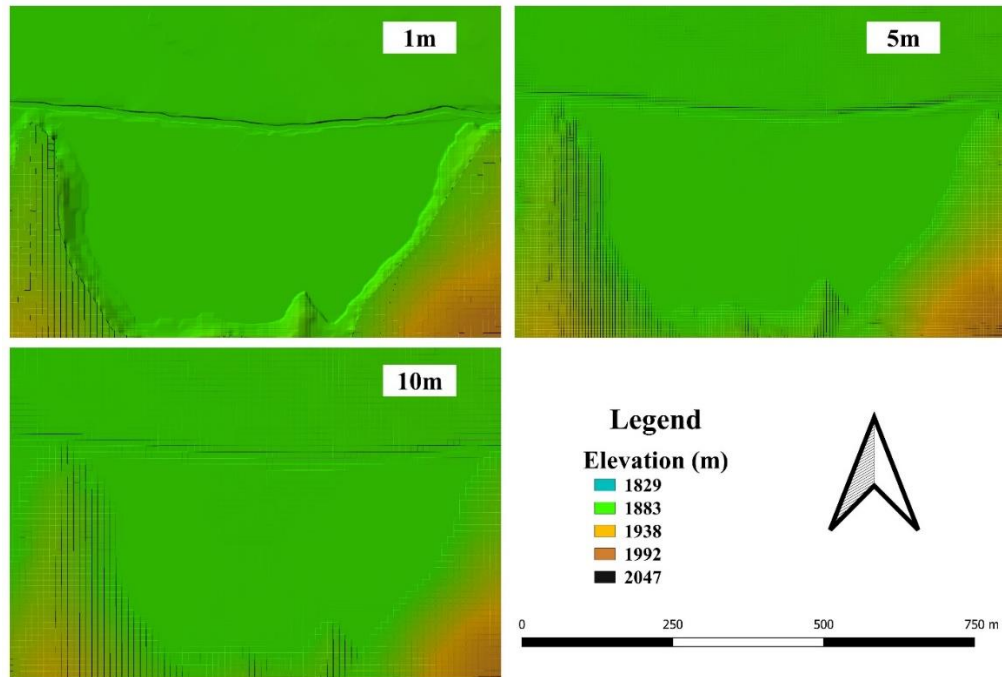
Figure 5-2 Enhanced terrain representation at different resolutions

### 5.1.2. Comparison of available DEMs

The basic intercomparison of the original DEM and the other two enhanced DEMs, generated from different approaches as mentioned in section 4.1, was performed in this study. All the DEMs showed nearly similar statistical measurements in elevations for the model domain. Table 5-1 describes the statistical measures of the DEMs.

Table 5-1 Statistical analysis of the DEMs

| DEM type | Minimum [m] | Maximum [m] | Mean [m] | Standard Deviation (SD) |
|---|---|---|---|---|
| **Original DEM** | 1829.0 | 2047.2 | 1899.8 | 33.78 |
| **Enhanced DEM-1** | 1829.0 | 2047.2 | 1899.8 | 33.77 |
| **Enhanced DEM-2** | 1829.5 | 2047.0 | 1899.9 | 33.69 |

This research did not perform the vertical accuracy assessment due to the lack of ground control points (GCPs). As a result, a small area in the floodplain was selected to explain the visible differences in the available DEMs. Figure 5-3 shows the difference in elevation gradient in the selected small area in the floodplain. It can be seen that the original DEM and the enhanced DEM using the first approach show almost the same gradient in the elevation within the selected area in the floodplain. Still, the DEM from the second approach presents the difference in elevation gradient within the interested area. The enhanced DEM-2 has a continuous elevation gradient in this small area, which could be the same for the whole floodplain.
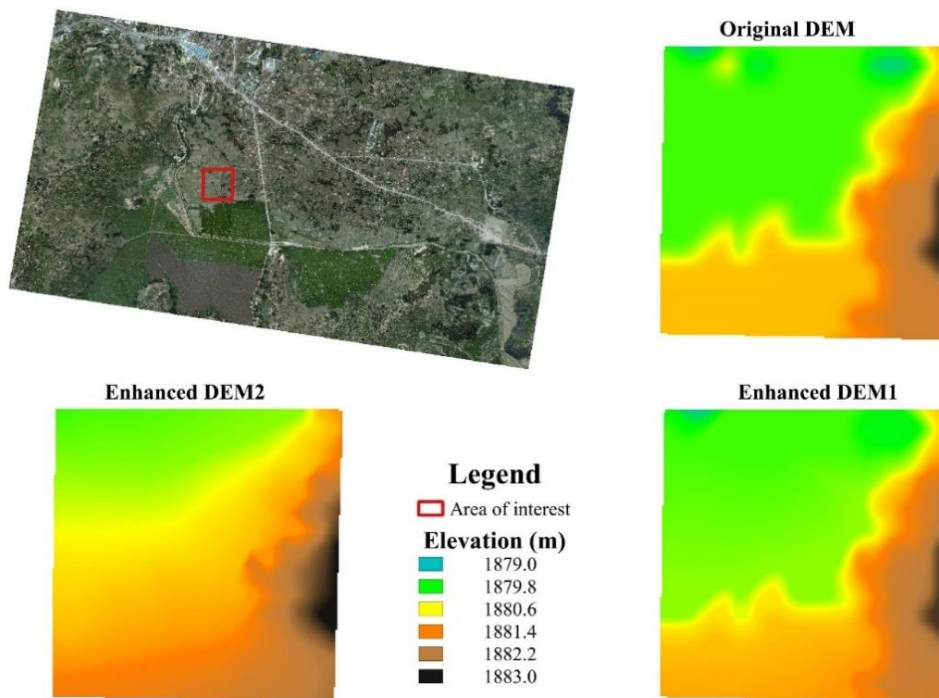
Figure 5-3 The difference in elevation gradient of a selected area for DEM comparison in the floodplain

Besides the fundamental statistical analysis and elevation gradient visual comparison of the DEMs, a horizontal profile was created in the floodplain using the Terrain profile tool in QGIS. Figure 5-4 shows the location of the profile line in the floodplain and its longitudinal gradient from the upstream side. According to the results, the improved DEM-2 has a continuous change in slope. The other two DEMs of the original and enhanced DEM-1 show some flat parts and indentations in the created profile. Therefore, the second approach applied to enhance the DEM could produce a valuable and reliable topography for the flood model in data-limited areas, like the Sebeya domain area.
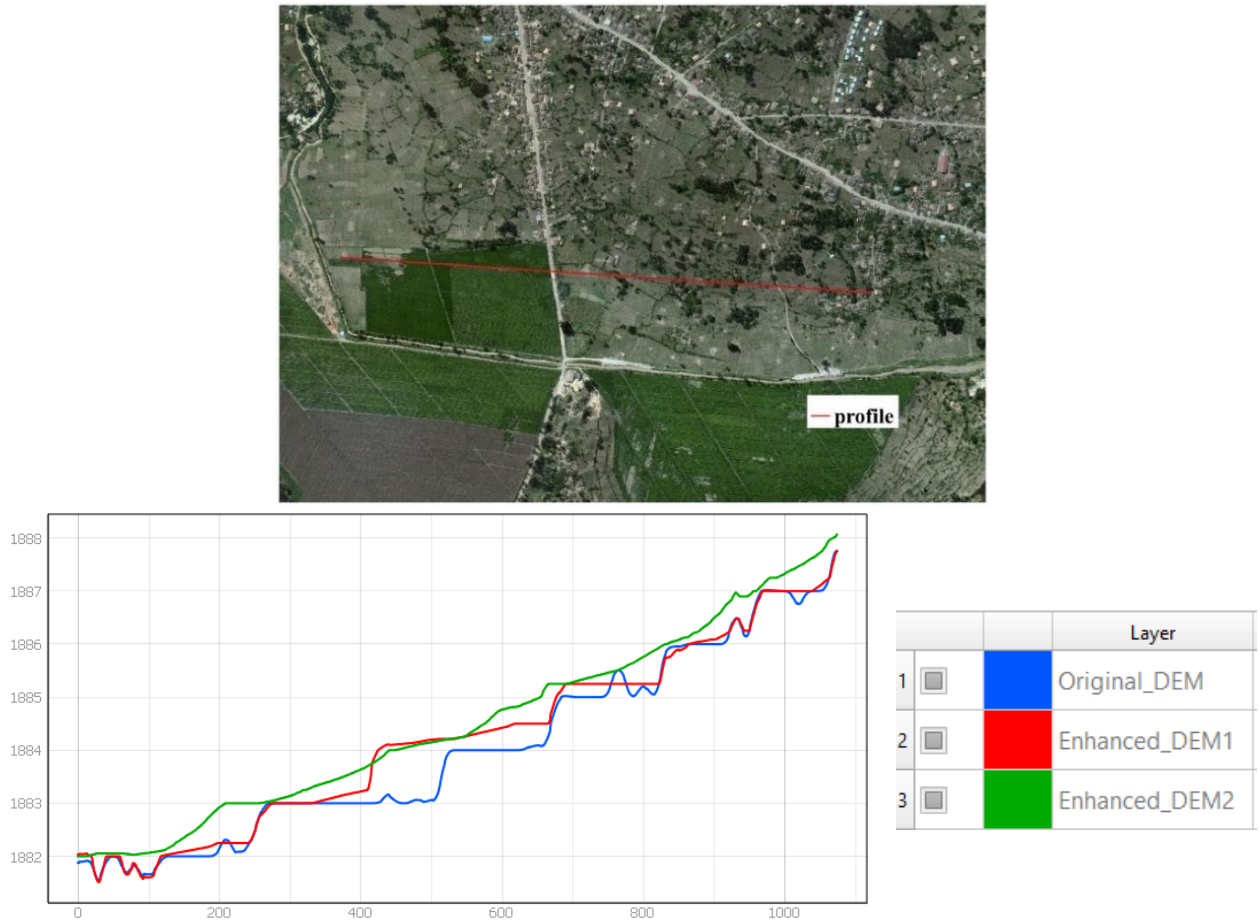
Figure 5-4 Horizontal profile characteristics for DEMs comparison

The difference maps were prepared where more analysis was performed on the floodplain's selected polygon. The original DEM was subtracted from enhanced DEM-2, as shown in Figure 5-5. It can be seen that the error depicts vertical differences up to 1m in areas where smoothing the terrain and channel delineation were executed. The difference map also shows irregular changes in elevation due to the smoothing process applied to the original DEM to enhance its vertical resolution. These lines follow the contours that were created, as explained in section 4.1, to improve the available DEM. Afterward, the hydro-DEM processing was performed on the enhanced DEM to fill the pits and sinks in the DEM-2 product. The difference map was produced for this case, where the enhanced DEM-2 was subtracted from the filled DEM (Figure 5-5). It can be revealed that the errors have been minimized where the majority of differences are below half a meter (0.5m) in vertical directions. The description of statistics of elevation differences is detailed in Table 5-2.

Table 5-2 Detailed statistics of elevation difference maps of the floodplain

| DEM type | Minimum [m] | Maximum [m] | Mean [m] | Standard Deviation (SD) |
|---|---|---|---|---|
| **Enhanced DEM-2 - Original DEM** | -4.77 | 2.03 | 0.29 | 0.47 |
| **Filled DEM - Enhanced DEM-2** | 0 | 2.91 | 0.03 | 0.08 |
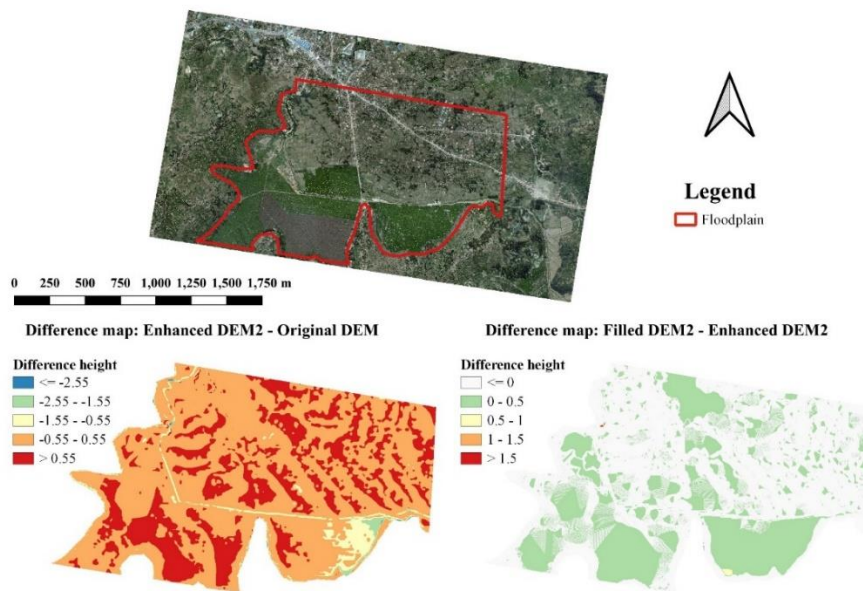
Figure 5-5 Elevation difference maps for the floodplain

## 5.2.    Planetscope satellite-derived surface water extent

Figure 5-6 represents the NDVI map of the Planetscope images before and after the flood event. The NDVI values range from 0.02 to 0.8 and from -0.04 to 0.83 for the 23/09/2017 (5 months before flooding) and 04/03/2018 (14 hours after the flood) images, respectively. The low positive NDVI values in both images (before and after) represent built-up areas and water bodies (Table 5-3). Table 5-3 indicates high NDVI positive values for vegetation cover in the image before flooding, while on the image after flooding, low NDVI positive values on the same pixels show change from vegetation to water or mud, which indicates the effects of flooding. The residual difference image shows negative values for built-up areas and low to high positive values for areas affected by flooding (Figure 5-6). The reddish color on the residual difference image indicates areas with decreased NDVI that marks the affected regions by flooding. Therefore, a pixel-by-pixel evaluation was performed to examine NDVI values of water bodies, buildings, and affected areas in the three images, i.e., before and after the flood and residual image (Table 5-3). This evaluation facilitated the selection of the threshold value to delineate surface water features in the Planetscope image.
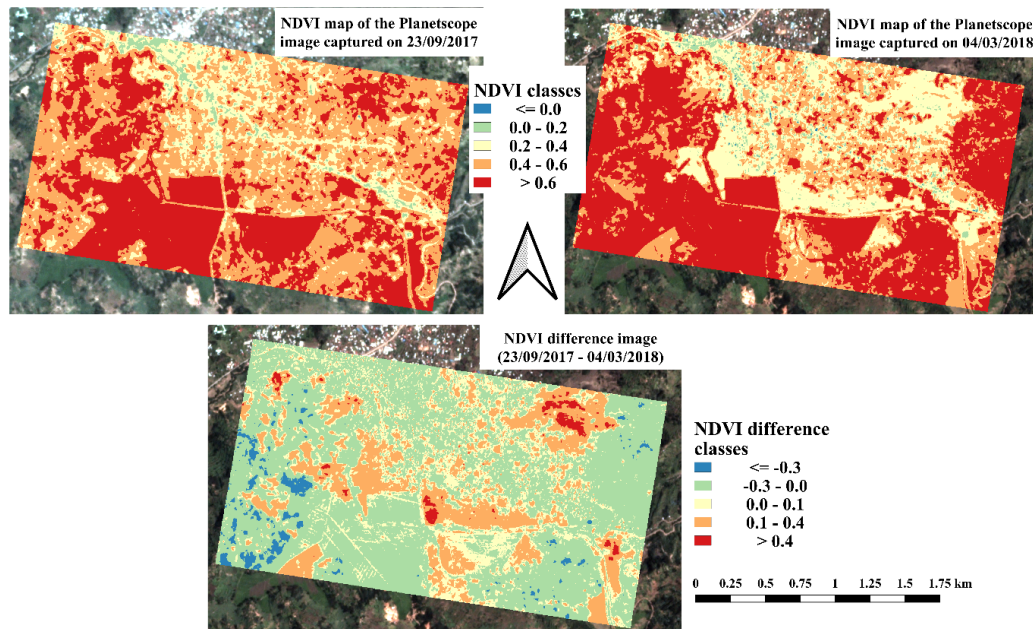
Figure 5-6 NDVI map of Planetscope and residual difference images for model domain

Table 5-3 shows the image's NDVI and different residual values of water bodies, built-up areas, and affected areas. All selected pixels under analysis were cloud-free in the images. The change detection approach was conducted to deduce the regions affected by the flood in the 2018 image. The no-change pixels show zero value on the map. In contrast, negative and high positive values represent an increase in vegetation and a decrease or removal of vegetation by water and mud during flooding, respectively.

Table 5-3 Pixel-by-pixel NDVI values evaluation of the Planetscope images

| NDVI Map | Water bodies | | | Built-up areas | | | Affected areas | | |
|---|---|---|---|---|---|---|---|---|---|
| | 1 | 2 | 3 | 1 | 2 | 3 | 1 | 2 | 3 |
| 23/09/2017 | 0.281 | 0.218 | 0.255 | 0.102 | 0.227 | 0.303 | 0.496 | 0.629 | 0.696 |
| 04/03/2018 | 0.261 | 0.208 | 0.248 | 0.216 | 0.358 | 0.395 | 0.325 | 0.205 | 0.175 |
| Difference residual | 0.02 | 0.009 | 0.007 | -0.116 | -0.131 | -0.092 | 0.171 | 0.424 | 0.521 |

In the residual difference image, a threshold value was applied to differentiate water features from other land cover classes. Thus, defining the difference NDVI threshold value to discriminate water features from non-water was based on the pixel-by-pixel evaluation (Table 5-3). Selecting a wrong threshold value can result in over/under-estimating flood extent. Therefore, based on the pixel-by-pixel assessment and visual inspection of the residual map on the affected areas, the threshold value of $>= 0.065$ was used to separate water features from other land cover classes on the residual difference map because it fairly classified the flooded areas (refer to affected areas). The change detection approach delineated water features in the acquired Planetscope images. However, the inundation map derived from the post-flood image still shows a misclassification of non-water features to surface water in the high elevated areas (Figure 5-7). This effect was attributed to the similar difference (i.e., equivalence) in residual NDVI values of areas affected by flood and other land surface features. Figure 5-7 shows that inundation extent derived from Planetscope satellite images after masking out clouds and before HAND filtering in the model domain.
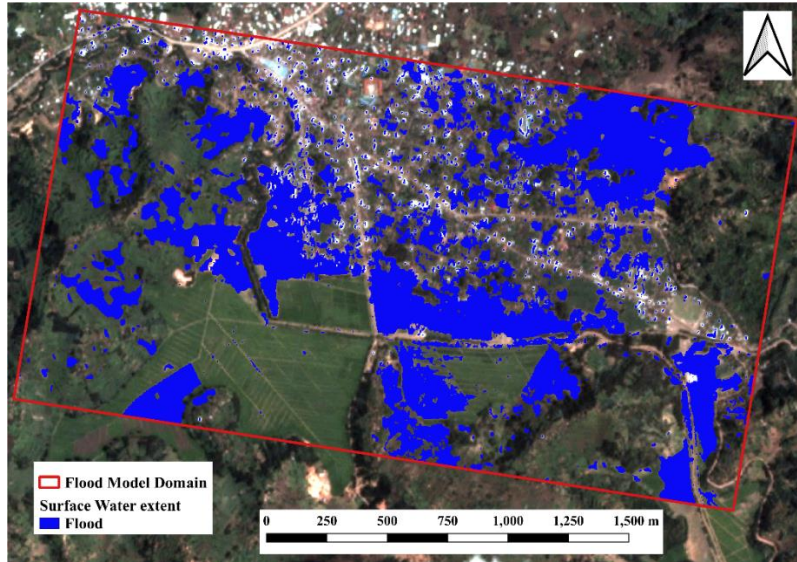
Figure 5-7 Planetscope satellite-derived surface water map of the model domain on 04/03/2018

### 5.2.1. HAND filtering approach

The HAND product was created using the 1m × 1m resolution DEM in the flood model domain. A threshold value of 20000 cells, established manually, was applied to define the drainage network in the flow-accumulation map. Figure 5-8 describes the normalized topography from the HAND model where areas having elevations below or equal to 3m, with topographic reference to the drainage network, were considered susceptible flood-prone areas. The HAND model results were observed to cover the flood-prone areas in the model domain, namely the Mahoko market and tea plantation on the left side of the Sebeya river. The HAND model was applied to limit the misclassification of surface water features detected from the Planetscope satellite image in the flood model domain. The HAND model provides information on flood-vulnerable areas based on the available DEM products (Bhatt and Srinivasa Rao, 2018). The HAND filtering operation was applied on the Planetscope image to detect inundation extent in flood-prone areas.
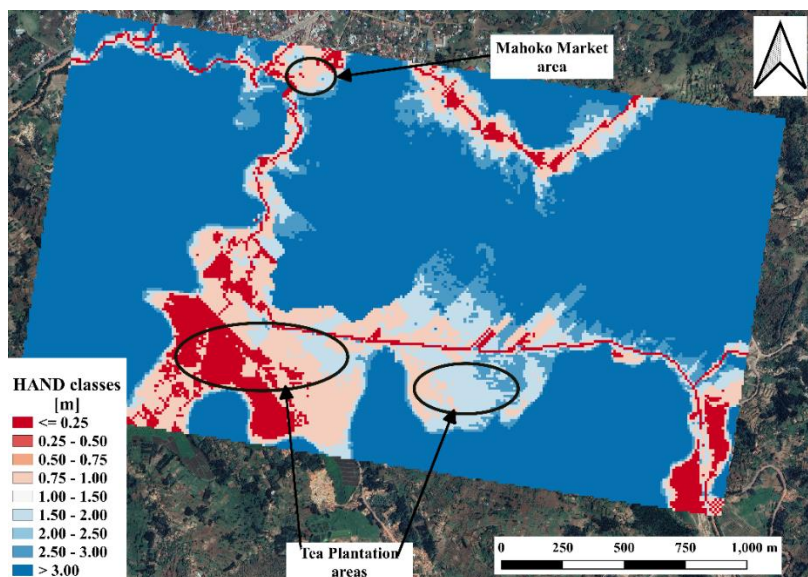


Figure 5-8 Potential flood-prone areas prepared using drainage patterns evaluation (HAND model)

Figure 5-9 describes the Planetscope satellite-derived inundation extent of the model domain after HAND filtering applications. The HAND filter was applied to the Planetscope image to remove water features that appeared in the elevations higher than the selected HAND threshold class (<= 3m). The results describe the ability of the HAND filtering approach to enhance flood extent derived from satellite images and limit the water surface features in non-flood-prone areas.
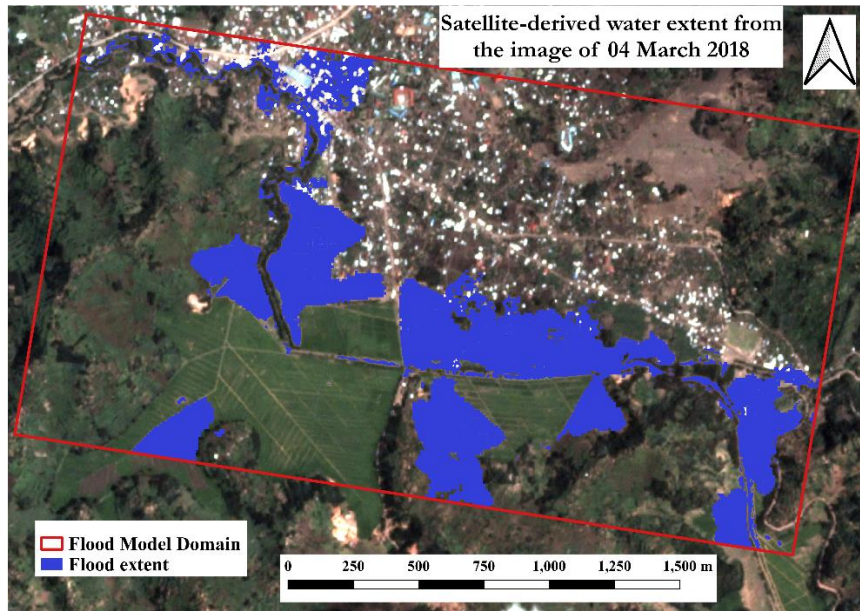


Figure 5-9 Planetscope flood map after HAND filter of the model domain

## 5.3. Satellite based-rainfall assessment

### 5.3.1. Point-to-pixel evaluation

The daily SREs (CHIRPSv2 and TAMSATv3.1) were compared with rain gauge stations where statistical measurements (Table 5-4) were used to evaluate their performance. Table 5-4 describes the results where all satellite products showed low correlation coefficient values ($0.1 \leq r \leq 0.3$) with daily rain gauge observations at all stations. The lowest and highest correlation was observed for TAMSAT at the Kabaya station ($r \approx 0.2$) and Nyundo station ($r \approx 0.3$), respectively. The TAMSAT satellite product depicts a high RMSE value (rmse = 10.1 mm per day) for Kabaya station, while the CHIRPS satellite presents the lowest RMSE value (8.2 mm per day) at the Bigogwe station. Overall, CHIRPS demonstrates a smaller RMSE value than the TAMSAT satellite product.

Table 5-4 Daily Statistical assessment results of different SREs with reference to ground stations (2014-2018)

| Stations | CHIRPSv2 | | | | TAMSATv3.1 | | | |
|---|---|---|---|---|---|---|---|---|
| | rBias [%] | RMSE [mm] | r [-] | ME [mm] | rBias [%] | RMSE [mm] | r [-] | ME [mm] |
| Nyundo | -10.6 | 8.3 | 0.2 | -0.4 | -6.4 | 9.1 | 0.3 | -0.2 |
| Bigogwe | 16.2 | 8.2 | 0.2 | 0.5 | -1.8 | 8.7 | 0.3 | -0.1 |
| Kabaya | -0.3 | 9.4 | 0.2 | -0.1 | -17.2 | 10.1 | 0.2 | -0.6 |

All SREs present an underestimation with negative relative Bias for most stations, where large uncertainties were observed at the Kabaya station for the TAMSAT satellite (rBias = -17.2 %). Kabaya station shows also a small rBias value (rBias = -0.3 %) for CHIRPS SRE. An overestimated rainfall was observed only at Bigogwe station for CHIRPS SRE (rBias = 16.2 %). Overall, CHIRPS presents less rBias values compared to the TAMSAT satellite product. All satellite products underestimate daily rainfall with a mean of errors from 0.1 mm (CHIRPS at Kabaya station) to 0.6 mm (TAMSAT at Kabaya station), except Bigogwe station, which overestimates daily rainfall (ME = 0.5 mm). Overall, the CHIRPS product possesses minor errors on a daily scale, followed by TAMSAT.

Statistical measurements vary across stations for all satellite products, which is explained by different techniques for recording rainfall for each SRE. Regardless of r and RMSE, CHIRPS fairly represents the rainfall in the Sebeya catchment compared to the TAMSAT satellite product from the overall evaluation of statistical criteria. Authors like Dinku et al. (2018) indicated a high correlation coefficient value for CHIRPS products in Rwanda compared to other products investigated in East Africa. Nkunzimana et al. (2020) also revealed that CHIRPS products provide valuable and reliable information for meteorological disasters in Burundi, a neighboring country to Rwanda.

### 5.3.2.    Defining window length and bias correction method

The RMSE results of bias-corrected satellite products using SW and MW methods are used to define suitable window length and bias correction methods. Both approaches (SW and MW) for bias correction were evaluated because no literature or research has been conducted for the Sebeya catchment to guide this research on which method could be applied most appropriately. Therefore, RMSE values for each time window for both approaches were plotted to define the window length for which it can be argued that the final scheme is suitable for the study area. Figure 5-10 depicts the remarkable increase in RMSE values as window length increases from 3 days to 6 days sampling window for both satellite products. All stations display only very little increase in RMSE values after 7 days window length, except Nyundo station, which shows variations in RMSE values for the TAMSAT product. Kabaya station for CHIRPS does not display a remarkable difference in RMSE values for the SW approach, but it reveals an increase in RMSE up to 6 days window size. Kabaya station depicts an increase in RMSE from 3 to 12 days when using the MW approach for the TAMSAT product. The RMSE values of uncorrected SREs are presented in Table 5-5. For all satellite products, all stations produce better results than the raw SREs data for 3 days and a larger time window length (comparing Table 5-5 and Figure 5-10). Therefore, from the above analysis and general patterns of stations in RMSE variations, 6 days window length was selected in this research. Bhatti et al. (2016); Habib et al. (2014) found that 7 days window size performed well to correct Bias in CMORPH rainfall data in the Gilgel Abbey watershed, and the corrected CMORPH rainfall revealed better performance in the hydrological model. However, in this research, 6 days window size was found to be the optimum window. This window length was selected because the analysis of RMSE values for a window length of 3, 5, 6, 7, 10, 12, 15, 17, and 20 do not present considerable RMSE differences after 6 days for SW and MW approaches for all satellite products (Figure 5-10).

Table 5-5 RMSE of raw satellite data

| Satellite | Nyundo | Bigogwe | Kabaya |
|-----------|--------|---------|--------|
| **CHIRPS** | 8.3 | 8.2 | 9.4 |
| **TAMSAT** | 9.1 | 9.4 | 10.1 |
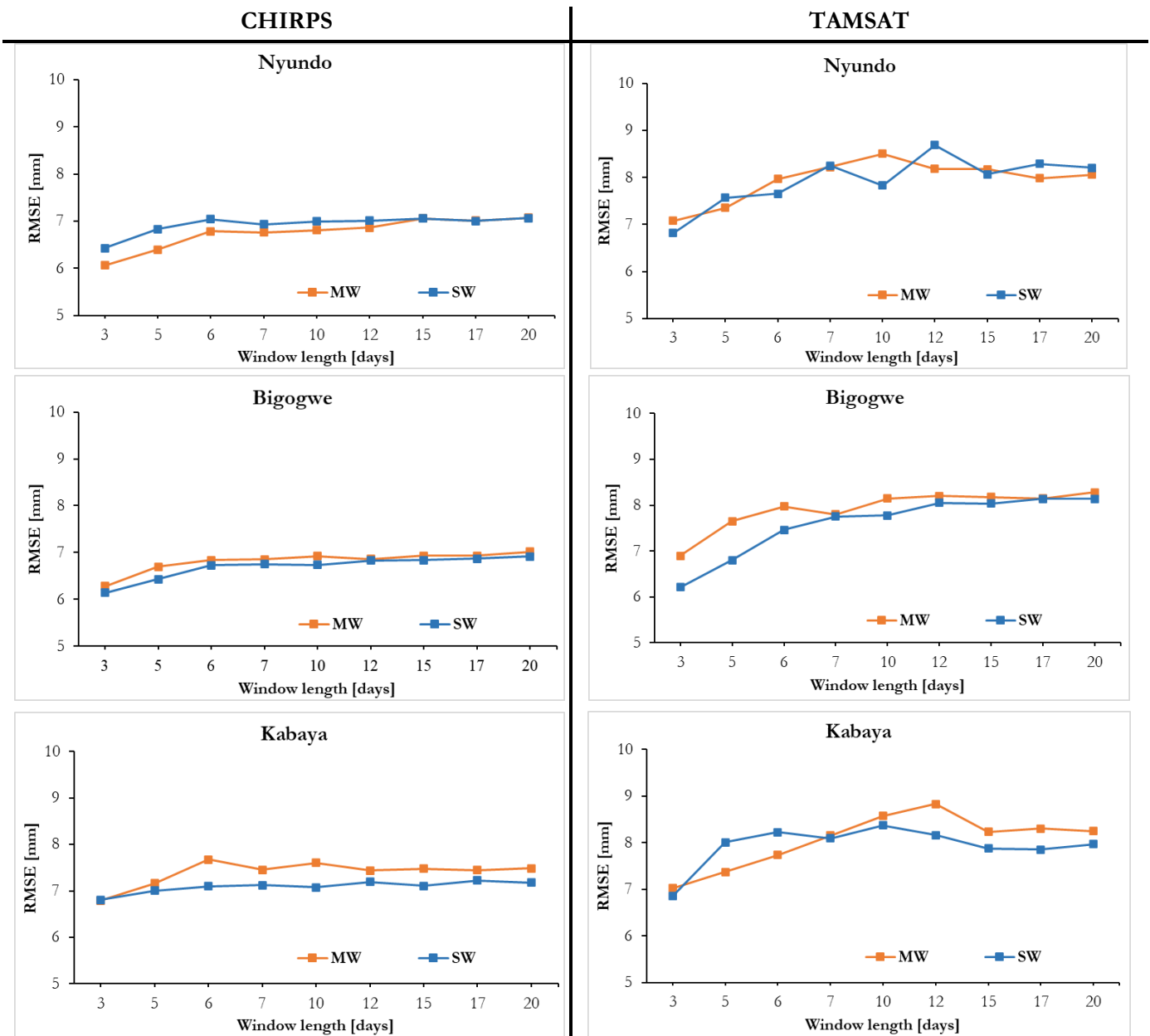
Figure 5-10 Results of RMSE for SW and MW methods on CHIRPS and TAMSAT SREs

After selecting the window size, the suitable approach for the Sebeya watershed was analyzed. Figure 5-11 shows the cumulative differences after bias correction at 6 days window size for CHIRPS and TAMSAT from 2014 to 2018 using both SW and MW approaches. All stations and satellite products do not behave the same after bias correction, which can be associated with different techniques used to estimate rainfall in each satellite product. Figure 5-11 describes that no single approach (SW or MW) could be applied to all SREs, challenging the selection of a suitable method for bias correction in the Sebeya catchment. However, the CHIRPS product indicates less cumulative rainfall differences for the SW method, whereas TAMSAT presents less accumulated rainfall differences for the MW method. Therefore, 6 day SW sampling window for CHIRPS and MW approach for TAMSAT were selected to further application of bias-corrected SREs.
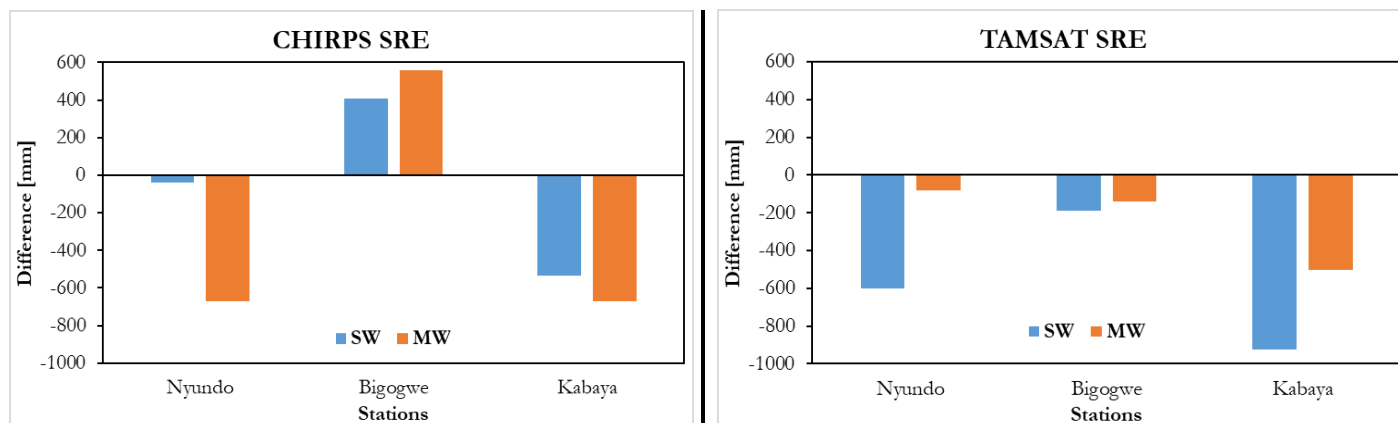
Figure 5-11 Cumulative difference results for 6 days window size for SW and MW bias correction

### 5.3.3. Sub-basins scale analysis

After evaluating the representation of SREs on each station available in the study area and selecting the sampling window and bias correction method, SREs were assessed on a sub-basin scale. Thiessen polygon approach was applied to estimate the aerial rainfall spatially from ground-based observations on each sub-basin, while the pixels of satellite rainfall products were averaged over each sub-basin. The year 2018 was selected in this process because it will be further applied in the hydrological model to estimate the streamflow.

### 5.3.3.1. SREs performance evaluation

The daily rainfall averaged over sub-basins from rain gauges and satellite products were compared using the same statistics described in section 4.4. Table 5-6 indicates the performance of SREs over five sub-basins in the Sebeya catchment. All sub-basins for all SREs, except the Karambo sub-basin for CHIRPS satellite product which has a positive relative bias (rBias = 0.9 %) and mean error (ME ≈ 0.1 mm per day), possess negative rBias and ME values, that indicates the underestimation of satellite rainfall products, ranging from 1.6 % to 23.1 % and 0.1 mm to 1.2 mm per day, respectively. The highest values of rBias and ME were observed at the Bihongora sub-basin for the TAMSAT product. The RMSE values are slightly in the same range as point-to-pixel analysis, ranging from 7.7 to 12.0 mm per day. The Sebeya upstream sub-basin presents a low RMSE value for the CHIRPS product, while Sebeya downstream sub-basin possesses a high RMSE value for the TAMSAT satellite product.

Table 5-6 Daily Statistical assessment results of different SREs over sub-basins (2018)

| Sub-basins | CHIRPSv2 | | | | TAMSATv3.1 | | | |
|---|---|---|---|---|---|---|---|---|
| | rBias [%] | RMSE [mm] | r [-] | ME [mm] | rBias [%] | RMSE [mm] | r [-] | ME [mm] |
| Sebeya upstream | -16.6 | 7.7 | 0.4 | -0.8 | -20.4 | 10.0 | 0.2 | -1.0 |
| Bihongora | -16.5 | 9.2 | 0.3 | -0.8 | -23.1 | 11.7 | 0.1 | -1.2 |
| Karambo | 0.9 | 8.6 | 0.2 | 0.1 | -1.6 | 9.7 | 0.2 | -0.1 |
| Sebeya downstream | -8.7 | 10.7 | 0.1 | -0.4 | -2.8 | 12.0 | 0.1 | -0.1 |
| Nyundo | -8.2 | 10.6 | 0.1 | -0.3 | -1.4 | 11.5 | 0.2 | -0.1 |

The correlation coefficient (r) was used to assess the relationship between ground-based and satellite-based rainfall over sub-basins. The coefficient values vary from 0.1 to 0.4. The strongest correlation value was obtained at Sebeya upstream sub-basin for CHIRPS SRE, while the Bihongora sub-basin for TAMSAT product shows a weak correlation coefficient. Overall coefficient values reveal that CHIRPS outperforms the TAMSAT satellite product.

### 5.3.3.2.  SREs bias correction evaluation

SREs were bias-corrected to improve their representation over the Sebeya catchment. The sampling window and bias correction approach were defined in section 5.3.2. Bias correction was performed on each sub-basin. The outputs of the bias-correction process are described in Figure 5-12 using Taylor Diagram. The Taylor diagram presents the statistical relation between uncorrected and bias-corrected SREs and the reference (ground-based rainfall observations) in terms of the correlation coefficient, standard deviation, and RMSE. Black contour lines on the Taylor diagram represent RMSE, grey contour lines are for standard deviation, and azimuth angle lines indicate correlation coefficient values. The dotted black line describes the standard deviation of the reference rainfall data.

The Taylor diagram was produced for each sub-basin in the Sebeya catchment. The overall results illustrate that bias-corrected SREs outperform uncorrected SREs for all sub-basins. The correlation coefficient values of corrected SREs range from 0.5 to 0.8. The lowest and strongest correlation values were observed at the Sebeya upstream sub-basin for the TAMSAT satellite and CHIRPS product, respectively. Bihongora sub-basin significantly increases the correlation coefficient value (≈ +0.6) for TAMSAT SRE after the bias correction process. Generally, after bias correction, the CHIRPS satellite product has improved more than the TAMSAT product based on the correlation indicator. The standard deviation (SD) values of uncorrected SREs are below the reference ground rainfall observations SD (except for Sebeya Upstream and Karambo sub-basins for TAMSAT SRE). The SD values of bias-corrected SREs are smaller than the rain gauges SD values for most sub-basins, except at Sebeya upstream and Bihongora for CHIRPS product and Karambo sub-basins for all satellite (CHIRPS and TAMSAT) products. The SD values of corrected SREs vary between 7.1 to 10.5 mm daily. The high value was observed at the Bihongora sub-basin for the CHIRPS product and the low value at the Sebeya upstream sub-basin for the TAMSAT satellite product. After all, SREs products were biased corrected, and the RMSE was reduced across the range in all sub-basins. In the case of bias-corrected SREs, the RMSE values range from 4.8 to 8.3 mm per day. For the TAMSAT satellite product, the Sebeya downstream sub-basin had the highest RMSE, whereas the Sebeya upstream sub-basin had the smallest RMSE. The largest change (a reduction of 4.5 mm per day) in RMSE values between uncorrected and corrected SREs was observed at the Bihongora sub-basin for the TAMSAT product. Therefore, it is revealed that the bias-corrected SREs perform better than the uncorrected SREs with reference to ground rainfall observations because of significant improvement in statistical metrics found after the bias correction process.
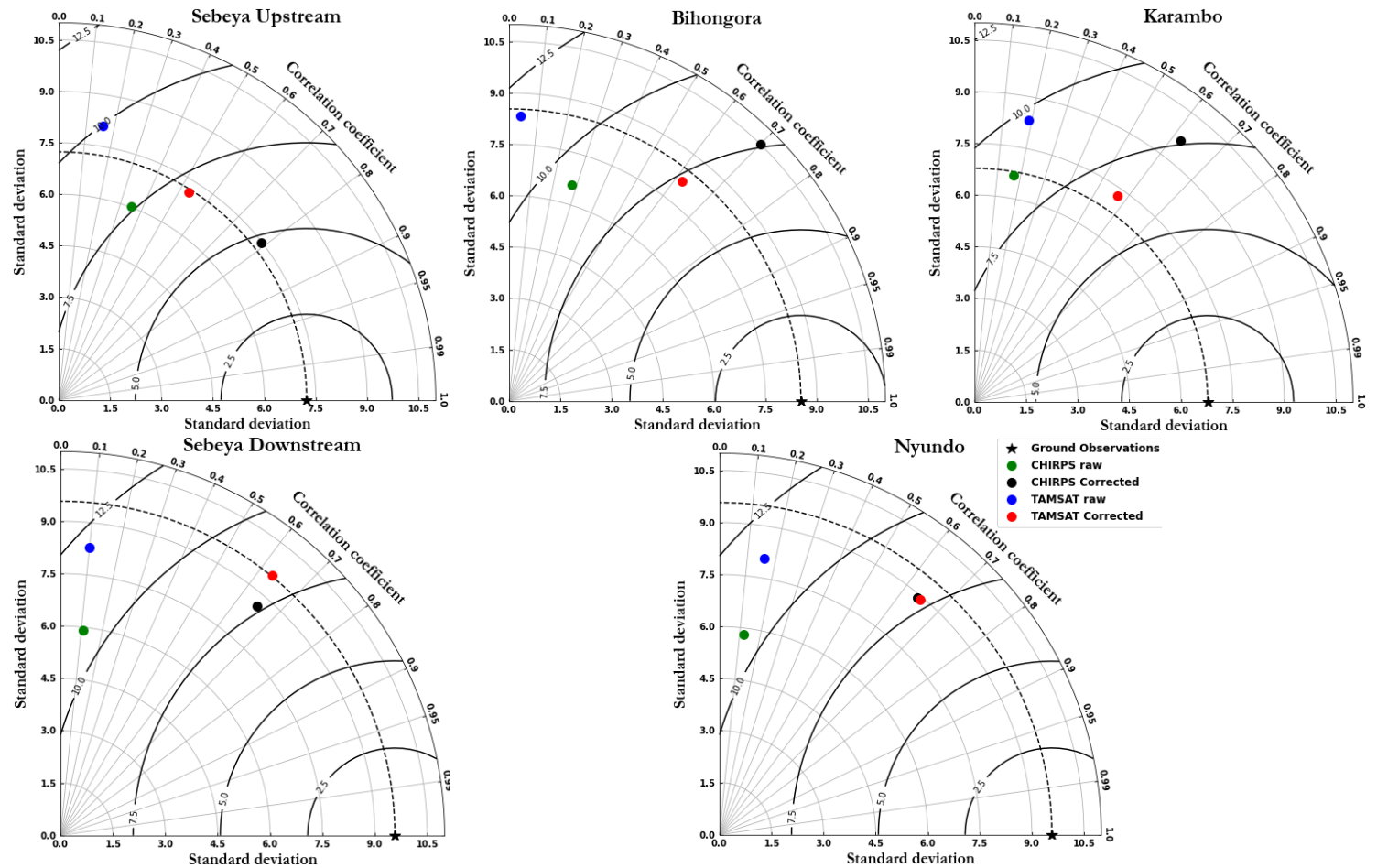
Figure 5-12 Taylor Diagram describing the statistical performance of uncorrected and corrected SREs

In the same context of evaluating the performance of bias-corrected SREs, accumulated rainfall over the whole period (the year 2018), ground-based rainfall, and uncorrected and corrected rainfall from the different satellites were produced to assess the capability of SREs to estimate rainfall amount before and after bias-correction. Figure 5-13 shows the double mass curves of all sub-basin in the Sebeya catchment. All satellite products underestimate rainfall before bias-correction and present an improvement after the bias-correction process at all sub-basins. The bias-corrected satellite products reproduce the accumulated rainfall observed at ground rainfall stations at all sub-basins for CHIRPS SRE. However, except for the Karambo sub-basin that is more likely to produce the accumulated rainfall after bias correction for TAMSAT, the remaining sub-basins for TAMSAT satellite product could not replicate the accumulated rainfall observed at rain gauges. Therefore, the difference in accumulated rainfall amount between the corrected TAMSAT and rain gauge data could be caused by erroneous data from the product's rainfall recordings.
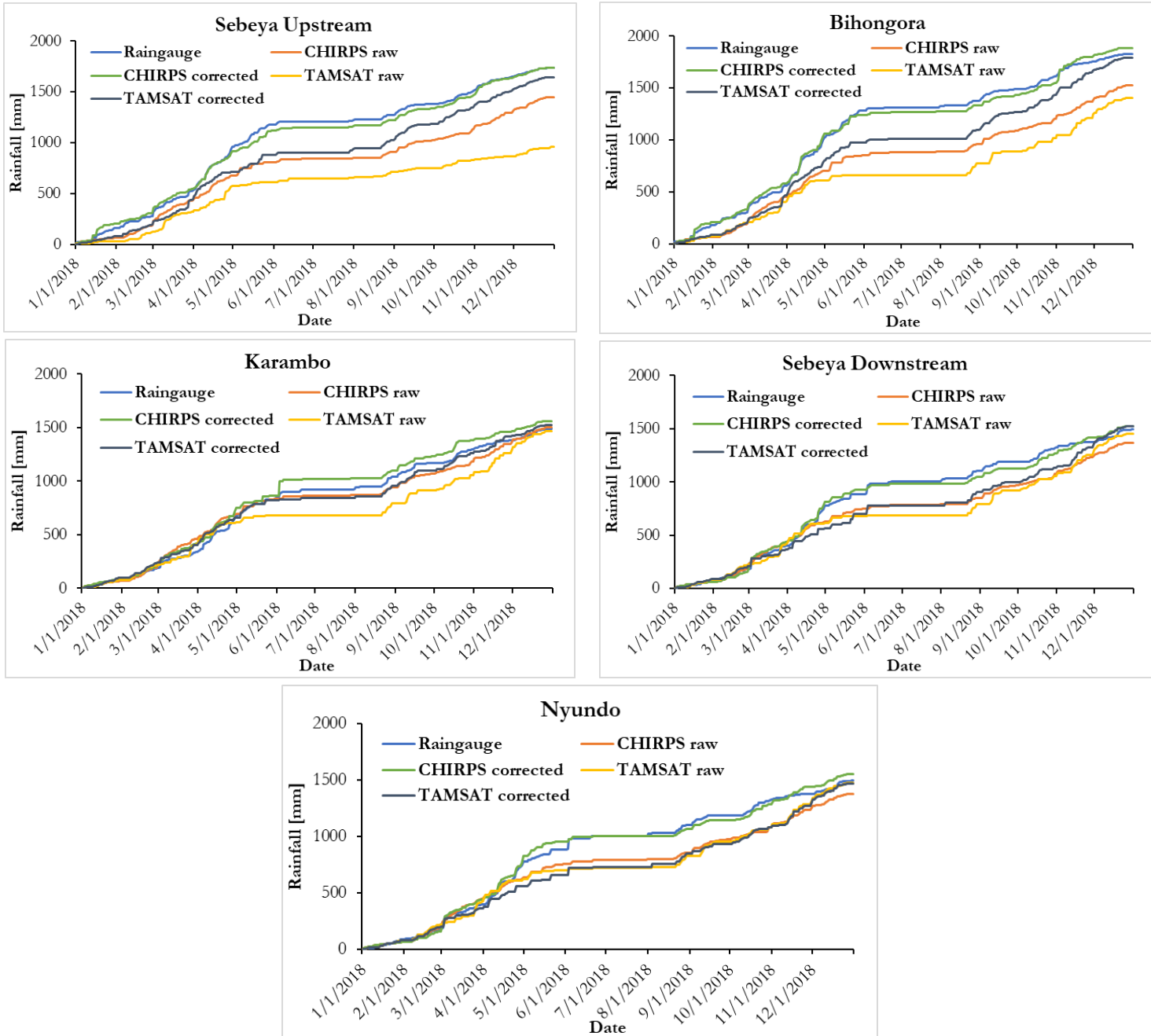
Figure 5-13 The accumulated rainfall amount of sub-basins using rain gauges, uncorrected and corrected SREs

The defects of the TAMSAT rainfall product were evaluated during the rainy season before and after bias correction (see section 4.5). An example in Table 4-4 shows that TAMSAT SRE did not detect rainfall during the rainy season in the Nyundo station. Therefore, the weak rainfall detection capability of the TAMSAT product deteriorates its rainfall recordings even after bias correction during the rainy season for the Nyundo station and other stations in the Sebeya catchment. For this reason, the defects of the TAMSAT to detect rainfall were propagated on the sub-basin scale recordings, which were also developed during the bias correction process. Table 5-7 shows an example of error propagation of the TAMSAT satellite product, where corrected CHIRPS and corrected TAMSAT were presented for the Nyundo sub-basin. It can be observed that after bias correction, the poor rainfall detection ability of the TAMSAT product propagated on the sub-basin scale rainfall estimates, and thus its further use of the product. Yet, the weaknesses in the

TAMSAT could be attributed to its algorithm developed for low rainfall recordings, serving in the drought monitoring practices (Kimani et al., 2017). Tarnavsky et al. (2014) also found that TAMSAT presents a limited ability to detect rainfall during the rainy season. Therefore, this weakness is propagated during bias-correcting the TAMSAT data (Figure 5-13). Nevertheless, the bias-corrected TAMSAT satellite data performs better than the raw TAMSAT data and can be accepted for the hydrological modeling applications in the Sebeya catchment. Therefore, the TAMSAT detected rainfall should be applied attentively to avoid the bias that the product could enforce in the hydrological modeling.

Table 5-7 Example of error propagation of TAMSAT satellite product

| DOY | InSitu Rainfall | Uncorrected CHIRPS | Corrected CHIRPS | Uncorrected TAMSAT | Corrected TAMSAT |
|---|---|---|---|---|---|
| **105** | 19.8 | 5.5 | 7.1 | 21.6 | 11.6 |
| **106** | 2.5 | 9.0 | 6.8 | 0.0 | 0.0 |
| **107** | 0.3 | 9.0 | 6.8 | 13.4 | 9.8 |
| **108** | 3.8 | 4.5 | 3.4 | 0.3 | 0.4 |
| **109** | 0.0 | 11.2 | 8.1 | 17.9 | 13.5 |
| **110** | 0.8 | 0.0 | 0.0 | 0.0 | 0.0 |
| **111** | 0.5 | 5.8 | 4.1 | 0.0 | 0.0 |
| **112** | 11.1 | 0.0 | 0.0 | 0.0 | 0.0 |
| **113** | 14.1 | 7.9 | 11.0 | 0.0 | 0.0 |
| **114** | 8.1 | 0.0 | 0.0 | 0.0 | 0.0 |

Therefore, from the above evaluations, it can be revealed that the applied bias-correction methods increased the relationship between the rainfall from rain gauges and CHIRPS and TAMSAT satellite products. At the same time, it could not reproduce the accumulated rainfall amount for the TAMSAT product at almost all sub-basins. However, overall, the CHIRPS satellite product performed better than TAMSAT regarding its strong correlation with ground-based rainfall and estimating rainfall amount. Therefore, it is deduced that SREs should be analyzed in terms of statistical performance and estimation of rainfall amount after bias correction and before their application in hydrological modeling or other water resources practices. This research accepted bias-corrected satellite products and InSitu rainfall data for the hydrological modeling practice in the Sebeya catchment.

## 5.4.    Rainfall-runoff model

### 5.4.1.    HBV model simulation and parameterization

The streamflow of the Sebeya river was simulated using HBV-light hydrological modeling for different rainfall input datasets. The modified streamflow observations for the Sebeya river at Nyundo station were used for the model calibration process. The model was firstly tested and calibrated using InSitu rainfall forcing data where the default parameters (Table 5-8) were optimized till the acceptable NS and RVE were found.

Table 5-8 HBV model defaults parameters (Seibert, 2005) and optimized parameters for the Sebeya catchment

| Routines | Parameter | Value range | Units | Default value | Optimized value |
|---|---|---|---|---|---|
| Soil Moisture routine | FC | (0, inf) | mm | 200 | 380 |
| | LP | [0, 1] | - | 1 | 0.75 |
| | BETA | (0, inf) | - | 1 | 1.05 |
| Response routine | Percolation [PERC] | [0, inf) | mm/Δt | 1 | 1.05 |
| | Upper Zone Storage [UZL] | [0, inf) | mm | 20 | 30 |
| | Recession coefficient 0 [K0] | [0, 1) | 1/Δt | 0.2 | 0.15 |
| | Recession coefficient 1 [K1] | [0, 1) | 1/Δt | 0.1 | 0.0015 |
| | Recession coefficient 2 [K2] | [0, 1) | 1/Δt | 0.05 | 0.0045 |
| Routing routine | MAXBAS | [1, 100] | Δt | 1 | 1 |
| NS [-] | | | | | 0.81 |
| RVE [%] | | | | | 5.91 |

Table 5-8 illustrates that the model performs very well with InSitu rainfall forcing data, with an NS of 0.8 and RVE of 5.9 %. Figure 5-14 represents the observed and simulated streamflow hydrographs for the Sebeya catchment. It is observed that the model replicates the observed baseflow during the dry period (Jun-July-August) in the Sebeya catchment. However, the model overestimates the modified peak streamflow observations. The discrepancies (indicated in Figure 5-14 by a black box) during the months of the short rainy season (September-October-November-December) could be caused by the limitation of the model structure to respond to the short rains or errors in the observed streamflow time-series dataset.
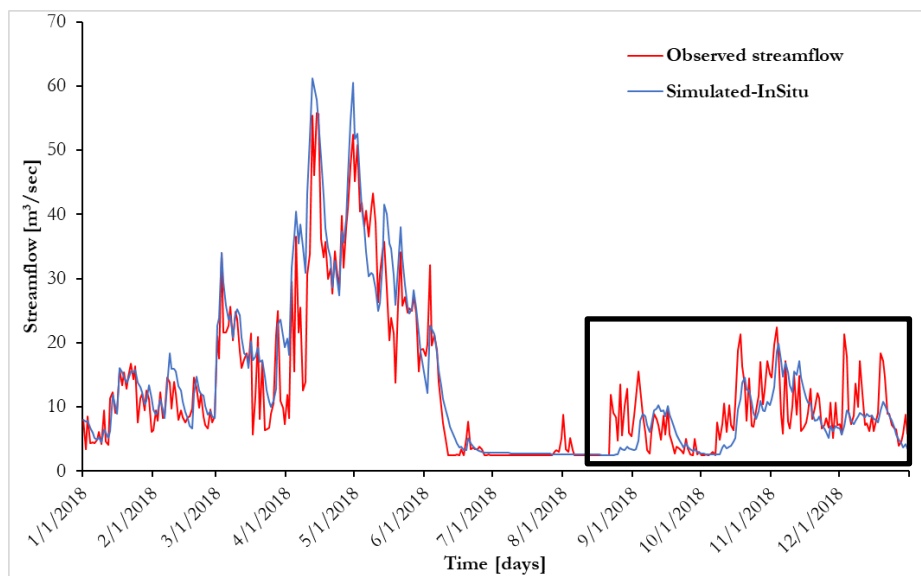


Figure 5-14 Modified observed and simulated streamflow using InSitu rainfall data for the Sebeya catchment

## 5.4.2. Streamflow simulations with SREs

Different rainfall forcing data were used to simulate streamflow in the Sebeya catchment. The SREs, before and after bias-correction, and InSitu rainfall were applied in the HBV model. Table 5-9 describes the optimal HBV model parameter for ground-based and bias-corrected rainfall data for the Sebeya catchment. The streamflow simulated by bias-corrected satellite rainfall was compared with the observed streamflow to assess the performance of the HBV model. It can be observed that the soil moisture routine parameters are sensitive to rainfall forcings.

Additionally, the percolation and storage in the upper zone were tuned to improve the performance of the HBV model for the TAMSAT SRE. The NS values were reduced when using SREs to simulate streamflow in the Sebeya catchment, especially for the TAMSAT product. Besides, the streamflow from CHIRPS SRE shows a reduction in the RVE (2.5 %), while the TAMSAT SRE depicts an increase in RVE in the negative direction (-11.2 %) compared to objective functions produced by InSitu forcing data. The CHIRPS product simulates streamflow reasonably well in the Sebeya catchment, whereas the TAMSAT satellite product insufficiently estimates streamflow with low NS (0.4) and poor RVE (-11.2 %) (see Table 5-9). The results in Table 5-9 indicate that each meteorological forcing requires an independent calibration

Table 5-9 Optimized HBV-light model parameters for InSitu and bias-corrected satellite-based (CHIRPS and TAMSAT) rainfall

| Routines | Parameter | Units | InSitu rainfall | CHIRPS SRE | TAMSAT SRE |
|---|---|---|---|---|---|
| Soil Moisture routine | FC | mm | 380 | 440 | 320 |
| | LP | - | 0.75 | 0.62 | 0.45 |
| | BETA | - | 1.05 | 1.05 | 1.35 |
| Response routine | Percolation [PERC] | mm/Δt | 1.05 | 1.05 | 1.15 |
| | Upper Zone Storage [UZL] | mm | 30 | 30 | 15 |
| | Recession coefficient 0 [K0] | 1/Δt | 0.15 | 0.15 | 0.15 |
| | Recession coefficient 1 [K1] | 1/Δt | 0.0015 | 0.0015 | 0.0015 |
| | Recession coefficient 2 [K2] | 1/Δt | 0.0045 | 0.0045 | 0.0045 |
| Routing routine | MAXBAS | Δt | 1 | 1 | 1 |
| NS | | | 0.81 | 0.77 | 0.42 |
| RVE | | | 5.91 | 2.47 | -11.16 |

From Table 5-9, the bias-corrected CHIRPS SRE outperforms the TAMSAT product to reasonably simulate streamflow in the Sebeya catchment. Besides the objective functions, the streamflow hydrographs from three rainfall forcing data (InSitu, bias-corrected CHIRPS, and TAMSAT) were prepared and presented in Figure 5-15. Figure 5-15 shows that all satellite products could maintain the observed baseflow after calibration. The streamflow estimated by bias-corrected CHIRPS SRE follows the trend of gauge-based streamflow, which is denoted by reasonable model performance metrics (NS and RVE in Table 5-9). However, the TAMSAT SRE could not reasonably simulate the streamflow (as demonstrated in Table 5-9),

where it shows the underestimations and weak recession limb compared to other forcings data (see Figure 5-15). Hence, this has resulted from the deficiencies in TAMSAT rainfall recordings, as illustrated during the bias correction process. The poor replication of observed rainfall for TAMSAT SRE, even after bias-correction, was propagated in the hydrological model of the Sebeya catchment, which caused the poor streamflow estimation using bias-corrected TAMSAT satellite rainfall.
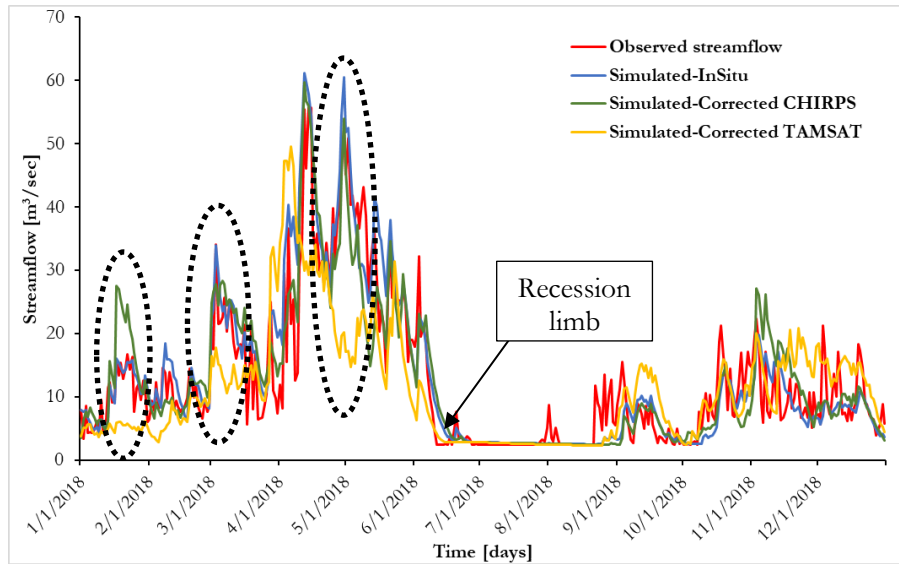


Figure 5-15 Streamflow simulated using gauge-based and bias-corrected SREs for the Sebeya catchment

In the same context, the uncorrected SREs were used to simulate streamflow for the Sebeya catchment. The optimized parameter set for each bias-corrected satellite product was used to estimate streamflow using uncorrected satellite rainfall forcing data (Figure 5-16). Figure 5-16 presents the weakness of uncorrected SREs to simulate streamflow, where they fail to represent the observed streamflow and streamflow estimated by the InSitu rainfall data. The TAMSAT satellite presents an advance of almost a month in the recession limb before the dry period starts in the Sebeya catchment. However, Figure 5-15 describes the improvement in streamflow simulation after bias correcting satellite rainfall products. Still, the TMASAT product continually propagates its deficiencies in detecting rainfall, mainly during the rainy season in the Sebeya catchment.
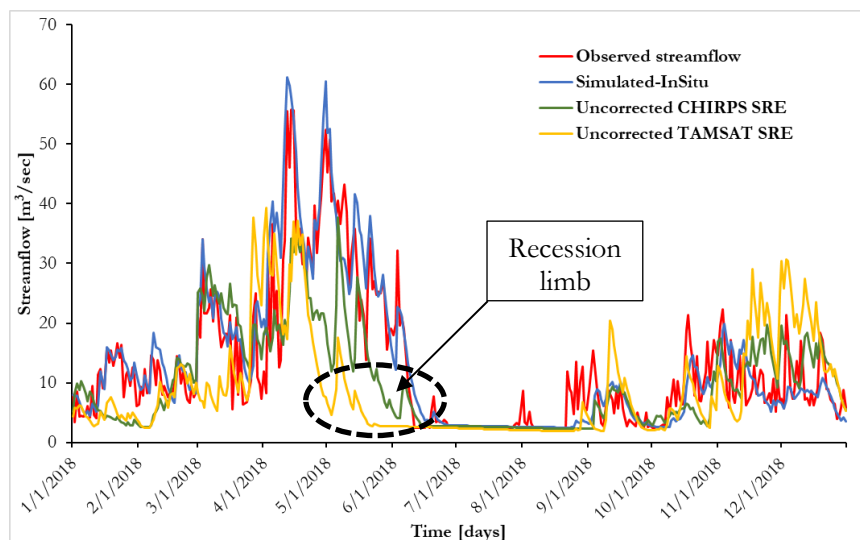


Figure 5-16 Streamflow using InSitu and uncorrected satellite rainfall for the Sebeya catchment

The InSitu and bias-corrected CHIRPS rainfall forcings performed well in simulating streamflow in the Sebeya catchment using the HBV-light model. The defaults in TAMSAT forcing dataset were propagated in the hydrological model even after bias correction. This shows that the uncertainties in the hydrological model were not only caused by the algorithm applied to correct the systematic errors in the available SREs. However, the uncertainties found in the simulated streamflow using InSitu rainfall could be affected by the small number of rain gauge stations available in the Sebeya catchment to represent rainfall's spatial variability adequately. Secondly, artifacts in satellite rainfall recordings consequently propagate in the simulated streamflow, but they could be reduced as indicated for the CHIRPS SRE, which improves after bias correction and simulate reasonable streamflow. On the other hand, the observed streamflow recordings contain errors that could reduce the model's efficiency using different meteorological forcing datasets. Besides the uncertainties found in the model, the available rainfall forcings could reasonably simulate the streamflow in the Sebeya catchment.

### 5.4.3. Inflow boundary conditions of the flood model

The main purpose of setting up the HBV rainfall-runoff model was to simulate streamflow hydrographs to serve as the upstream inflow boundaries in the flood model. Based on the schematization of the flood model domain, the upstream areas contributing to the model domain were found to be Karambo and Sebeya-Downstream sub-basins. The streamflow estimated using the combination of InSitu and bias-corrected CHIRPS SRE rainfall was adopted for the flood model. Figure 5-17 illustrates the streamflow hydrograph of each contributing area, which are inputs in the flood model as inflow boundaries.
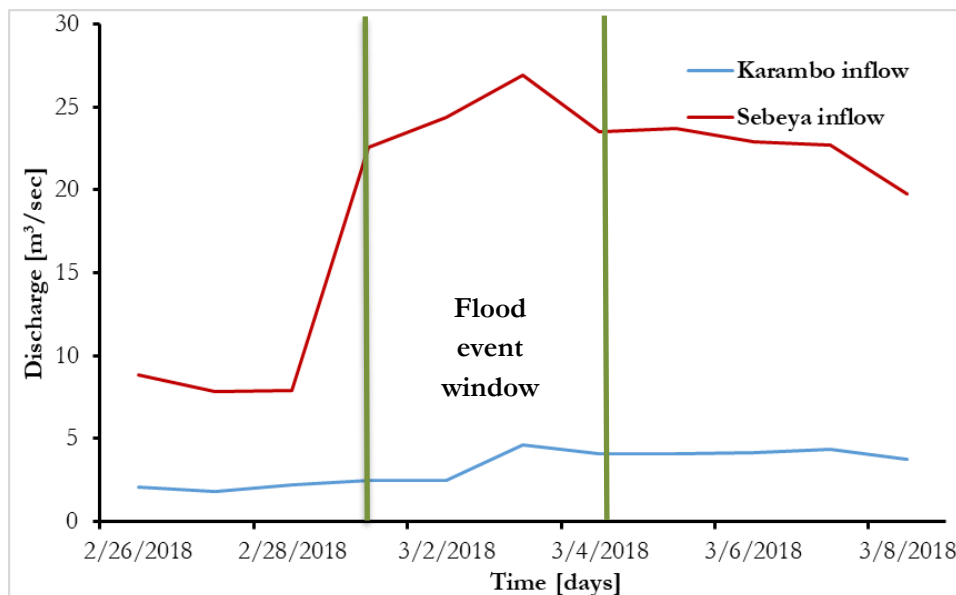


Figure 5-17 Simulated inflow boundaries of the flood model

However, this study intends to analyze the impact of inflow boundary conditions on the hydrodynamic flood model. Figure 5-18 shows the HBV streamflow generated by rain gauges as a reference, bias-corrected, and uncorrected CHIRPS satellite rainfall data for the flood event of 3rd March 2018. It can be observed that there was an improvement in streamflow after CHIRPS bias correction on the Sebeya inflow boundary condition. However, the product did not reproduce the hydrograph generated by rain gauge data. Besides, the streamflow on the Karambo area was changed after the bias correction of the CHIRPS product. Therefore, the impact of the different streamflow hydrographs will be tested in the hydrodynamic model of the Sebeya catchment floodplain.
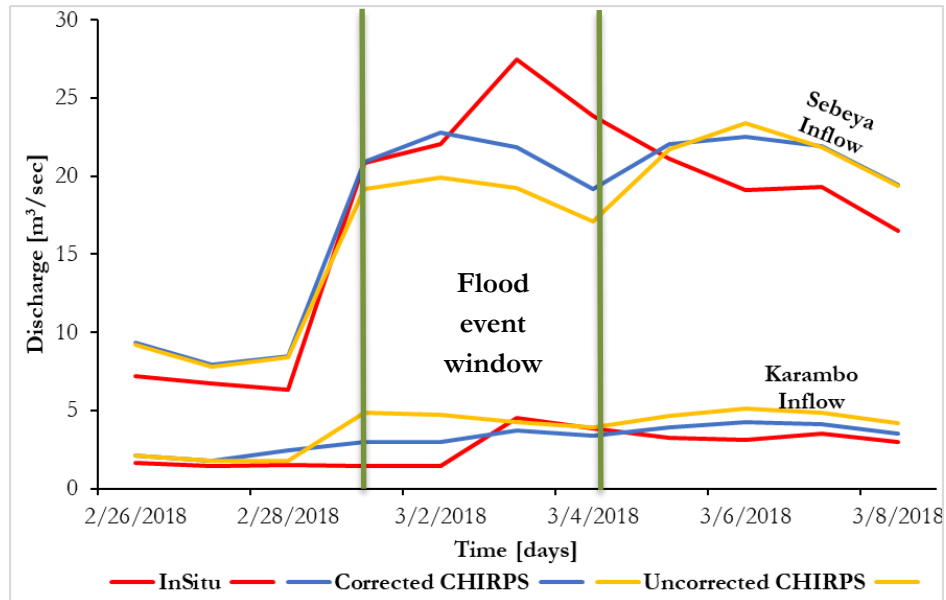
Figure 5-18 Streamflow results from rain gauges, corrected and uncorrected CHIRPS satellite rainfall for hydrodynamic model

## 5.5.    Hydrodynamic model

### 5.5.1.    Effect of topographic representation

This section compares flood extent simulated using the original and enhanced DTM products. Several studies have indicated significant effects of DTM spatial resolution on the flood model outputs where they have pointed out that coarser DTM products worsen the simulated flood model results (Manyifika, 2015; Muthusamy et al., 2021; Xu et al., 2021). However, in this study, the available DTM presented errors in representing surface features as the river reaches. Therefore, it was essential to carry out the DTM enhancement process before using the available DTM in the flood model to reduce the errors found in the topographic representation. Both original and enhanced DTMs were resampled at a similar resolution (1m × 1m spatial resolution) to present the effect of the DTM enhancement method. Identical boundary conditions and the same mesh grid size and land surface characteristics (surface roughness coefficients) were defined on both terrains. Figure 5-19 presents the maximum flood depths using the original and enhanced DEM products in the Sebeya model domain. The processes of improving the DTM are described in section 4.1. It can be well observed visually the importance of DTM enhancement on simulated flood extent in Figure 5-19. The irregularities of topographic representation in original DTM were propagated in model outputs where large flood extent and high maximum depth at the downstream part were simulated in the model domain. However, after enhancing the original terrain and channeling the river, water was conveyed in the channel, and continuous flood extent on the surface was produced. A section was selected in the floodplain better to visualize the effect of the DTM enhancement process.
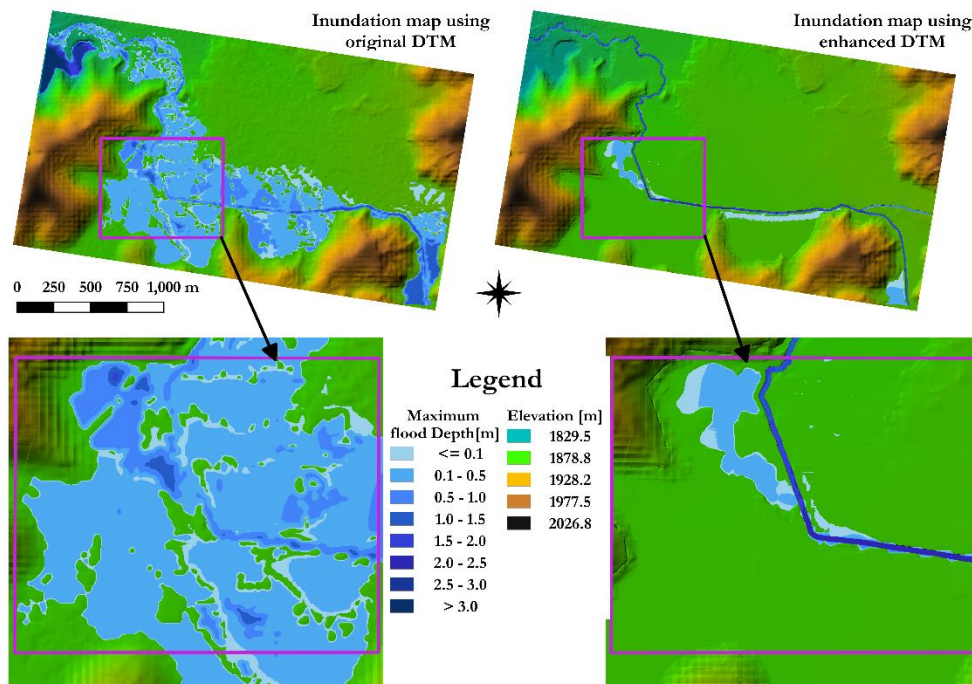
Figure 5-19 Maximum flood depth of different DTM products

The selected part of the floodplain depicts depressions and humps in the original DTM that was enhanced to avoid water storage in those depressions (Figure 5-19). The channel was not well delineated in the original DTM, but after introducing it to the terrain, water could move within the river consistently. Table 5-10 outlines the statistics of simulated flood depth in the model domain. Table 5-10 reveals different mean and maximum water depths for the two DTM products. The original DTM presents a high maximum water depth (8.6 m); after enhancement, the maximum flood depth has increased by almost 74% (Max. depth=2.3 m), which was identified in the river channel. It can also be perceived that the total flood water extent has reduced from 118.3 ha to 15.3 ha (87%) after the DTM enhancement.

Table 5-10 Statistics of simulated flood depth of two DTM products

| DEM products | Max flood depth [m] | | | Area [ha] |
|---|---|---|---|---|
| | **Mean** | **Max** | **STD** | |
| **Original** | 0.509 | 8.610 | 0.849 | 118.3 |
| **Enhanced** | 0.712 | 2.272 | 0.751 | 15.3 |

Therefore, the above results illustrate the essence of DTM enhancement and correction in data-limited areas, like the Sebeya catchment. The enhanced DTM was practically accepted in the hydrodynamic flood modeling of the Sebeya model domain. This is due to its reduction in errors attributed in original DTM to the simulated flood outputs and its increase in the representation of surface features (ex., River channel). Ettritch et al. (2018) have revealed the importance of DTM enhancement and indicated an improvement of topographic representation in the River Gambia floodplain.

### 5.5.2. Effects of inflow boundary condition

The impact of the upstream boundary conditions on the flood model outputs was assessed by changing the input of streamflow. As discussed in previous sections, this study analyses the representation of satellite-

derived rainfall in the Sebeya catchment, with a low number of rain gauges and uneven gauge distribution areas. The streamflow generated from the TAMSAT satellite product was not used in this analysis due to the deficiencies depicted by the product. Therefore, the streamflow generated from the hydrological model using raw and bias-corrected CHIRPS satellite rainfall data and ground observations-based rainfall were used in the flood model to assess their impacts on the model outputs. The enhanced DTM, same mesh grid size, and land cover representation were kept fixed in all simulations. Figure 5-20 shows the maximum flood depth simulated using different upstream inflow boundary conditions. It is observed that changing the inflow boundary condition significantly affects the flood model outputs. From selected spots (in red ellipses) in Figure 5-20, the flood extent is different from each inflow boundary, which is associated with the errors found in satellite-rainfall products and undistributed rain gauges in the Sebeya catchment to represent the rainfall better and reduce errors in the simulated streamflow, that serve as input in the flood model.
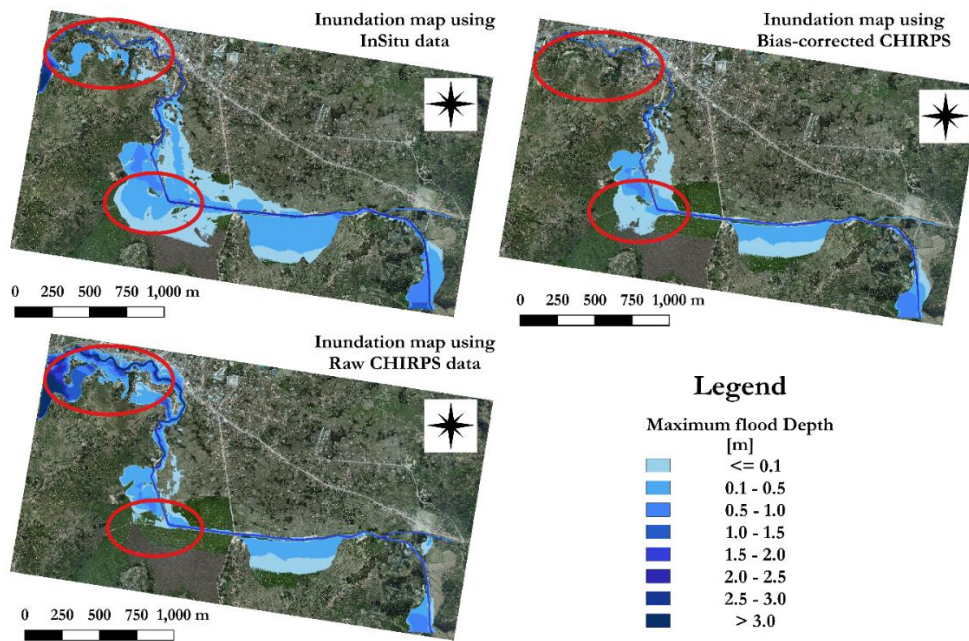


Figure 5-20 Maximum flood depth outputs using different upstream *in*flow boundary conditions

Table 5-11 describes the statistics of simulated maximum flood depths using upstream inflow boundaries generated from InSitu-based, raw CHIRPS, and bias-corrected CHIRPS satellite rainfall. It can be revealed that the raw CHIRPS data generated the highest maximum flood depth during the selected flood window (02-04 March 2018), while after correcting the errors in the satellite, the maximum flood depth has reduced from 7.8 m to 2.3 m (reduction of 70%). The inundation extent area was also affected by the change in the upstream boundary condition, where the inundation area changes with respect to the input upstream flow boundary condition (Table 5-11).

Table 5-11 Statistics of simulated maximum flood depth using different inflow boundary conditions

| Upstream inflow boundary | Maximum flood depth [m] | | | Area[ha] |
|---|---|---|---|---|
| | Mean | Max | STD | |
| Insitu | 0.36 | 4.35 | 0.57 | 81.17 |
| Raw CHIRPS | 0.82 | 7.76 | 1.26 | 54.54 |
| Corrected CHIRPS | 0.35 | 2.34 | 0.51 | 43.26 |

### 5.5.3. Simulation results

Figure 5-21 represents the maximum flood depth and velocity outputs of the 2D HEC-RAS hydrodynamic model for the Sebeya floodplain on 03rd March 2018. A single simulation following the flood window indicated in Figure 5-17 would take almost four hours due to the refined mesh in the river section from 10m × 10m to 1m × 1m grid size. The main Sebeya river gets flooded by water from the Sebeya upstream part, which is filled up by water from upstream sub-basins (Sebeya upstream, Bihongora, and Sebeya downstream sub-basins), and water from the Karambo tributary that gets filled by the water from Karambo sub-basin. However, the main contribution to flooding is the Sebeya river due to a large amount of water from the upstream mountains and high rainfall from the Gishwati forest. However, the available topographic representation in the model domain could affect the simulated flood model results.
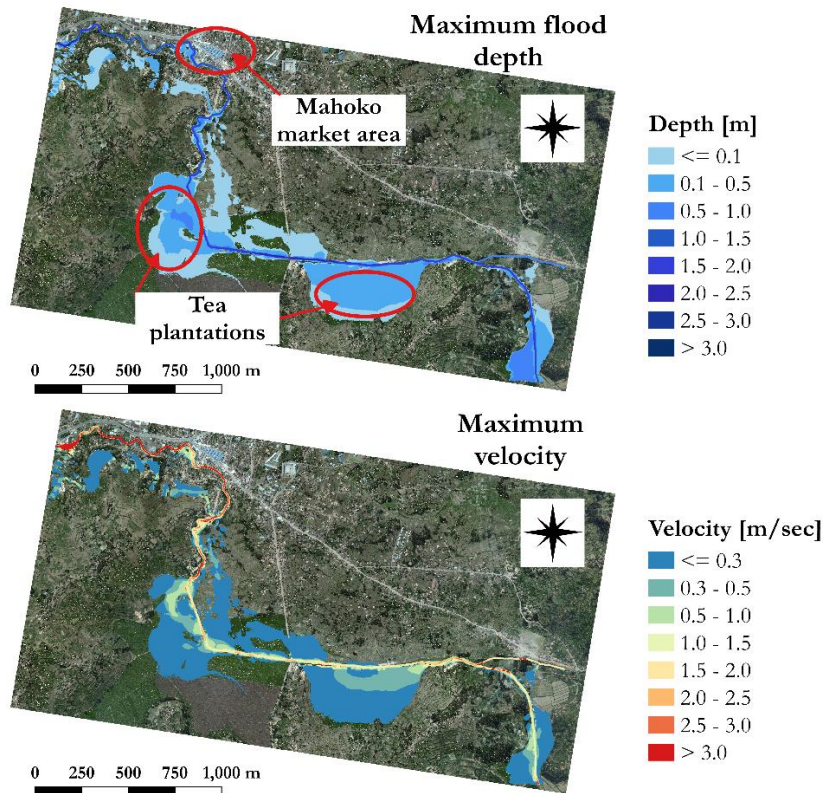


Figure 5-21 Simulated maximum flood depth and velocity

Figure 5-21 depicts that the maximum flood depth was simulated within the river channel (max. depth >=2m). This is attributed to the delineation of the river reach during the DTM enhancement process. Maximum velocity also was observed in the river reach. Besides, the model inundation extent appears reasonable in the tea plantation areas, while water didn't reach the Mahoko market. This results from discrepancies in the DTM used during flood model simulations. Besides all the efforts made to enhance and correct the available DTM, it still presents defects that could not be removed completely. However, there were no on-site flood depth recordings inside the model domain to evaluate the effectiveness of the flood model. Additionally, the available DTM didn't comprise elevation for land surface features like bridges, roads, and buildings, resulting in a continuing simulated inundation extent. Regardless of the difficulties encountered in the topographic representation, the 2D HEC-RAS hydrodynamic model simulated reasonable and representational inundation extent for the Sebeya floodplain.

### 5.5.4. Comparison of model simulated flood extent and satellite-derived water extent

One of the motives for carrying out this research was to investigate the application of satellite-derived flood extent in the calibration of the hydrodynamic model of the Sebeya catchment. The surface roughness coefficients for each land use were considered as calibration parameters. The calibration was performed to better match satellite-derived, and 2D HEC-RAS hydrodynamic model simulated flood extent in the model domain.

The inundation extent extracted from Planetscope optical satellite image acquired on 4th March 2018 at 7:48 AM was compared with the simulated flood extent that occurred on 3rd March 2018 around 4:00 PM (EFRC, 2018) in the Sebeya catchment. The critical surface index (CSI) measure of fit was used to compare the Planetscope satellite-derived and simulated inundation maps. A better fit would indicate the significant application of a satellite-extracted inundation map to calibrate the hydrodynamic models. Table 5-12 shows the results of the comparison between satellite-derived and simulated inundation extent.

Table 5-12 Statistical comparisons of satellite-derived and simulated inundation extent

| Satellite image | Area [ha] | | | CSI |
|---|---|---|---|---|
| | Flood extent in satellite and simulated observations | Flood extent in satellite observations only | Flood extent in simulated observations only | |
| Planetscope | 24.6 | 54.4 | 37.1 | 0.2 |

Table 5-12 presents a low value of CSI (0.2) when comparing the Platenscope stellite-derived, and 2D HEC-RAS simulated inundation extent. This indicates a mismatch between satellite-derived and simulated water maps, as the CSI should be close to 1 for a better match. The mismatch could be caused by the change detection method used to delineate water from the satellite, the coverage of the vegetation over the river, and defects in the Planetscope image. Figure 5-22 clearly describes the comparison of satellite-extracted and simulated water maps.
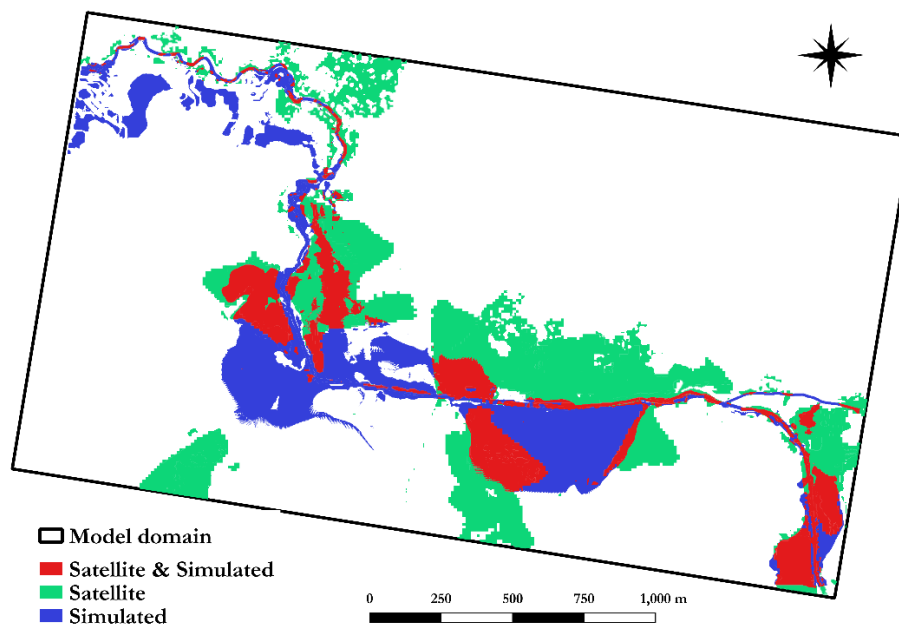


Figure 5-22 Comparison of Planetscope satellite-derived and model simulated flood extent

Figure 5-22 deduces that the comparison results between satellite-derived and simulated flood extent were inadequate for the Sebeya catchment model domain. It can be visually observed that the satellite could not detect the river reaches because of trees on the banks of the rivers. Another misfit would be caused by the same reflectance of the Sebeya river and dry lands, which could be discarded during surface water extraction. The Sebeya river contains a lot of sediments that change the color of water reflectance. Additionally, the higher reflectance values in the NIR than the green for surface water pixels were found in Planestcope, which could cause the misfit, and it has influenced this study to use the NDVI differencing change detection, which caused the disqualification of water pixels in the river. The available DTM used in the flood model could cause defects in the simulated flood extent, thus reducing the matching between the satellite-based and simulated inundation extent. Therefore, from the above uncertainties, the Planetscope could not be used in calibrating the hydrodynamic model of the Sebeya catchment floodplain.

# 6.    CONCLUSION AND RECOMMENDATION

## 6.1.    Conclusion

The main objective of this research is to investigate the applicability of satellite-based rainfall estimates (SREs) and satellite-derived inundation extent to perform hydrodynamic flood modeling of the floodplain in Sebeya catchment, Rwanda. The limited research conducted in the area, data scarcity, and poor quality of available data were the challenges and primary considerations of the Sebeya catchment. However, the hydrodynamic model requires calibration using ground flood extent or depth observed during the flood event, which was unavailable from the site. Therefore, this results in assessing the application of satellite-derived flood extent to calibrate the hydrodynamic model of the Sebeya floodplain. The only satellite image available for the respective flood time window was Planetscope, which was further processed and used in this study. However, the uneven spatial distribution of rain gauges in the Sebeya catchment necessitates the application of satellite rainfall estimates to consider the spatial variability of rainfall in the hydrological modeling. The CHIRPS and TAMSAT satellite product errors were assessed and bias-corrected for further use in the hydrological model.

The change detection method of NDVI's image differencing was applied to extract inundation extent from the Planetscope optical image. The difference between the Planetscope images acquired on 23/09/2017 (before flooding) and 04/03/2018 (after flooding) was achieved by computing the NDVI of each image and then subtracting the NDVI of the image after the flood from the image before flooding. However, the main challenge in this study was to get an image that could capture a flood event in the Sebeya catchment. Nevertheless, the acquired image presents drawbacks like the presence of clouds and shadows in the image and masked water within the river by the vegetation. It was challenging to detect water from the NDVI difference image. Besides, pixel-by-pixel investigation and reasonable inundation extent extracted from the image guided the selection of optimum threshold to delineate surface water. The residual difference presents zero values in areas with no change, negative values for areas with vegetation increase, and positive values in areas where vegetation was removed from the site, which indicates the areas affected by flooding. A threshold of 0.065 was used to extract inundation areas. However, the HAND model was adopted in this study, which deduces the nearest locations closest to nearby drainage that are susceptible to flooding. Therefore, the HAND model indicates its significant application in enhancing the satellite-derived inundation extent.

The daily rain gauge data from three stations (Kabaya, Bigogwe, and Nyundo) were used to evaluate the performance of the CHIRPS and TAMSAT satellite products in the Sebeya catchment. Overall, the daily assessment indicates that all satellite products underestimate rainfall amount where the daily mean errors from -0.1 to -0.6 mm/day were estimated, except the CHIRPS product at Bigogwe station, which overestimates daily rainfall of 0.5 mm/day. All satellite products at all stations reveal a weak correlation measure (below 0.5). Therefore, the general evaluation indicates a better performance of CHIRPS product than TAMSAT when compared with ground-based rainfall. However, the systematic errors found in the SREs were corrected in this study.

The Spatio-temporal bias correction scheme, the time-space variable, was used to correct the bias in the CHIRPS and TAMSAT SREs. However, no research was conducted regarding the SRE bias correction. Therefore, an optimum window size was defined in this study following the method applied by Bhatti et al. (2016). The sampling window size on which the RMSE does not show significant changes was selected. It

was found that the lowest RMSE values were detected at 3 days window size, and an increase in sampling window size resulted in an increment of RMSE values for all satellite products (see Figure 5-10). However, this study found small changing RMSE values from 6 days sampling window to larger window sizes, which was selected as the optimal sampling window to bias-correct CHIRPS and TAMSAT SREs. The MW and SW bias correction approaches were examined, where based on cumulative rainfall differences between the rain gauges recordings and bias-corrected satellite rainfall data (Figure 5-11), the SW approach outperforms MW for the CHIRPS product, and the MW approach depicts better performance than SW for the TAMSAT satellite. Therefore, those approaches were used on the sub-basin scale to generate rainfall for hydrological modeling. However, discrepancies were found in the TAMSAT satellite even after bias correction, which was caused by the weak rainfall detection of the product during the rainy season in the Sebeya catchment. This weakness propagated during bias correction and further in the hydrological modeling. Therefore, it was argued that the TAMSAT SRE could be cautiously used in hydrological applications.

The HBV hydrological model was used in this study, where different rainfall forcing data were used. The model was firstly parameterized using InSitu rainfall recordings. The modified (observed) streamflow data was used in the calibration process. The InSitu rainfall data depicts a better model performance with NS of 0.8 and RVE of 5.9 % after calibration. However, changing rainfall input data in the HBV model resulted in the independent optimized parameters. The soil moisture routine parameters were found sensitive to different rainfall input data. The bias-corrected CHIRPS rainfall data reasonably simulate streamflow of the Sebeya catchment with NS of 0.8 and RVE of 2.5 %. Besides, the bias-corrected TAMSAT rainfall data poorly simulated streamflow, resulted from the product's lack of rainfall detection capability, mainly during the rainy season. The raw satellite rainfall data were used to simulate streamflow of the Sebeya catchment using the independent optimized parameters of each satellite using bias-corrected rainfall data. The raw SREs poorly reproduce the observed streamflow data. Therefore, the streamflow generated using a combination of InSitu and bias-corrected CHIRPS rainfall data was used in the flood modeling.

The 2D HEC-RAS hydrodynamic model was used to simulate flood characteristics in this study. The upstream inflow boundary conditions were obtained from the hydrological model for the Sebeya and Karambo river reaches. However, the inadequate topographic representation introduces uncertainties in the simulated flood extent. Hence, the available DTM product was enhanced in this study, where river reaches were delineated in the DTM, and it was smoothed to minimize the product's defects. The adopted enhancing method was found to perform satisfactorily and reduce errors in the simulated flood extent and depth. Different inflow boundary conditions were defined using streamflow from rain gauges and raw and bias-corrected CHIRPS rainfall data. The flood model is sensitive to the input upstream boundary condition. The model results were found acceptable after enhancing the DTM based on the site's knowledge with a maximum depth (>=2m) observed in the river reaches. However, there were no ground flood depth or extent observations to compare with the simulated results. Satellite-derived flood extent from Planetscope was compared with the simulated flood extent using CSI statistical indicator. This study found a poor match of satellite-based and simulated inundation extent. The mismatch could be originated in the uncertainties of Planetscope image and defects in the considered DTM product, though the product was enhanced. Therefore, the comparison of satellite-based and simulated flood extent was insufficient, thus making the calibration of the 2D HEC-RAS hydrodynamic model with Planetscope-derived flood extent ineffective in the Sebeya catchment.

Overall, this study indicated the significance of bias-corrected SREs, and their further use in the hydrological and hydrodynamic models of the Sebeya catchment. This study could be a basis to assess the extreme events

further causing floods in the data-limited Sebeya catchment using SREs. Besides, this study was the first to attempt the comparison of satellite-derived and simulated flood extent in Rwanda. Therefore, the knowledge described in this study can be used to investigate further the application of satellite-based inundation extent in calibrating hydrodynamic in the Sebeya catchment and other frequently flooded areas in Rwanda.

## 6.2.    Recommendation

The major challenge of this study was the limited quality of available data to set up and calibrate hydrological and hydrodynamic models. A smaller number of rain gauges was the first limitation to overcome the spatial distribution of rainfall in the hydrological model. The observed streamflow was another challenge in calibrating the hydrological model. Meanwhile, the available DTM for the hydrodynamic model poorly represents the topographic representation of surface features, which induced uncertainties in the simulated flood extent and depths. Furthermore, the limited availability of satellite images to extract flood extent was another challenge in this study. Besides, the acquired Planetscope satellite image shows cloud cover and shadow effects. The image possesses only four bands, which limits the investigation of other water indices to delineate inundation extent better. Therefore, the following recommendations could be considered for future studies:

- The number of rain gauge stations should be increased to represent the spatial variability of rainfall in this frequently flooded area, the Sebeya catchment. The daily temporal resolution rainfall data do not better capture the extreme flood event, indicating the need for high temporal resolution records like every 15 min or 30 min or hourly rainfall data.
- The available streamflow data were inadequate in this study. Therefore, it is recommended to check and improve the quality and increase the temporal coverage of disseminated streamflow before being available to the public. This could be done by developing a hydrological model using the approved and checked meteorological and streamflow data to fill the gaps and update the measured streamflow.
- Due to limited time, a small number of satellite rainfall products were investigated in this study on a daily basis. Therefore, exploring other available SREs and analyzing them is recommended based on the Sebeya catchment seasons (rainy vs. dry rainfall detection capability). Additionally, one bias correction method was applied, but future studies can test different approaches to argue on the suitable bias correction scheme in the Sebeya catchment.
- The challenge of unavailable satellite images during a flood event in the Sebeya catchment was inevitably in this study. Therefore, ground recordings of flood extent and depths should be recorded. The UAV[10] or drones can also be used to capture the surface land features, including water extent, during a flood event. This could overcome the difficulties of the available images in the hydrodynamic model calibration.
- The available DEM was enhanced in this study for the hydrodynamic model applications. Much effort was made to correct the DEM, but all the defects could not be removed, which caused uncertainties in the simulated flood results. Therefore, high-resolution and high-quality DEM products, like LiDAR, and detailed river cross-sections, are highly recommended to represent better the topography of land surface features (rivers, buildings, roads, etc.) in the frequently flooded Sebeya areas.
- Extending the flood model domain to the Petit Séminaire high school is recommended to capture all flooded areas in the Sebeya catchment adequately.

---

[10] Unmanned aerial vehicle

# LIST OF REFERENCES

ABAZAJ, F., 2019. SENTINEL-2 Imagery for Mapping and Monitoring Flooding in Buna River Area. J. Int. Environ. Appl. Sci. 15, 48–53.

Abbas, S.A., Al-Aboodi, A.H., Ibrahim, H.T., 2020. Identification of Manning's Coefficient Using HEC-RAS Model: Upstream Al-Amarah Barrage. J. Eng. (United Kingdom) 2020. https://doi.org/10.1155/2020/6450825

Acharya, T.D., Lee, D.H., Yang, I.T., Lee, J.K., 2016. Identification of water bodies in a landsat 8 OLI image using a J48 decision tree. Sensors (Switzerland) 16, 1–16. https://doi.org/10.3390/s16071075

Addae, R.A., 2018. Satellite-Based Flood Mapping for Hydrodynamic Flood Model Assessment: Accra, Ghana (Masters' thesis). Masters' thesis.

Adjei, K.A., Ren, L., Appiah-Adjei, E.K., Odai, S.N., 2015. Application of satellite-derived rainfall for hydrological modelling in the data-scarce Black Volta trans-boundary basin. Hydrol. Res. 46, 777–791. https://doi.org/10.2166/nh.2014.111

Ageet, S., Fink, A.H., Maranan, M., Diem, J.E., Hartter, J., Ssali, A.L., Ayabagabo, P., 2022. Validation of Satellite Rainfall Estimates over Equatorial East Africa. J. Hydrometeorol. 23, 129–151. https://doi.org/10.1175/JHM-D-21-0145.1

Ali, H.T., 2016. Digital Urban Terrain Characterization for 1D2D Hydrodynamic Flood Modelling in Kigali, Rwanda. Thesis 83.

Ali, M.I., Dirawan, G.D., Hasim, A.H., Abidin, M.R., 2019. Detection of changes in surface water bodies urban area with NDWI and MNDWI methods. Int. J. Adv. Sci. Eng. Inf. Technol. 9, 946–951. https://doi.org/10.18517/ijaseit.9.3.8692

Alivio, M.B.T., Puno, G.R., Talisay, B.A.M., 2019. Flood hazard zones using 2d hydrodynamic modeling and remote sensing approaches. Glob. J. Environ. Sci. Manag. 5, 1–16. https://doi.org/10.22034/gjesm.2019.01.01

Anusha, N., Bharathi, B., 2020. Flood detection and flood mapping using multi-temporal synthetic aperture radar and optical data. Egypt. J. Remote Sens. Sp. Sci. 23, 207–219. https://doi.org/10.1016/j.ejrs.2019.01.001

Ashouri, H., Nguyen, P., Thorstensen, A., Hsu, K.L., Sorooshian, S., Braithwaite, D., 2016. Assessing the efficacy of high-resolution satellite-based PERSIANN-CDR precipitation product in simulating streamflow. J. Hydrometeorol. 17, 2061–2076. https://doi.org/10.1175/JHM-D-15-0192.1

Assoumpta, M., Aja, D., 2021. Flood forecasting using quantitative precipitation forecasts and hydrological modeling in the Sebeya catchment , Rwanda 4, 182–203. https://doi.org/10.2166/h2oj.2021.094

Awange, J.L., Ferreira, V.G., Forootan, E., Khandu, Andam-Akorful, S.A., Agutu, N.O., He, X.F., 2016. Uncertainties in remotely sensed precipitation data over Africa. Int. J. Climatol. 36, 303–323. https://doi.org/10.1002/joc.4346

Bakary, F., Abdou, A., Honoré, D., Ansoumana, B., Salif, D., Luc, D., Bakary, F., Abdou, A., Honoré, D., Ansoumana, B., Salif, D., Luc, D., 2018. Assessment of satellite rainfall products for stream flow simulation in Gambia watershed. African J. Environ. Sci. Technol. 12, 501–513. https://doi.org/10.5897/ajest2018.2551

Bao, H.J., Zhao, L.N., 2011. Hydraulic model with roughness coefficient updating method based on Kalman filter for channel flood forecast. Water Sci. Eng. 4, 13–23. https://doi.org/10.3882/j.issn.1674-2370.2011.01.002

Becker, A., Serban, P., 1990. World Meteorological Organization Hydrological Models for Water-Resources System Design and Operation " '.

Beden, N., Ulke Keskin, A., 2021. Flood map production and evaluation of flood risks in situations of insufficient flow data. Nat. Hazards 105, 2381–2408. https://doi.org/10.1007/s11069-020-04404-y

Behrangi, A., Khakbaz, B., Jaw, T.C., AghaKouchak, A., Hsu, K., Sorooshian, S., 2011. Hydrologic evaluation of satellite precipitation products over a mid-size basin. J. Hydrol. 397, 225–237. https://doi.org/10.1016/j.jhydrol.2010.11.043

Belay, A.S., Fenta, A.A., Yenehun, A., Nigate, F., Tilahun, S.A., Moges, M.M., Dessie, M., Adgo, E., Nyssen, J., Chen, M., Van Griensven, A., Walraevens, K., 2019. Evaluation and application of multi-source satellite rainfall product CHIRPS to assess spatio-temporal rainfall variability on data-sparse western margins of Ethiopian highlands. Remote Sens. 11, 1–22.

https://doi.org/10.3390/rs11222688

Bergström, S., 1992. The HBV model - its structure and applications. Swedish Meteorol. Hydrol. Institute, Norrköping 4, 1–33.

Bergstrom S, 1976. Development and application of a conceptual runoff model for Scandinavian catchments. SMHI 7.

Bhatt, C.M., Srinivasa Rao, G., 2018. HAND (height above nearest drainage) tool and satellite-based geospatial analysis of Hyderabad (India) urban floods, September 2016. Arab. J. Geosci. 11. https://doi.org/10.1007/s12517-018-3952-1

Bhatti, H.A., Rientjes, T., Haile, A.T., Habib, E., Verhoef, W., 2016. Evaluation of bias correction method for satellite-based rainfall data. Sensors (Switzerland) 16, 1–16. https://doi.org/10.3390/s16060884

Bitew, M.M., Gebremichael, M., 2011. Evaluation of satellite rainfall products through hydrologic simulation in a fully distributed hydrologic model. Water Resour. Res. 47, 1–11. https://doi.org/10.1029/2010WR009917

Boukhaly Traore, V., Bop, M., Faye, M., Malomar, G., Hadj, E., Gueye, O., Sambou, H., Dione, A.N., Fall, S., Diaw, A.T., Sarr, J., Chedikh Beye, A., 2015. Using of Hec-ras Model for Hydraulic Analysis of a River with Agricultural Vocation: A Case Study of the Kayanga River Basin, Senegal. Am. J. Water Resour. 3, 147–154. https://doi.org/10.12691/ajwr-3-5-2

Brunner, G.W., 2021a. HEC-RAS HEC-RAS 2D User's Manual 171.

Brunner, G.W., 2021b. HEC-RAS, River Analysis System User's Manual 1–962.

Brunner, G.W., CEIWR-HEC, 2021. HEC-RAS HEC-RAS 2D User's Manual.

Chignell, S.M., Anderson, R.S., Evangelista, P.H., Laituri, M.J., Merritt, D.M., 2015. Multi-temporal independent component analysis and landsat 8 for delineating maximum extent of the 2013 Colorado front range flood. Remote Sens. 7, 9822–9843. https://doi.org/10.3390/rs70809822

Chow, C., Twele, A., Martinis, S., 2016. An assessment of the Height Above Nearest Drainage terrain descriptor for the thematic enhancement of automatic SAR-based flood monitoring services. Remote Sens. Agric. Ecosyst. Hydrol. XVIII 9998, 999808. https://doi.org/10.1117/12.2240766

Collier, P., Conway, G., Venables, T., 2008. Climate change and Africa. Oxford Rev. Econ. Policy 24, 337–353. https://doi.org/10.1093/oxrep/grn019

Cook, A., Merwade, V., 2009. Effect of topographic data, geometric configuration and modeling approach on flood inundation mapping. J. Hydrol. 377, 131–142. https://doi.org/10.1016/j.jhydrol.2009.08.015

Costabile, P., Costanzo, C., Ferraro, D., Macchione, F., Petaccia, G., 2020. Performances of the new HEC-RAS version 5 for 2-D hydrodynamic-based rainfall-runoff simulations at basin scale: Comparison with a state-of-the art model. Water (Switzerland) 12, 1–19. https://doi.org/10.3390/W12092326

Devia, G.K., Ganasri, B.P., Dwarakish, G.S., 2015. A Review on Hydrological Models. Aquat. Procedia 4, 1001–1007. https://doi.org/10.1016/j.aqpro.2015.02.126

Di Baldassarre, G., Schumann, G., Bates, P.D., 2009. A technique for the calibration of hydraulic models using uncertain satellite observations of flood extent. J. Hydrol. 367, 276–282. https://doi.org/10.1016/j.jhydrol.2009.01.020

Dinku, T., Ceccato, P., Grover-Kopec, E., Lemma, M., Connor, S.J., Ropelewski, C.F., 2007. Validation of satellite rainfall products over East Africa's complex topography. Int. J. Remote Sens. 28, 1503–1526. https://doi.org/10.1080/01431160600954688

Dinku, T., Funk, C., Peterson, P., Maidment, R., Tadesse, T., Gadain, H., Ceccato, P., 2018. Validation of the CHIRPS satellite rainfall estimates over eastern Africa. Q. J. R. Meteorol. Soc. 144, 292–312. https://doi.org/10.1002/qj.3244

Douben, K.J., 2006. Characteristics of river floods and flooding: A global overview, 1985-2003. Irrig. Drain. 55, 25–27. https://doi.org/10.1002/ird.239

Dubey, A.K., Kumar, P., Chembolu, V., Dutta, S., Singh, R.P., Rajawat, A.S., 2021. Flood modeling of a large transboundary river using WRF-Hydro and microwave remote sensing. J. Hydrol. 598, 126391. https://doi.org/10.1016/j.jhydrol.2021.126391

EFRC, 2018. DREF Emergency Plan of Action (EPoA) Rwanda Storm & Heavy Winds 1–20.

Ettritch, G., Hardy, A., Bojang, L., Cross, D., Bunting, P., Brewer, P., 2018. Enhancing digital elevation models for hydraulic modelling using flood frequency detection. Remote Sens. Environ. 217, 506–522. https://doi.org/10.1016/j.rse.2018.08.029

Feyisa, G.L., Meilby, H., Fensholt, R., Proud, S.R., 2014. Automated Water Extraction Index: A new technique for surface water mapping using Landsat imagery. Remote Sens. Environ. 140, 23–35. https://doi.org/10.1016/j.rse.2013.08.029

Funk, C.C., Peterson, P.J., Landsfeld, M.F., Pedreros, D.H., Verdin, J.P., Rowland, J.D., Romero, B.E., Husak, G.J., Michaelsen, J.C., Verdin, A.P., 2014. A Quasi-Global Precipitation Time Series for Drought Monitoring. U.S. Geol. Surv. Data Ser. 832, 4. https://doi.org/10.3133/ds832

Gandhi, G.M., Parthiban, S., Thummalu, N., Christy, A., 2015. Ndvi: Vegetation Change Detection Using Remote Sensing and Gis - A Case Study of Vellore District. Procedia Comput. Sci. 57, 1199–1210. https://doi.org/10.1016/j.procs.2015.07.415

Garrote, J., González-Jiménez, M., Guardiola-Albert, C., Díez-Herrero, A., 2021. The manning's roughness coefficient calibration method to improve flood hazard analysis in the absence of river bathymetric data: Application to the urban historical zamora city centre in spain. Appl. Sci. 11. https://doi.org/10.3390/app11199267

Gebregiorgis, A.S., Hossain, F., 2013. Understanding the dependence of satellite rainfall uncertainty on topography and climate for hydrologic model simulation. IEEE Trans. Geosci. Remote Sens. 51, 704–718. https://doi.org/10.1109/TGRS.2012.2196282

Ghimire, S., 2013. Application of a 2D hydrodynamic model for assessing flood risk from extreme storm events. Climate 1, 148–162. https://doi.org/10.3390/cli1030148

Giustarini, L., Chini, M., Hostache, R., Pappenberger, F., Matgen, P., 2015. Flood hazard mapping combining hydrodynamic modeling and multi annual remote sensing data. Remote Sens. 7, 14200–14226. https://doi.org/10.3390/rs71014200

Godara, N., Bruland, O., Scholar, P., 2019. Choosing an Appropriate Hydrologic Model 1–18.

Grimaldi, S., Li, Y., Pauwels, V.R.N., Walker, J.P., 2016. Remote Sensing-Derived Water Extent and Level to Constrain Hydraulic Flood Forecasting Models: Opportunities and Challenges. Surv. Geophys. 37, 977–1034. https://doi.org/10.1007/s10712-016-9378-y

Gumindoga, W., Rientjes, T.H.M., Haile, A.T., Makurira, H., Reggiani, P., 2016. Bias correction schemes for CMORPH satellite rainfall estimates in the Zambezi River Basin. Hydrol. Earth Syst. Sci. Discuss. 0, 1–36. https://doi.org/10.5194/hess-2016-33

Gumindoga, W., Rientjes, T.H.M., Tamiru Haile, A., Makurira, H., Reggiani, P., 2019. Performance of bias-correction schemes for CMORPH rainfall estimates in the Zambezi River basin. Hydrol. Earth Syst. Sci. 23, 2915–2938. https://doi.org/10.5194/hess-23-2915-2019

Habib, E., Haile, A.T., Sazib, N., Zhang, Y., Rientjes, T., 2014. Effect of bias correction of satellite-rainfall estimates on runoff simulations at the source of the Upper Blue Nile. Remote Sens. 6, 6688–6708. https://doi.org/10.3390/rs6076688

Hamlin, M.J., 1983. The significance of rainfall in the study of hydrological processes at basin scale. J. Hydrol. 65, 73–94. https://doi.org/10.1016/0022-1694(83)90211-1

Hawker, L., Bates, P., Neal, J., Rougier, J., 2018. Perspectives on Digital Elevation Model (DEM) Simulation for Flood Modeling in the Absence of a High-Accuracy Open Access Global DEM. Front. Earth Sci. 6, 1–9. https://doi.org/10.3389/feart.2018.00233

Heidler, Lisa, 2015. Evaluation of Different Hydrological Models in Data Scarce Regions on the Island of Ceram, Indonesia.

Hu, A., Demir, I., 2021. Real-time flood mapping on client-side web systems using hand model. Hydrology 8. https://doi.org/10.3390/hydrology8020065

Hunter, N.M., 2005. Development and assessment of dynamic storage cell codes for flood inundation modelling. Sch. Geogr. Sci. 360.

Hunter, N.M., Bates, P.D., Horritt, M.S., de Roo, P.J., Werner, M.G.F., 2005. Utility of different data types for calibrating flood inundation models within a GLUE framework. Hydrol. Earth Syst. Sci. 9, 412–430. https://doi.org/10.5194/hess-9-412-2005

IFRC, 2012. World Disaster Report. Focus on forced migration and displacement, International Federation of Red Cross and Red Crescent Societies.

J.Arcement, G., Schneider, V.R., 1989. Guide for Selecting Manning's Roughness Coefficients for Natural Channels and Flood Plains United States Geological Survey Water-supply Paper 2339. Area 2339, 39.

Jamandre, C.A., Narisma, G.T., 2013. Spatio-temporal validation of satellite-based rainfall estimates in the Philippines. Atmos. Res. 122, 599–608. https://doi.org/10.1016/j.atmosres.2012.06.024

Joyce, R.J., Janowiak, J.E., Arkin, P.A., Xie, P., 2004. CMORPH: A method that produces global precipitation estimates from passive microwave and infrared data at high spatial and temporal resolution. J. Hydrometeorol. 5, 487–503. https://doi.org/10.1175/1525-7541(2004)005<0487:CAMTPG>2.0.CO;2

Karim, F., Petheram, C., Marvanek, S., Ticehurst, C., Wallace, J., Gouweleeuw, B., 2011. The use of hydrodynamic modelling and remote sensing to estimate floodplain inundation and flood discharge in a large tropical catchment. MODSIM 2011 - 19th Int. Congr. Model. Simul. - Sustain. Our Futur. Underst. Living with Uncertain. 3796–3802.

Kidd, C., Kniveton, D.R., Todd, M.C., Bellerby, T.J., 2003. Satellite rainfall estimation using combined passive microwave and infrared algorithms. J. Hydrometeorol. 4, 1088–1104. https://doi.org/10.1175/1525-7541(2003)004<1088:SREUCP>2.0.CO;2

Kimani, M.W., Hoedjes, J.C.B., Su, Z., 2017. An assessment of satellite-derived rainfall products relative to ground observations over East Africa. Remote Sens. 9. https://doi.org/10.3390/rs9050430

Klemas, V., 2015. Remote sensing of floods and flood-prone areas: An overview. J. Coast. Res. 31, 1005–1013. https://doi.org/10.2112/JCOASTRES-D-14-00160.1

Lea, D., Yeonsu, K., Hyunuk, A., 2019. Case study of HEC-RAS 1D-2D coupling simulation: 2002 Baeksan flood event in Korea. Water (Switzerland) 11, 1–14. https://doi.org/10.3390/w11102048

Liu, Q., Qin, Y., Zhang, Y., Li, Z., 2015. A coupled 1D–2D hydrodynamic model for flood simulation in flood detention basin. Nat. Hazards 75, 1303–1325. https://doi.org/10.1007/s11069-014-1373-3

Liu, Z., Merwade, V., Jafarzadegan, K., 2019. Investigating the role of model structure and surface roughness in generating flood inundation extents using one- and two-dimensional hydraulic models. J. Flood Risk Manag. 12. https://doi.org/10.1111/jfr3.12347

Machlica, A., Horvát, O., Horáček, S., Oosterwijk, J., Van Loon, A.F., Fendeková, M., Van Lanen, H.A.J., 2012. Influence of model structure on base flow estimation using BILAN, FRIER and HBV-light models. J. Hydrol. Hydromechanics 60, 242–251. https://doi.org/10.2478/v10098-012-0021-4

Maidment, R.I., Grimes, D., Allan, R.P., Tarnavsky, E., Marcstringer, M., Hewison, T., Roebeling, R., Black, E., 2014. The 30 year TAMSAT african rainfall climatology and time series (TARCAT) data set. J. Geophys. Res. 119, 10,619-10,644. https://doi.org/10.1002/2014JD021927

Maidment, R.I., Grimes, D., Black, E., Tarnavsky, E., Young, M., Greatrex, H., Allan, R.P., Stein, T., Nkonde, E., Senkunda, S., Alcántara, E.M.U., 2017. A new, long-term daily satellite-based rainfall dataset for operational monitoring in Africa. Sci. Data 4. https://doi.org/10.1038/sdata.2017.63

Manavalan, R., 2017. SAR image analysis techniques for flood area mapping - literature survey. Earth Sci. Informatics 10, 1–14. https://doi.org/10.1007/s12145-016-0274-2

Manyifika, M., 2015. Diagnostic assessment on urban floods using satellite data and hydrologic models in Kigali, Rwanda. Thesis 88.

Marie Aimée, B.N., 2020. ANALYSIS OF FLOOD RESILIENCE USING PARTICIPATORY GIS APPROACH.

Masson-Delmotte, V., Zhai, P., Pörtner, H.-O., Roberts, D., Skea, J., Shukla, P.R., Pirani, A., Moufouma-Okia, W., Péan, C., Pidcock, R., Connors, S., Matthews, J.B.R., Chen, Y., Zhou, X., Gomis, M.I., Lonnoy, E., Maycock, T., Tignor, M., Waterfield, T., 2018. Global warming of 1.5°C. An IPCC Spec. Rep. impacts Glob. Warm. 1.5°C above pre-industrial levels Relat. Glob. Greenh. gas Emiss. pathways, Context Strength. Glob. response to Threat Clim. Chang. Sustain. Dev. 291, 285. https://doi.org/10.1038/291285a0

McFeeters, S.K., 1996. The use of the Normalized Difference Water Index (NDWI) in the delineation of open water features. Remote Sens. Environ. 25, 687–711. https://doi.org/10.1080/01431169608948714

Md Ali, A., Solomatine, D.P., Di Baldassarre, G., 2015. Assessing the impact of different sources of topographic data on 1-D hydraulic modelling of floods. Hydrol. Earth Syst. Sci. 19, 631–643. https://doi.org/10.5194/hess-19-631-2015

Mendez, M., Calvo-Valverde, L., 2016. Development of the HBV-TEC Hydrological Model. Procedia Eng. 154, 1116–1123. https://doi.org/10.1016/j.proeng.2016.07.521

Merwade, V., Olivera, F., Arabi, M., Edleman, S., 2008. Uncertainty in Flood Inundation Mapping: Current Issues and Future Directions. J. Hydrol. Eng. 13, 608–620. https://doi.org/10.1061/(asce)1084-0699(2008)13:7(608)

Mesa-Mingorance, J.L., Ariza-López, F.J., 2020. Accuracy assessment of digital elevation models (DEMs):

A critical review of practices of the past three decades. Remote Sens. 12, 1–27. https://doi.org/10.3390/RS12162630

MINEMA, 2018. Republic of Rwanda Ministry in Charge of Emergency Management.

Muthusamy, M., Casado, M.R., Butler, D., Leinster, P., 2021. Understanding the effects of Digital Elevation Model resolution in urban fluvial flood modelling. J. Hydrol. 596. https://doi.org/10.1016/j.jhydrol.2021.126088

Niang, I., Ruppel, O.C., Abdrabo, M.A., Essel, A., Lennard, C., Padgham, J., Urquhart, P., 2015. Africa. Clim. Chang. 2014 Impacts, Adapt. Vulnerability Part B Reg. Asp. Work. Gr. II Contrib. to Fifth Assess. Rep. Intergov. Panel Clim. Chang. 1199–1266. https://doi.org/10.1017/CBO9781107415386.002

Nikolopoulos, E.I., Anagnostou, E.N., Hossain, F., Gebremichael, M., Borga, M., 2010. Understanding the scale relationships of uncertainty propagation of satellite rainfall through a distributed hydrologic model. J. Hydrometeorol. 11, 520–532. https://doi.org/10.1175/2009JHM1169.1

Nkunzimana, A., Bi, S., Alriah, M.A.A., Zhi, T., Kur, N.A.D., 2020. Earth and Space Science - 2020 - Nkunzimana - Comparative Analysis of the Performance of Satellite-Based Rainfall Products.pdf. Earth Sp. Sci. 7. https://doi.org/10.1029/2019EA000834

Nobre, A.D., Cuartas, L.A., Hodnett, M., Rennó, C.D., Rodrigues, G., Silveira, A., Waterloo, M., Saleska, S., 2011. Height Above the Nearest Drainage - a hydrologically relevant new terrain model. J. Hydrol. 404, 13–29. https://doi.org/10.1016/j.jhydrol.2011.03.051

Nobre, A.D., Cuartas, L.A., Momo, M.R., Severo, D.L., Pinheiro, A., Nobre, C.A., 2016. HAND contour: A new proxy predictor of inundation extent. Hydrol. Process. 30, 320–333. https://doi.org/10.1002/hyp.10581

Notti, D., Giordan, D., Caló, F., Pepe, A., Zucca, F., Galve, J.P., 2018. Potential and limitations of open satellite data for flood mapping. Remote Sens. 10. https://doi.org/10.3390/rs10111673

Omondi, C.K., Rientjes, T.H.M., Booij, M.J., Nelson, A.D., 2021. Satellite rainfall bias assessment for crop growth simulation – A case study of maize growth in Kenya. Agric. Water Manag. 258. https://doi.org/10.1016/j.agwat.2021.107204

Ongdas, N., Akiyanova, F., Karakulov, Y., Muratbayeva, A., Zinabdin, N., 2020. Application of hec-ras (2d) for flood hazard maps generation for yesil (ishim) river in kazakhstan. Water (Switzerland) 12, 1–20. https://doi.org/10.3390/w12102672

Planet Labs, 2021. Planet Application Program Interface: In Space for Life on Earth. San Francisco, CA, USA. Downloaded from https://assets.planet.com/docs/Planet_Combined_Imagery_Product_Specs_letter_screen.pdf. Planet Labs Inc 1–100.

Planet Labs, 2020. Planet Surface Reflectance Product v2. Planet Labs, Inc. Downloaded from https://assets.planet.com/marketing/PDF/Planet_Surface_Reflectance_Technical_White_Paper.pdf. 1–18.

Quirogaa, V.M., Kurea, S., Udoa, K., Manoa, A., 2016. Application of 2D numerical simulation for the analysis of the February 2014 Bolivian Amazonia flood: Application of the new HEC-RAS version 5. Ribagua 3, 25–33. https://doi.org/10.1016/j.riba.2015.12.001

Rahmawati, N., Rahayu, K., Yuliasari, S.T., 2021. Performance of daily satellite-based rainfall in groundwater basin of Merapi Aquifer System, Yogyakarta. Theor. Appl. Climatol. 146, 173–190. https://doi.org/10.1007/s00704-021-03731-9

Rangari, V.A., Umamahesh, N. V., Bhatt, C.M., 2019. Assessment of inundation risk in urban floods using HEC RAS 2D. Model. Earth Syst. Environ. 5, 1839–1851. https://doi.org/10.1007/s40808-019-00641-8

Refice, A., Capolongo, D., Pasquariello, G., Daaddabbo, A., Bovenga, F., Nutricato, R., Lovergine, F.P., Pietranera, L., 2014. SAR and InSAR for flood monitoring: Examples with COSMO-SkyMed data. IEEE J. Sel. Top. Appl. Earth Obs. Remote Sens. 7, 2711–2722. https://doi.org/10.1109/JSTARS.2014.2305165

Rennó, C.D., Nobre, A.D., Cuartas, L.A., Soares, J.V., Hodnett, M.G., Tomasella, J., Waterloo, M.J., 2008. HAND, a new terrain descriptor using SRTM-DEM: Mapping terra-firme rainforest environments in Amazonia. Remote Sens. Environ. 112, 3469–3481. https://doi.org/10.1016/j.rse.2008.03.018

Rientjes, T.H.M., 2016. Hydrologic modelling for Integrated Water Resource Assessments. Lect. B. Modul. 9-10 Surf. water stream 255.

Rientjes, T.H.M., Haile, A.T., Kebede, E., Mannaerts, C.M.M., Habib, E., Steenhuis, T.S., 2011. Changes in land cover, rainfall and stream flow in Upper Gilgel Abbay catchment, Blue Nile basin - Ethiopia. Hydrol. Earth Syst. Sci. 15, 1979–1989. https://doi.org/10.5194/hess-15-1979-2011

Sælthun, N.R., 1996. The "Nordic" HBV Model. Description and documentation of the model version developed for the project Climate Change and Energy Production. NVE Publ. 7, Nor. Water Ressources Energy Adm. Oslo 26.

Sajjad, A., Lu, J., Chen, X., Saleem, N., 2021. Rapid riverine flood mapping with different water indexes using flood instances Landsat-8 images 8049. https://doi.org/10.3390/ecws-5-08049

Schumann, G., Bates, P.D., Horritt, M.S., Matgen, P., Pappenberger, F., 2009. Progress in integration of remote sensing-derived flood extent and stage data and hydraulic models. Rev. Geophys. 47, 1–20. https://doi.org/10.1029/2008RG000274

Seibert, J., 2005. HBV light. HBV Light version 2 User's Man.

Seibert, J., Vis, M.J.P., 2012. Teaching hydrological modeling with a user-friendly catchment-runoff-model software package. Hydrol. Earth Syst. Sci. 16, 3315–3325. https://doi.org/10.5194/hess-16-3315-2012

Sekertekin, A., 2019. Mapping of Surface Water Resources: A Comparative Analysis of Eight Image Classification Methods. Theor. Investig. Appl. Stud. Eng. 269–284.

Shen, X., Wang, D., Mao, K., Anagnostou, E., Hong, Y., 2019. Inundation extent mapping by synthetic aperture radar: A review. Remote Sens. 11, 1–17. https://doi.org/10.3390/RS11070879

Shen, Y., Xiong, A., Wang, Y. and, Xie, P., 2010. Performance of high-resolution satellite precipitation products over China. https://doi.org/doi:10.1029/2009JD012097

Singh, R.K., Kumar Villuri, V.G., Pasupuleti, S., Nune, R., 2020. Hydrodynamic modeling for identifying flood vulnerability zones in lower Damodar river of eastern India. Ain Shams Eng. J. 11, 1035–1046. https://doi.org/10.1016/j.asej.2020.01.011

Sivanpillai, R., Jacobs, K.M., Mattilio, C.M., Piskorski, E. V., 2021. Rapid flood inundation mapping by differencing water indices from pre- and post-flood Landsat images. Front. Earth Sci. 15, 1–11. https://doi.org/10.1007/s11707-020-0818-0

Solomatine, D.P., Shrestha, D.L., 2009. A novel method to estimate model uncertainty using machine learning techniques. Water Resour. Res. 45, 1–16. https://doi.org/10.1029/2008WR006839

SUHET, 2015. Sentinel-2 User Handbook. Eur. Sp. Agency 2, 64. https://doi.org/10.1021/ie51400a018

Tarekegn, T.H., Haile, A.T., Rientjes, T., Reggiani, P., Alkema, D., 2010. Assessment of an ASTER-generated DEM for 2D hydrodynamic flood modeling. Int. J. Appl. Earth Obs. Geoinf. 12, 457–465. https://doi.org/10.1016/j.jag.2010.05.007

Tarnavsky, E., Grimes, D., Maidment, R., Black, E., Allan, R.P., Stringer, M., Chadwick, R., Kayitakire, F., 2014. Extension of the TAMSAT satellite-based rainfall monitoring over Africa and from 1983 to present. J. Appl. Meteorol. Climatol. 53, 2805–2822. https://doi.org/10.1175/JAMC-D-14-0016.1

Timbadiya, P. V., Patel, P.L., Porey, P.D., 2015. A 1D–2D Coupled Hydrodynamic Model for River Flood Prediction in a Coastal Urban Floodplain. J. Hydrol. Eng. 20, 05014017. https://doi.org/10.1061/(asce)he.1943-5584.0001029

Tramblay, Y., Thiemig, V., Dezetter, A., Hanich, L., 2016. Evaluation of satellite-based rainfall products for hydrological modelling in Morocco. Hydrol. Sci. J. 61, 2509–2519. https://doi.org/10.1080/02626667.2016.1154149

USACE, 2021. HEC-RAS, River Analysis System Hydraulic Reference Manual. Hydrol. Eng. Cent.

Vant-Hull, B., Mahani, S., Autones, F., Mecikalski, J.R., Rabin, R., 2014. Infrared satellite rainfall monitoring: Relationships between cloud towers, rainfall intensity, and lightning. Int. J. Water 8, 343–367. https://doi.org/10.1504/IJW.2014.065792

Watson, C.S., Carrivick, J., Quincey, D., 2015. An improved method to represent DEM uncertainty in glacial lake outburst flood propagation using stochastic simulations. J. Hydrol. 529, 1373–1389. https://doi.org/10.1016/j.jhydrol.2015.08.046

Wiwoho, B.S., Astuti, I.S., Alfarizi, I.A.G., Sucahyo, H.R., 2021. Validation of three daily satellite rainfall products in a humid tropic watershed, brantas, indonesia: Implications to land characteristics and hydrological modelling. Hydrology 8. https://doi.org/10.3390/hydrology8040154

Wu, H., Adler, R.F., Hong, Y., Tian, Y., Policelli, F., 2012. Evaluation of global flood detection using satellite-based rainfall and a hydrologic model. J. Hydrometeorol. 13, 1268–1284. https://doi.org/10.1175/JHM-D-11-087.1

Xu, H., 2006. Modification of normalised difference water index (NDWI) to enhance open water features in remotely sensed imagery. Int. J. Remote Sens. 27, 3025–3033. https://doi.org/10.1080/01431160600589179

Xu, K., Fang, J., Fang, Y., Sun, Q., Wu, C., Liu, M., 2021. The Importance of Digital Elevation Model Selection in Flood Simulation and a Proposed Method to Reduce DEM Errors: A Case Study in Shanghai. Int. J. Disaster Risk Sci. 12, 890–902. https://doi.org/10.1007/s13753-021-00377-z

Xue, X., Hong, Y., Limaye, A.S., Gourley, J.J., Huffman, G.J., Khan, S.I., Dorji, C., Chen, S., 2013. Statistical and hydrological evaluation of TRMM-based Multi-satellite Precipitation Analysis over the Wangchu Basin of Bhutan: Are the latest satellite precipitation products 3B42V7 ready for use in ungauged basins? J. Hydrol. 499, 91–99. https://doi.org/10.1016/j.jhydrol.2013.06.042

Yalcin, E., 2018. Two-dimensional hydrodynamic modelling for urban flood risk assessment using.pdf. https://doi.org/10.1111/jfr3.12499

Yan, K., Di Baldassarre, G., Solomatine, D.P., Schumann, G.J.P., 2015. A review of low-cost space-borne data for flood modelling: topography, flood extent and water level. Hydrol. Process. 29, 3368–3387. https://doi.org/10.1002/hyp.10449

Yang, X., Zhao, S., Qin, X., Zhao, N., Liang, L., 2017. Mapping of urban surface water bodies from sentinel-2 MSI imagery at 10 m resolution via NDWI-based image sharpening. Remote Sens. 9, 1–19. https://doi.org/10.3390/rs9060596

Ymeti, I., 2007. Rainfall estimation by Remote Sensing for conceptual rainfall-runoff modeling in the Upper Blue Nile basin Rainfall estimation by Remote Sensing for conceptual rainfall-runoff modeling in the Upper Blue Nile basin. Geo-Information Sci.

Zainalfikry, M.K., Ab Ghani, A., Zakaria, N.A., Chan, N.W., 2020. HEC-RAS One-Dimensional Hydrodynamic Modelling for Recent Major Flood Events in Pahang River. Lect. Notes Civ. Eng. 53, 1099–1115. https://doi.org/10.1007/978-3-030-32816-0_83

Zhao, H., Yang, S., Wang, Z., Zhou, X., Luo, Y., Wu, L., 2015. Evaluating the suitability of TRMM satellite rainfall data for hydrological simulation using a distributed hydrological model in the Weihe River catchment in China. J. Geogr. Sci. 25, 177–195. https://doi.org/10.1007/s11442-015-1161-3